AMBIENT NOISE TOMOGRAPHY FOR A HIGH SPATIAL-RESOLUTION 3D S-WAVE VELOCITY AND AZIMUTHAL ANISOTROPY MODEL OF THE KINKI REGION, SOUTHWEST JAPAN, USING DENSE SEISMIC ARRAY DATA

ボカニ, ンサバ

AMBIENT NOISE TOMOGRAPHY FOR A HIGH SPATIAL-RESOLUTION 3D S-WAVE VELOCITY AND AZIMUTHAL ANISOTROPY MODEL OF THE KINKI REGION, SOUTHWEST JAPAN, USING DENSE SEISMIC ARRAY DATA

BOKANI NTHABA

2022

AMBIENT NOISE TOMOGRAPHY FOR A HIGH SPATIAL-RESOLUTION 3D S-WAVE VELOCITY AND AZIMUTHAL ANISOTROPY MODEL OF THE KINKI REGION, SOUTHWEST JAPAN, USING DENSE SEISMIC ARRAY DATA

By

BOKANI NTHABA

A dissertation submitted in partial fulfillment of requirements

for the degree of

Doctoral Engineering

Department of Earth Resources Engineering

Graduate School of Engineering

Kyushu University

Japan

December 2022

Abstract

The interactions among the subducting Philippine Sea Plate (PSP), the overriding Eurasian or Amurian (Amur) plate and the Pacific Oceanic Plate continually deform the crust and produces major tectonic structures in the Kinki region, southwest Japan. In this region, there is an apparent inconsistency between earthquake hypocenters and the location of documented active faults. Some of these earthquake hypocenters either occur between known fault locations or are aligned in the same direction as documented active faults, suggesting a possible existence of concealed faults or other deformational structures. Previous studies that sought to unravel the geological heterogeneities in the Kinki region focused mainly on deep, large-scale structures and could not resolve fine-scale (~13 km) shallow crustal structures. Therefore, there is a need to characterize the upper crustal structure of this region at an improved spatial resolution. The fundamental aim of this study is to estimate and characterize the shallow crustal structure of the Kinki region at an improved spatial resolution using the ever-present ambient seismic noise. In Chapter 1, I provide the background information, justification and the aims of this study. A detailed description of the geologic setting of the Kinki area is given in Chapter 2.

In Chapter 3, I provide a detailed description of the data and methods used in this study. Firstly, I pre-processed the continuous seismic waveforms recorded over a period of six months by the densely distributed 221 permanent and temporary seismic stations. Then, I derived the empirical Green's functions from the cross-correlations of the vertical component of ambient seismic noise data, from which Rayleigh wave phase velocities were estimated using a frequency domain method (Zero-crossing). Using the estimated phase velocity dispersion data, I constructed high-resolution 3D S-wave velocity and azimuthal anisotropy models of the Kinki region based on ambient noise tomography (ANT) method, a form of interferometry. To construct the 3D S-wave velocity model, I applied a direct surface wave tomographic method (DSurfTomo), which is based on frequency-dependent ray-tracing inversion. This inversion approach is well-suited to determining the complex shallow crustal structure of the Kinki region using the short-period surface waves dispersion data.

To further construct the 3D azimuthal anisotropy model, I applied a direct joint inversion (DAzimSurfTomo) method. Here, the inversion workflow was implemented in two steps. Firstly, I obtained the 3D isotropic S-wave model by inverting the measured Rayleigh

wave phase velocity dispersion data using a 3D direct inversion method. Secondly, the isotropic S-wave velocity model obtained from the initial step was then used as the 3D reference model to perform a joint inversion for both 3D isotropic S-wave velocity perturbation and azimuthal anisotropy.

In Chapters 4 and 5, I presented the results of this study and their interpretations. Here, the 3D isotropic S-wave velocity model constructed in Chapter 3 revealed a NE-SW trending low-velocity structure coinciding with the location of the Niigata-Kobe Tectonic Zone (NKTZ) and the active Biwako-seigan Fault Zone (BSFZ). Also, I identified fine-scale low-velocity structures coinciding with known active faults on the eastern side of the NKTZ, as well as sets of low-velocity structures on the northern side of the Arima-Takatsuki Tectonic Line (ATTL). Moreover, sedimentary basins manifest as low-velocity zones extending to depths ranging from ~1.5 to 2 km, correlating well with those reported in previous studies.

The resolved 3D azimuthal anisotropy model reveals significant contrasts of anisotropy across the Kinki region. The southern part shows predominantly NE-SW- and near E-W-trending fast axes in the central part and the western part of the Kii Mountainland, respectively, which are attributable to stress-induced anisotropy. In the northwestern part, the observed fast axes direction is consistent with that of the maximum horizontal compressional stress and the principal strain rate axes, suggesting that the observed anisotropy in the northwestern part of the Kinki region is influenced by both the stress field and strain rate. On the depth profiles of anisotropy, I observed depth-dependent variation of azimuthal anisotropy. Furthermore, my model revealed a significant consistency between azimuthal anisotropy and seismicity beneath a depth of 3 km. This interrelationship between anisotropy and seismicity demonstrates that the observed anisotropy could be linked to local crustal stress or fractures relevant to earthquake ruptures. The high-spatial resolution 3D anisotropy model obtained in this study therefore contributes towards understanding the locations and features of seismicity region. Most importantly, the results of this study contribute towards understanding the complex shallow crustal structure, earthquake faulting, the dominant deformation mechanisms in the tectonically active Kinki area, and will be useful for hazard assessment and disaster mitigation. The main findings of this study are summarized in Chapter 6.

List of papers

This thesis is based on the following papers.

1. **Nthaba, B.**, Ikeda, T., Nimiya, H., Tsuji, T., & Iio, Y. (2022). Ambient noise tomography for a high-resolution 3D S-wave velocity model of the Kinki Region, Southwestern Japan, using dense seismic array data. Earth Planets Space 74, 96 (2022). https://doi.org/10.1186/s40623-022-01654-x

2. **Nthaba, B.**, Ikeda, T., Nimiya, H., Tsuji, T., & Iio, Y. (2022). High Spatial Resolution Three-dimensional Azimuthal Anisotropy southwest Japan, based on Ambient Noise Tomography. Manuscript, to be submitted to a peer-reviewed journal.

In addition, below is another publication during my PhD that is not included in the main part of this thesis but is in Appendix A:

- **Nthaba, B.**, Shemang, E., Hengari, A., Kgosidintsi, B., & Tsuji, T. (2020). Characterizing coal seams hosted in Mmamabula Coalfield, central Botswana using pseudo-3D electrical resistivity imaging technique. Journal of African Earth Sciences, 167, 103866.

Table of Contents

List of abbreviations

AF	Aibano Fault
AIST	National Institute of Advanced Industrial Science and Technology
ANT	Ambient Noise Tomography
ATTL	Arima-Takatsuki Tectonic Line
BSFZ	Biwako-seigan Fault Zone
CF	Chinai Fault
CT	Chichibu terrain
EUR	Eurasian
FB	Fukuchiyama basin
HF	Hiei Fault
HiF	Hira Fault
HO	Hokutan Block
HOF	Hanaore Fault
HT	Hidaka terrain
IB	Ise basin
IFZ	Ikoma Fault Zone
JMA	Japan Meteorological Agency
KaF	Katata Fault
KB	Kyoto basin
KF	Kamidera Fault
KtF	Katsuno Fault
KZF	Kizugawa Fault

MA	Maizuru Block
MT	Muro terrain
MTF	Mitoke Fault
MTL	Median Tectonic Line
MZ	Maizuru Zone
NB	Nara basin
NIED	National Research Institute for Earth Science and Disaster Resilience
NKTZ	Niigata-Kobe Tectonic Zone
OB	Osaka basin
OoB	Oomi basin
PHS	Philippine Sea
RAFZ	Rokko Active Fault Zone
RT	Ryoke terrain
SB	Sanda basin
SPAC	Spatial autocorrelation
SKF	Suzuka Fault
SMZ	Sambagawa metamorphic terrain
TA	Tanba Block
TTT	Tango-Tajima terrain
UFZ	Uemachi Fault Zone
YBF	Yabu Fault
YDF	Yamada Fault
YGF	Yagi Fault
YKF	Yokkaichi Fault
YNF	Yanagase Fault

YSF	Yamasaki Fault
ZF	Zeze Fault
EUR	Eurasian

1. Introduction

High-resolution seismic velocity models enhance our comprehension of geologic structures and geodynamic processes in the Earth crust (Schippkus et al., 2018). In seismically active regions, such models can be used to accurately locate zones prone to crustal movement and seismic events, hence their utility in seismic hazard assessment and mitigation. As one of the most seismically active regions in southwest Japan, it is of great importance to understand the structural complexity and the dynamic processes that cause deformation within the Kinki region. In this quest, I constructed high-resolution crustal 3D S-wave velocity and azimuthal anisotropic models of the Kinki region in its entirety based on ambient noise tomography (ANT).

The emergence of ANT in recent years has revolutionized seismic tomography because, unlike the conventional earthquake-based surface wave tomography, this method is not restricted to areas with high seismicity and it is applicable to short periods compared to teleseismic studies (Shapiro and Campillo, 2004; Sabra et al., 2005; Shapiro et al., 2005; Sadeghisorkhani et al., 2016). The ANT method is premised on the retrieval of the Empirical Green's functions (EGFs) between seismic station pairs by cross-correlating continuous seismic waveforms (seismic ambient noise) recorded at those stations (e.g., Weaver and Lobkis, 2004; Shapiro et al., 2005; Boschi and Weemstra, 2015; Campillo and Roux, 2015). These EGFs can provide information about the structure of the crust between the seismic station pairs in the absence of earthquakes or active sources (Shapiro et al., 2005; Weaver and Lobkis, 2004), as they are dominated by surface waves in the microseism period band (Longuet-Higgings, 1950; Hasselmann, 1963).

Since its inception and the recent expansion of high-quality seismic arrays, the ANT method has been employed with proven efficacy in many applications and diverse geological settings (e.g., Lin et al., 2008; Nishida et al., 2008; Shapiro et al., 2005; Chen et al., 2018;

Kastle et al., 2018; Nimiya et al., 2020; Suemoto et al., 2020). All applications of ANT rely on the dispersive property of the surface waves and estimating dispersion curves between station pairs is pivotal in constructing 3D S-wave velocity and azimuthal anisotropy structures of the Earth.

In this thesis, I focus on modeling the shallow crustal structure at a scale of tens of kilometers using continuously recorded seismic waveforms by the 221 permanent and temporary stations (Iio et al., 2018; Katoh et al., 2018) deployed across the Kinki region. The 3D isotropic velocity models provide useful constraints on the geological heterogeneities within the crust and the upper mantle (e.g., Nakajima and Hasegawa, 2007; Matsubara et al., 2008; Nishida et al., 2008). In the Kinki region, however, the existing 3D isotropic S-wave velocity model (e.g., Nishida et al., 2008) focused mainly on deep, large-scale structures and could not sufficiently resolve the shallow crustal structures. Therefore, there is still a need for a detailed S-wave velocity model that resolves the shallow crustal structure and fine-scale geologic features in the Kinki region.

Deformation within the earth induces seismic anisotropy, both through the Shape-Preferred Orientation (SPO) of fault fabrics, pervasive cracks and layered geologic structures or through the Lattice-Preferred Orientation (LPO) of anisotropic minerals under strain or applied stress (Crampin and Chastin, 2003; Crampin and Peacock, 2008; Savage, 1999; Wang and Zhao, 2021). Seismic anisotropy estimated from dispersive surface waves thus provides insights into the deformational mechanisms in the crust and upper mantle at various scales (Montagner, 1994; Savage, 1999; Yao et al., 2010).

There are two types of seismic anisotropy: the radial and azimuthal anisotropy. Radial anisotropy describes the wave speed discrepancies between the vertically and horizontally polarized shear waves, irrespective of their propagation azimuth (Dreiling et al., 2018), and is estimated from the inversion of Love wave and Rayleigh wave dispersion. Azimuthal

anisotropy is, on the other hand, used to determine the S-wave velocity variations of the Rayleigh waves propagating in different azimuthal directions (Schaeffer et al., 2016; Liu et al., 2019). Here, I focus only on estimating the azimuthal anisotropic structure of the Kinki region. Existing azimuthal anisotropy models in this region were estimated using shear-wave splitting of natural earthquake (Kaneshima et al., 1987; Mizuno et al., 2001; Hiramatsu et al., 2010). However, these models could not resolve the variation of anisotropy with depth and the spatial resolution of anisotropy is limited by the sparse distribution of seismic events and stations used in those studies. In order to provide insight into the deformational mechanisms and the stress condition across the Kinki region, there is a need to estimate the azimuthal anisotropy structure of the Kinki region in its entirety at high lateral and vertical resolution.

This thesis is based on two papers that are dedicated to the ambient noise tomography method. It consists of six chapters. The second chapter discusses the geological setting of the study area, the third chapter focuses on the data and methods, the fourth chapter focuses on the results, discussion of the results makes chapter five, and lastly, the key findings of this study are presented as chapter six.

In paper one, continuously recorded seismic waveforms by the 221 permanent and temporary seismic stations deployed in the Kinki region were used to determine the S-wave velocity structure of the shallow crust in the Kinki region. Preprocessing of the dataset used involved partitioning the daily seismic waveforms into 30-minute-long segments with a 50% overlap and the removal of the instrumental response of each dataset. Next, I applied cross-correlation of the vertical component of the Rayleigh waves to estimate phase velocities in the period range of 1 to 20 s, using the zero-crossing method (Ekström et al., 2009). In this method, the real part of cross-correlation spectra is matched with an approximate Bessel function in the frequency domain.

The GSpecDisp software package was used to measure the phase-velocity dispersion up to the period corresponding to an interstation distance of one wavelength. Finally, the obtained dispersion data were inverted using a direct inversion method (DSurfTomo) proposed by Fang et al. (2015) to construct a high-resolution 3D S-wave velocity model. After the inversion, the results were interpreted and compared to other geophysical and geological information. S-wave velocity anomalies show significant correlation with earthquake hypocenter distribution and geologic structures (active fault systems, sedimentary basins and mountainous zones). The final S-wave velocity model provides insights into the complex geologic structures, their depth extent in the upper crust and earthquake faulting in the Kinki region.

In paper two, I used the same dispersion curves as those used in paper one. I applied a joint inversion method (i.e., DAzimSurfTomo) proposed by Liu et al. (2019) to estimate the first high-resolution 3D azimuthal anisotropic model of the shallow crustal structure in the Kinki region based on ambient noise tomography. Compared to the existing azimuthal anisotropy models obtained from shear-wave splitting measurements (Hiramatsu et al., 2010; Iidaka et al., 2016) in the Kinki region, I took advantage of a dense seismic array to estimate the 3D V_{SV} azimuthal anisotropy structure of the entire Kinki region at a high lateral and vertical resolution.

The inversion workflow using this joint inversion method is implemented in two steps. In the first step, the 3D isotropic velocity model is constructed by inverting Rayleigh wave phase velocities using a 3D direct inversion method (Fang et al., 2015). The second step involves using the 3D isotropic velocity model obtained in step one as an initial model in the joint inversion for both 3D azimuthal anisotropy and an additional isotropic velocity perturbation. To aid interpretation, the azimuthal anisotropy results are compared with the shear-wave splitting measurements (e.g., Hiramatsu et al., 2010; Iidaka et al., 2016), the

trajectories of the maximum horizontal compressional stress (e.g., Ukawa, 1982), the distribution of the principal strain rate axes estimated from the continuous GPS velocity field (Sagiya et al., 2000), and the distribution of earthquake hypocenters (Yano et al., 2017). The final 3D azimuthal anisotropy model provides important constraints on the dominant deformation mechanisms and the tectonic evolution of the study area.

2. Geologic setting

In the Kinki region, southwestern Japan, the Eurasian (EUR) plate overrides the subducting Philippine Sea (PHS) oceanic plate (Aoki et al., 2016). The southeastward movement of the incipient Amurian plate (Amur Plate) with respect to the EUR plate and a shift in the subduction direction of the PHS plate (Taira, 2001) has generated relatively new, large fault zones or continually reactivates the old ones, a process referred to as neotectonics (Barnes, 2008). A striking example of neotectonic faulting is the Median Tectonic Line (MTL), which has an E-W right-lateral strike-slip fault movement across the Kii Peninsula. The MTL divides the Kinki region into two zones with different characteristics and deformational styles (Matsushita, 1963; Sato et al., 2015; Okamura and Shishikura, 2020); the Inner Zone (northern part) and the Outer Zone (southern part).

On the one hand, the outer zone is characterized by four zonally arranged terrains from north to south: namely, the Sanbagawa metamorphic terrain, Chichibu terrain, Hidaka terrain, and Muro terrain (SMZ, CT, HT, and MT; Fig. 1a). This zone is characterized by undulating topographic pattern of mountainous and depressional zones, and active faults are scarce (Okamura and Shishikura, 2020). The Inner Zone is, on the other hand, characterized by the Neogene volcanic and sedimentary series of the Tango-Tajima terrain (TTT), the Yakuno intrusive rocks and marine formations of the Maizuru zone (MZ), Cretaceous granites of the Mino-Tanba terrain (MTT), and metamorphic and granitic rocks of the Ryoke terrain (RT; Fig. 1a) (Matsushita, 1963).

Huzita (1980) delineated a triangular-shaped neotectonics zone characterized by the E-W compression in the upper crust and undulating topography of alternating sedimentary basins and mountain ranges, called the Kinki triangle (shaded area in Fig. 1c). This tectonic zone provided Kinki region with its civilizational homelands, including the Osaka, Nara, Kyoto and Ise basins (Barnes, 2008). The Kinki triangle hosts a plethora of Quaternary active faults

predominantly oriented in the N–S direction and some NE–SW or NW–SE strike-slip faults (Huzita, 1980; Research Group for Active Faults of Japan, 1991; Sugiyama, 1992).

Furthermore, Sagiya et al. (2000) identified a NE-SW trending zone of high strain rate across the Inner Zone, designated the Niigata-Kobe Tectonic Zone (NKTZ). The NKTZ, just like the Kinki Triangle, has NE-SW-striking Quaternary fault zones which are oriented in the same direction as the NKTZ (Tamura et al., 2020) and many destructive earthquakes have occurred in this zone.

Around the Osaka area, numerous strike-slip and reverse active faults of diverse orientations exist (Research Group for Active Faults of Japan, 1991). The significance of these faults was highlighted by the highly catastrophic 1995 M_w 7.2 Kobe earthquake, which resulted from the strike-slip displacements on the Rokko-Active Fault Zone (Kanamori, 1995; Katao et al., 1997). In addition, a shallow crustal earthquake of M_w 5.6 occurred in 2018, proximal to the zone of intersection between the ATTL, the Uemachi and Ikoma fault zones (Kato and Ueda, 2019; Sato et al., 2009). These earthquakes are a testament to how susceptible life is to displacements along these fault zones and highlight the need to identify zones prone to strong crustal movement in a quest to minimize the effects of destructive earthquakes. Such zones include fault zones which are difficult to ascertain from surficial evidence, as well as active and new fault systems, which are likely to be the locus of future events.

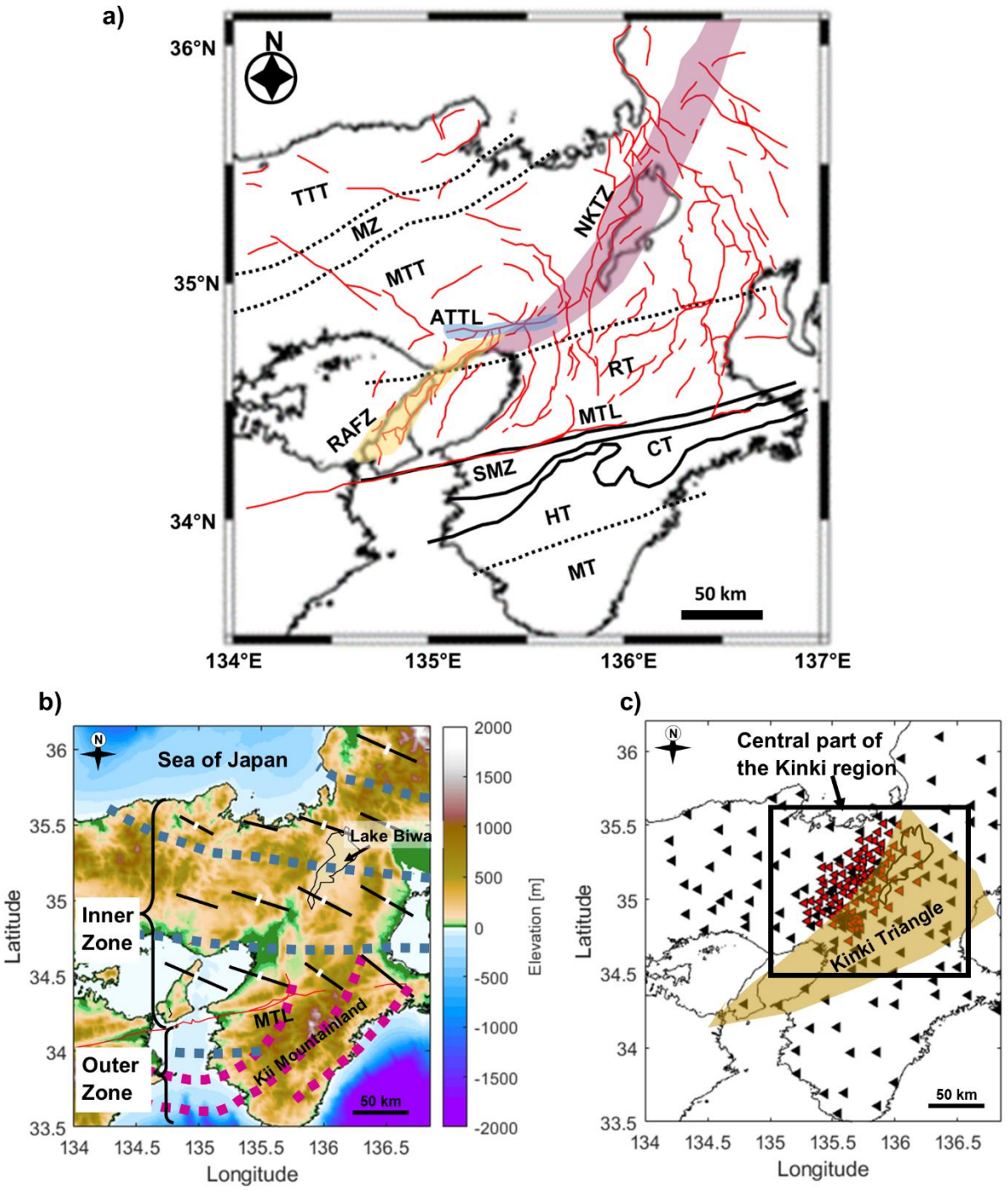

Fig. 1. (a) Map of the Kinki region showing the spatial distribution of tectonic structures. Red lines represent active faults (retrieved on 19 November 2021 from https://gbank.gsj.jp/subsurface/english/ondemand.php), thick purple, yellow, and light blue lines represent the Niigata-Kobe Tectonic Zone (NKTZ), Rokko Active Fault Zone (RAFZ), and the Arima-Takatsuki Tectonic Line (ATTL), respectively. Also shown are the locations of the Median Tectonic Line (MTL), and tectonic divisions of the Kinki region, comprising Tango-Tajima Terrain (TTT),

Maizuru Zone (MZ), Mino-Tamba Terrain (MTT), Ryoke Terrain (RT), Sanbagawa Metamorphic Zone (SMZ), Chichibu Terrain (CT), Hidaka Terrain (HT), and Muro Terrain (MT), (b) Topographic map of the Kinki region. Black and white bars show the principal strain rate axes (black bars: compression, white bars: extension) (Sagiya et al., 2000). Blue and magenta dashed lines indicate the trajectories of the maximum horizontal compressional stress and tensional stress, respectively (Ukawa, 1982), (c) The distribution of permanent (black triangles) and temporary stations (red triangles) deployed in the Kinki region. Red lines in (a) represent active faults (Research Group for Active Faults of Japan, 1991).

3. Data and Method

3.1 Data

I utilized the vertical component of continuously recorded seismic waveforms by the 221 permanent and temporary stations from April 1 to September 30 during the year 2019. The permanent stations included 78 Hi-net stations, 1 Kyushu University station, 1 Tokyo University station, 1 Nagoya University station, 10 AIST stations, 14 Kyoto University stations and 9 JMA stations, and temporary stations comprised 104 Kyoto University Manten project stations (Iio et al., 2018; Katoh et al., 2019), that are deployed across the central part of the Kinki region. I note that velocity type seismometers with the damping constant of 0.7 and the natural frequency of 2 Hz were used for the Manten Project stations. The corresponding poles (p_1 and p_2) and zeros (z_1 and z_2) are p_1= -8.7965-8.9742i, p_2= -8.7965+8.9742i, z_1=z_2=0.

By combining these set of stations, I obtained a dataset with adequate short-period surface waves ray paths coverage and subsequent 3D S-wave velocity and azimuthal anisotropy models of high-resolution. Firstly, I computed the cross-correlation of ambient noise to extract surface waves propagating between pairs of seismic stations. Rayleigh wave phase velocity measurements between station pairs were then estimated using the zero-crossing method (Ekström et al., 2009). Finally, the shallow crustal 3D S-wave velocity and 3D azimuthal anisotropy models were constructed by applying the direct surface wave inversion method (Fang et al., 2015) and a joint inversion method (Liu et al., 2019), respectively.

3.1.1 Pre-processing and cross-correlation

After partitioning daily seismic waveforms into 30-minute-long segments with a 50% overlap, the instrumental response of each dataset was eliminated. Next, cross-correlation spectra for all the seismic stations pairs were computed from the resulting seismograms (Ekström, 2014). Then, the daily cross-correlation spectra were stacked over a six-month-long time series. The

time-domain cross-correlations computed from stacked cross-correlation spectra clearly shows the Rayleigh wave propagation between station pairs (Fig. 2).

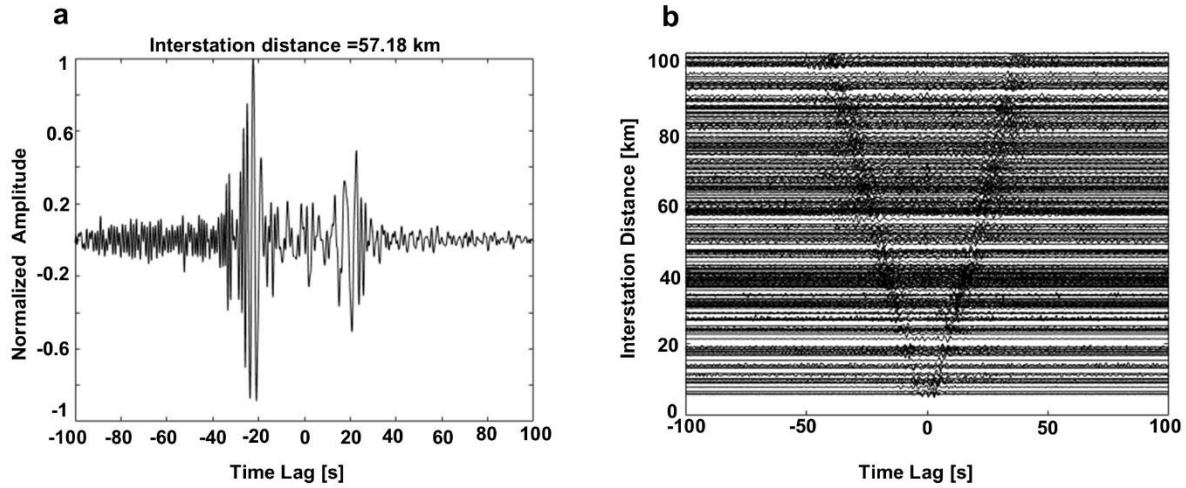

Fig. 2. Cross-correlation functions showing the empirical Green's functions between station pairs for frequencies ranging from 0.05 to 1.0 Hz. **a** Cross-correlation function for a station pair with an interstation distance of 57.18 km (shown in Fig. 3b), and **b** stacked cross-correlation functions from randomly selected station pairs, exhibiting Rayleigh wave propagation between paired seismic stations.

3.2 Dispersion measurements

Phase velocity measurements can be conducted in either the time domain or frequency domain. The time domain analysis requires the high-frequency approximation and only considers those interstation distances exceeding three wavelengths (λ) (Bensen et al., 2007; Lin et al., 2008; Yao et al., 2006). In contrast, the frequency domain approach has no theoretical limitation for interstation distances (i.e., zero-crossing method; Ekström et al., 2009). As such, interstation distances up to approximately one wavelength can be practically used (Ekström et al., 2009; Tsai and Moschetti, 2010).

In this study, I used the zero-crossing method to estimate phase velocity measurements between station pairs. This method is based on modeling cross-correlation spectra by the spatial

autocorrelation (SPAC) method (Aki, 1957; Asten, 2006) and uses the zero-crossing frequencies of the real part of the cross-correlation spectra. The SPAC method is premised on the assumption that ambient noise sources are homogeneously distributed, and that ambient noise is predominantly surface waves (Aki, 1957). Under this assumption, a Bessel function of the first kind and zeroth order can be used to model the real part of the vertical cross-correlation spectra as follows:

$$Real\big(CCS(f,x)\big) = J_0\left(\frac{2\pi f x}{C_R(f)}\right), \quad (1)$$

where CCS is the cross-spectrum, f is the frequency, x represents the interstation distance, J_0 represents the Bessel function of the first kind and zeroth order, and $C_R(f)$ represents the Rayleigh wave phase velocity. In the zero-crossing method, I only focus on the zero crossing points where both sides of Eq. (1) should be zero. The zero-crossing points are not sensitive to fluctuations in the power spectrum of the background noise and non-linear filtering in the data processing (Ekström et al., 2009). Using zero crossings simplifies phase velocity measurements and stabilizes the estimation of phase velocities because phase velocity estimation is not affected by incoherent noise (Cho et al., 2021).

If f_n represents the frequency of the observed nth zero crossing point of the cross-correlation spectrum, and Z_n denotes the nth zero of the Bessel function, each f_n can be matched with the zero crossing points of the Bessel function to have all the possible phase velocity dispersion curves according to the following equation:

$$C_m(f_n) = \frac{2\pi f_n x}{Z_{n+2m}}, \quad (2)$$

where m representing the number of missed or additional zero crossing points, takes the values (0, ±1, ±2,…). Applying Eq. (2) for all observed values of f_n yields numerous possible dispersion curves.

I used the GSpecDisp package (Sadeghisorkhani et al., 2018) to estimate phase-velocity dispersion curves uniquely by the zero-crossing method from the stacked cross-correlations. To reduce noise effects in the correlations, a velocity filter of 1–4.5 km/s with a taper interval of ~0.2 km/s was applied. Then, spectral whitening was applied to each correlation for amplitude equalization (Sadeghisorkhani et al., 2018). With many possible phase velocities occurring at each frequency with regard to Eq. (2) (colored dots; Fig. 3a), it is difficult to uniquely determine the phase velocity dispersion curves without using a reference velocity dispersion curve as a guide. To circumvent this, I picked the dispersion curve appearing closest to the reference dispersion curve manually. In the GSpecDisp, average velocities can be estimated by combining all cross-correlation spectra (average velocity module). Average phase velocities in the period ranging from 2 to 8 s were estimated and the result was used as a reference velocity for picking dispersion curves between station pairs (dashed black dots; Fig. 3a). Finally, phase-velocity dispersion curves between all the possible station pairs (red circles in Fig. 3a) were estimated.

For the dataset used in this study, the maximum measurable period required an interstation distance (x, in km) of at least three wavelengths (λ), defined as the r/λ ratio in GSpecDisp ($x/\lambda \geq 3$). For each cross-correlation function, the signal-to-noise ratio (SNR) was defined as the ratio between maximum absolute amplitude in the signal window (between arrival times corresponding to waves with 1 and 4.5 km/s) and the root mean square amplitude in the noise time window (between 500 and 700 s). I utilized a SNR threshold of 10 to reject correlations with low signal. In the end, I obtained a total of 23,647 dispersion curves (Fig. 3c).

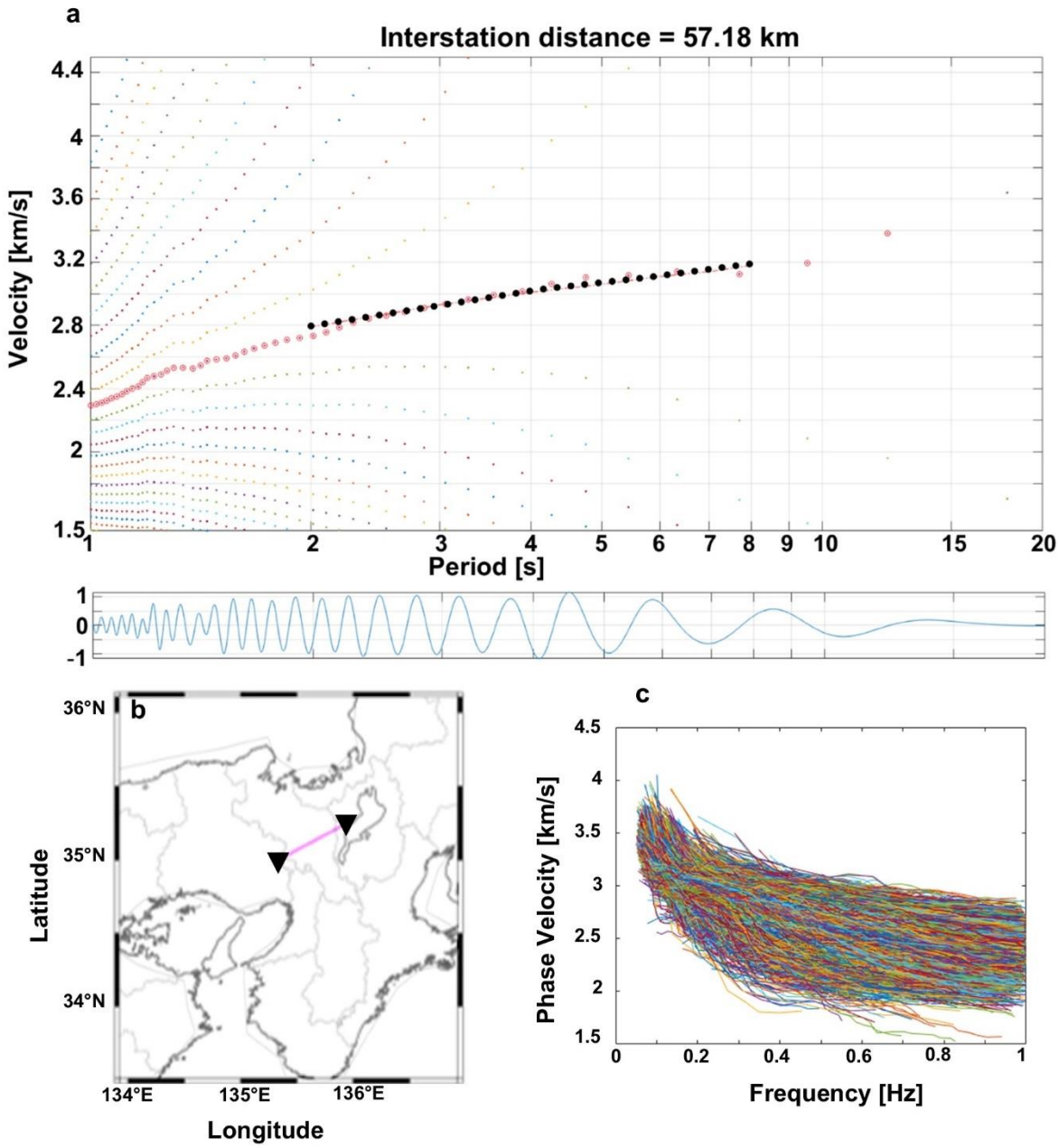

Fig. 3. a Observed phase velocity dispersion curves (upper panel) and the real part of the cross-correlation spectrum (lower panel). Red and black circles in the upper panel represent the selected points of the dispersion curve and the average phase-velocity dispersion curve for the region, respectively. **b** Location of the station pair for which dispersion data are displayed in **a**. **c** Phase-velocity–frequency plot showing the 23,647 selected dispersion curves for all the station pairs used.

3.3 3D S-wave velocity model by a direct inversion technique

Ambient noise tomography using phase velocity dispersion curves typically involves a two-step procedure. Firstly, 2D phase velocity maps are constructed by travel-time tomography at discrete frequencies. Secondly, pointwise inversion of dispersion data for 1D profiles of S-wave velocity as a function of depth at each grid point is implemented. Combining multiple 1D profiles subsequently yields the 3D S-wave velocity structure (Shapiro and Ritzwoller, 2002; Yao et al., 2008). Nonetheless, a 3D S-wave velocity structure can equally be estimated by direct inversion of dispersion data without the intermediate step of constructing 2D phase velocity maps (Boschi and Ekström, 2002; Feng and An, 2010; Pilz et al., 2012). Typically, these direct inversion approaches do not update the ray paths and sensitivity kernels for the newly constructed 3D models.

To estimate the 3D S-wave velocity structure from phase velocity dispersion data, I applied a direct surface wave tomography method (DSurfTomo), which is based on frequency-dependent ray-tracing and a wavelet-based sparsity-constrained inversion (Fang et al., 2015). This approach circumvents the intermediate step of constructing 2D phase velocity maps and iteratively updates the sensitivity kernels of period-dependent dispersion data (Fang et al., 2015). Furthermore, it accounts for the ray-bending effects of period-dependent ray paths by using the fast-marching method (Rawlinson and Sambridge, 2004). Accounting for such effects in the inversion is especially useful for short-period surface waves, which are significantly sensitive to the highly complex shallow crustal structure (Fang et al., 2015; Gu et al., 2019). Therefore, this approach is a well-suited tool for determining the shallow-crustal structure of the Kinki region using short-period surface-waves dispersion data.

In tomographic inversion, the objective is to find a model **m** that minimizes the differences $\delta t_i(f)$ between the measured travel times $t_i^{obs}(f)$ and the calculated travel times $t_i(f)$ from the model for all frequencies f. The travel time for path i is given as

$$\delta t_i(f) = t_i^{obs}(f) - t_i(f) \approx -\sum_{k=1}^{K} v_{ik} \frac{\delta C_k(f)}{C_k^2(f)}, \quad (3)$$

where $t_i(f)$ represents the computed travel times from a reference model which can be updated during the inversion, v_{ik} denotes the bilinear interpolation coefficients along the ray path associated with the *i*th travel-time data, $C_k(f)$ is the phase velocity and its perturbation $\delta C_k(f)$ at the *k*-th two-dimensional surface grid node at frequency f (Fang et al., 2015). Surface wave dispersion is primarily sensitive to S-wave velocity. However, short-period Rayleigh wave dispersion is also sensitive to the compressional (P-wave) velocity in the shallow crustal structure (Fang et al., 2015). The P-wave velocity perturbations together with mass density are therefore explicitly included in the calculation of surface wave dispersion using empirical relationships given by Brocher (2005), with R'_α and R'_ρ as scaling factors, leading to the following equation:

$$\delta t_i(f) = \sum_{k=1}^{K} \left(-\frac{v_{ik}}{C_k^2}\right) \sum_{j=1}^{J} \left[R'_\alpha(z_j) \frac{\partial C_k}{\partial \alpha_k(z_j)} + R'_\rho(z_j) \frac{\partial C_k}{\partial \rho_k(z_j)} + \frac{\partial C_k}{\partial \beta_k(z_j)}\right]\Bigg|_{\theta_k} \delta\beta_k(z_j) =$$

$$\sum_{l=1}^{M} G_{il} m_l, \quad (4)$$

where θ_k denotes the one-dimensional (1D) reference model at the *k*-th surface grid node, $\alpha_k(z_j)$, $\rho_k(z_j)$, and $\beta_k(z_j)$ represent the P-wave velocity, the mass density, and the S-wave velocity, respectively. *J* indicates the number of grid points in the depth direction, and $M = KJ$ represents a sum of all the model grid points. Equation (4) can be written as follows:

$$\mathbf{d} = \mathbf{Gm}, \quad (5)$$

where **d**, **G**, and **m** represent the surface wave travel-time residual vector for all ray paths and discrete frequencies, data sensitivity matrix, and the model parameter vector, respectively. The damping and weighting parameters were applied to balance data fitting and smoothing regularization. In this study, these inversion parameters were selected on a trial-and-error basis

considering the diverse patterns in inverted S-wave velocity models (weakly smoothed and strongly smoothed S-wave velocity models are shown in Fig. 11 and Fig. 12, respectively).

I conducted two inversions with coarser and finer grid intervals between grid points in each horizontal direction for the entire Kinki region and the northern part of the Kinki region (with dense distribution of seismic stations), respectively. The entire Kinki region was parameterized into 53 by 58 grid points on the horizontal plane with 0.055° intervals between grid points in each horizontal direction, whereas the northern part was parameterized into 27 by 75 grid points on the horizontal plane with 0.025° grid point intervals in the latitude and longitude directions. For both inversions, I used 9 grid points along the depth direction (i.e., 0, 0.6, 1.2, 2, 4, 6, 9, 12 and 16 km) and used dispersion data within a frequency bandwidth of 0.0714 - 1.0 Hz.

Empirically, the fundamental mode Rayleigh wave phase velocity is primarily sensitive to 1.1 × S-wave velocity at a depth of about 1/3 multiplied by its corresponding wavelength (λ) (Fang et al., 2015; Foti et al., 2014; Hayashi, 2008). Consequently, the observed Rayleigh wave phase velocities were averaged at depths of about $1/3\lambda$ and then multiplied them by 1.1 to construct the initial S-wave velocity model of the study area (i.e., a one-third wavelength transformation; Fig. 4). To account for the influence of topography on the S-wave velocity models, I subtracted altitude value from the depth value at each grid point. Elevation values were smoothed by applying a moving 2D average smoothing filter with a window size of 18 km by 18 km before correcting for topographic effects. The depth shown in my final 3D S-wave velocity models is the depth below sea level (S-wave velocity models without topographic correction are shown in Figs. 13, 14 and 15).

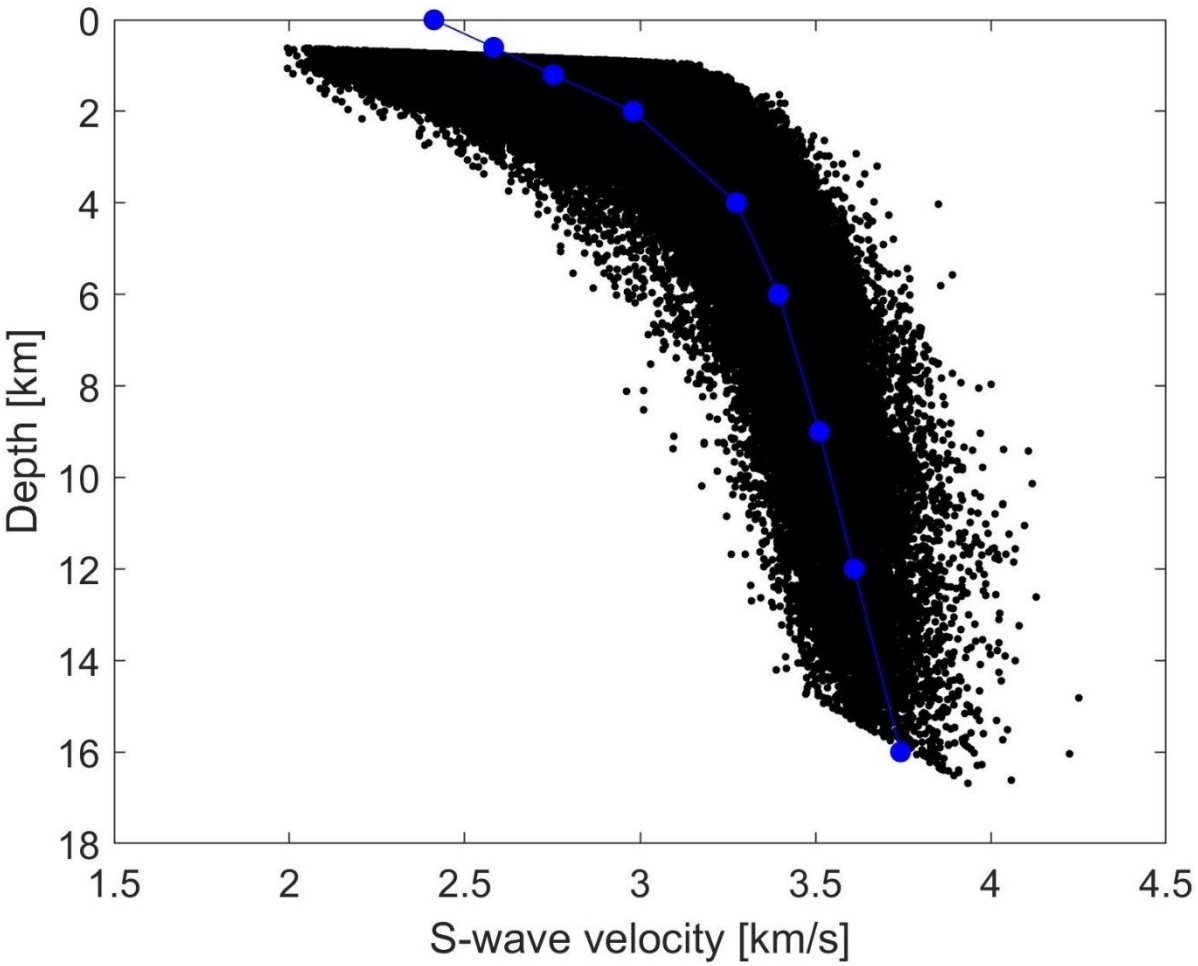

Fig. 4. The initial S-wave velocity model used as a reference in the inversion process. The blue line and blue dots represent the average S-wave velocity model. The black dots represent all the interstation Rayleigh wave phase-velocity dispersion curves measured using the zero-crossing method transformed to a depth–S-wave velocity approximation.

3.4 Direct inversion for 3D azimuthal anisotropy

I estimated the 3D azimuthally anisotropic Vsv structure from phase velocity dispersion data by applying a direct joint inversion technique proposed by Liu et al. (2019), abbreviated DAzimSurfTomo. For the conventional two-step anisotropic inversion approaches (Montagner and Nataf, 1986; Montagner and Tanimoto, 1991; Yao et al., 2010), the initial step of phase velocity tomography involves estimating the isotropic and azimuthally anisotropic phase velocity variations by utilizing mixed-path dispersion data. In the second step, the depth-

dependent S-wave velocity and its azimuthal anisotropy can be obtained by inverting the pointwise dispersion curve with azimuthal anisotropy (Liu et al., 2019). By contrast, this direct joint inversion approach circumvents the intermediate step of constructing 2D phase velocity azimuthal anisotropy maps (Liu et al., 2019). Additionally, it accounts for the frequency-dependent ray-bending effect using the fast-marching method (Rawlinson and Sambridge, 2004) in estimation of frequency-dependent Rayleigh wave propagation in the first step of isotropic inversion (Fang et al., 2015; Li et al., 2016), and the second step of joint inversion, where the effect of weak azimuthal anisotropy on the raypaths is ignored (Liu et al., 2019). Accounting for the ray-bending effects in the inversion makes this approach valid for complex heterogeneous media (Yang and Hung, 2005).

The raypath (AB) of Rayleigh waves between source A and receiver B may detour from the great-circle path due to structural heterogeneity (Liu et al., 2019). Taking the variation of azimuthal anisotropy ψ into account, the travel time $t_{AB}(\omega)$ based on ray theory can be expressed as

$$t_{AB}(\omega) = \int_{l_{AB}} \frac{1}{c(l,\omega,\psi)} dl \,, \tag{6}$$

where $c(l, \omega, \psi)$ repesents the local phase velocity along the actual raypath l_{AB}, ω is the angular frequency and ψ indicates the azimuth of Rayleigh wave propagation. The discretized version of Eq. (6) is given as

$$t_{AB}(\omega) = \sum_{p=1}^{P} \frac{1}{c_p(\omega,\psi)} \Delta l, \tag{7}$$

where P is the total number of path segments, p is the index of path segments, and $c_p(\omega, \psi)$ represents the phase velocity for the path segment Δl along raypath AB. For a weak anisotropic medium, the Rayleigh wave phase velocty $c(\omega, \psi)$ in Eq. (7) can be expressed as (Smith and Dahlen, 1973):

$$c_p(\omega,\psi) = c_0(\omega,p) + a_1(\omega,p)cos2\psi + a_2(\omega,p)sin2\psi + a_3(\omega,p)cos4\psi +$$

$$a_4(\omega,p)sin4\psi \quad (8)$$

where, $c_0(\omega)$ represents the isotropic phase velocity at the angular frequency ω, and $a_{1,2}$ and $a_{3,4}$ are the amplitudes of 2ψ (180° periodicity) and 4ψ (90° periodicity) terms, respectively. As suggested in Montagner and Nataf (1986), the 4ψ terms in Eq. (8) are insignificant for Rayleigh waves.

Due to the variations in effective transversely isotropic moduli (ETI) and azimuthally anisotropic moduli (AA) relative to the reference moduli, phase velocity perturbation can be decomposed into three parts:

$$c(\omega,\psi) = c_0^{ref}(\omega) + \delta c_k^{ETI}(\omega) + \delta c_k^{AA}(\omega,\psi), \quad (9)$$

where $c_0^{ref}(\omega)$ is the prediction from reference moduli. The study area is parameterized with a regular grid of *K* points in total. The 1D transversely layered model at each grid point *k* is then taken as a reference with the isotropic phase velocity given by c_0^k. For a tomographic model, the objective is to minimize the difference between the measured traveltimes $t_i^{obs}(\omega)$ and the calculated traveltimes from the model for all frequencies ω. With the isotropic phase velocity $c_0^k(\omega)$ as a reference, the traveltime difference between the measurement $t_i^{obs}(\omega)$ and the isotropic reference model prediction $t_i^{ref}(\omega)$ can be expressed as

$$\delta t_i(\omega) = t_i^{obs}(\omega) - t_i^{ref}(\omega) \approx \sum_{k=1}^{K} \frac{R_k}{\left(c_0^k(\omega)\right)^2}\left(\delta c_k(\omega) + a_1^k(\omega)cos2\psi + a_2^k(\omega)sin2\psi\right)$$

$$= \sum_{k=1}^{K} \frac{R_k}{\left(c_0^k(\omega)\right)^2}\left(\delta c_k^{ETI}(\omega) + \delta c_k^{AA}(\omega,\psi)\right). \quad (10)$$

where R_k is the coefficient of interpolation.

Following Liu et al. (2019), the effective transversely isotropic perturbation of Rayleigh wave phase velocity can be expressed as

$$\delta c_k^{ETI}(\omega) = \int_0^{\infty} \left(\frac{\partial c_k(\omega)}{\partial A_k(z)} \delta A_k(z) + \frac{\partial c_k(\omega)}{\partial C_k(z)} \delta C_k(z) + \frac{\partial c_k(\omega)}{\partial L_k(z)} \delta L_k(z) + \frac{\partial c_k(\omega)}{\partial F_k(z)} \delta F_k(z) \right) dz, \quad (11)$$

where the four parameters *A*, *C*, *L*, and *F* together with another, *N*, represent parameters of the transversely isotropic medium. According to Montagner and Nataf (1986), the azimuthally anisotropic perturbation in the Rayleigh wave phase velocities can be approximated by

$$\delta c_k^{AA}(\omega, \psi) \approx \int_0^{\infty} \left[\left(B_c^k \frac{\partial c_k(\omega)}{\partial A_k(z)} + G_c^k \frac{\partial c_k(\omega)}{\partial L_k(z)} \right) cos2\psi + \left(B_s^k \frac{\partial c_k(\omega)}{\partial A_k(z)} + G_s^k \frac{\partial c_k(\omega)}{\partial L_k(z)} \right) sin2\psi \right] dz, \quad (12)$$

where B_c, B_s, G_c, and G_s represent the 2ψ azimuthal variations of *A* and *L*, respectively (Liu et al., 2019; Montagner and Nataf, 1986). After substituting Eqs. (11) and (12) into Eq. (10), the traveltime perturbation at all frequencies $\delta t_i(\omega)$ is obtained (Liu et al., 2019); a solution that can be represented in the form

$$\mathbf{d} = \mathbf{Gm} = \mathbf{G} \left[\delta\beta_1(z_1) \dots \delta\beta_1(z_J) \dots \delta\beta_K(z_J) \frac{G_c^1(z_1)}{L_1(z_1)} \dots \frac{G_c^1(z_J)}{L_1(z_J)} \dots \frac{G_c^K(z_J)}{L_K(z_J)} \frac{G_s^1(z_1)}{L_1(z_1)} \dots \frac{G_s^1(z_J)}{L_1(z_J)} \dots \frac{G_s^K(z_J)}{L_K(z_J)} \right]^T. \quad (13)$$

where $\boldsymbol{d}$ represents the vector of the traveltime residuals for all frequencies and all paths, $\boldsymbol{G}$ is the data sensitivity matrix, and $\boldsymbol{m}$ is the model parameter vector. Equation 13 is then solved using the LSQR algorithm (Paige and Saunders, 1982) with the regularized inversion system as:

$$\begin{bmatrix} \boldsymbol{G}_{iso} & \boldsymbol{G}_{AA} \\ \lambda_1 \boldsymbol{L}_{iso} & \mathbf{0} \\ \mathbf{0} & \lambda_2 \boldsymbol{L}_{AA} \end{bmatrix} \begin{bmatrix} \boldsymbol{m}_{iso} \\ \boldsymbol{m}_{AA} \end{bmatrix} = \begin{bmatrix} \boldsymbol{d} \\ \mathbf{0} \\ \mathbf{0} \end{bmatrix}, \quad (14)$$

where $\boldsymbol{G}_{iso}$, $\boldsymbol{G}_{AA}$, $\boldsymbol{m}_{iso}$, and $\boldsymbol{m}_{AA}$ represent the isotropic and azimuthal anisotropic data sensitivity matrices and model parameter vectors, respectively, $\boldsymbol{L}_{iso}$ and $\boldsymbol{L}_{AA}$ are the isotropic

and azimuthally anisotropic roughening matrices, and λ_1 and λ_2 are the weighting parameters balancing data fitting and model regularization. Since the isotropic *Vsv* model is iteratively updated, new depth-dependent sensitivity kernel matrices and new raypaths for all isotropic and anisotropic parameters are also updated in each iteration.

The inversion workflow using the DAzimSurfTomo method (Liu et al., 2019) is implemented in two stages. Firstly, the 3D isotropic *Vsv* model is obtained by inverting Rayleigh wave phase velocities using a 3D direct inversion method (Fang et al., 2015). Then, the isotropic *Vsv* model obtained from the first step is used as the 3D reference model to perform a joint inversion iteratively for both 3D isotropic *Vsv* perturbation and azimuthal anisotropy. According to Liu et al. (2019), the azimuthal anisotropic S-wave velocity $\hat{V}_{SV}$ can be approximated by

$$\hat{V}_{SV} \approx V_{SV}\left(1 + \frac{G_c}{2L}cos2\psi + \frac{G_s}{2L}sin2\psi\right) = V_{SV}[1 + A_{SV}cos2(\psi - \emptyset)], \quad (15)$$

where V_{SV} represents the isotropic part of $\hat{V}_{SV}$, A_{SV} is the magnitude of azimuthal anisotropy, $\emptyset$ represents the azimuth of fast polarization axis, which ranges from 0° to 180° clockwise from the north (Chen et al., 2015). A_{SV} and $\emptyset$ can be represented as

$$A_{SV} = \frac{1}{2}\sqrt{\left(\frac{G_s}{L}\right)^2 + \left(\frac{G_c}{L}\right)^2}, \quad (16)$$

$$\emptyset = \frac{1}{2}tan^{-1}\left(\frac{G_s}{G_c}\right). \quad (17)$$

Firstly, I performed the inversion for the Kinki region in its entirety. Here, the inversion area was parameterized into 55 by 60 grid points with lateral grid interval of 0.5° and set 6 grid points at variable intervals along the depth direction (0, 1, 3, 6, 10, and 16 km). The second inversion area is the central part of the Kinki region (shown in Fig. 1c), where seismic stations are densely distributed. This second inversion was parameterized into 42 by 57 grid points with lateral grid point intervals of 0.03° and 8 grid points along the vertical direction (0.0, 0.6, 1.8,

3.5, 6.0, 10.0, 15.0, and 20.0 km). The damping and weighting parameters were selected on a trial-and-error basis and applied to balance data fitting and smoothing regularization.

For both inversions, I used dispersion data within a frequency range of 0.0714 - 1.0 Hz. Altitude value was subtacted from the depth value at each grid point in order to account for the influence of topography on the isotropic Vsv and azimuthal anisotropic models. Elevation values were smoothed by applying a moving 2D average smoothing filter with a window size of 18 km by 18 km before correcting for topographic effects.

4. Results

4.1 Raypath coverage

Following the dispersion data inversion step, I ensured reliability of my measurements by plotting the spatial ray paths coverage in the study area (Fig. 5). From Fig. 5, it is apparent that the ray paths density is sufficient to resolve small-scale geological features, especially in the most central part of the study area where seismic stations are densely distributed. At the edges, however, the ray paths coverage is slightly limited.

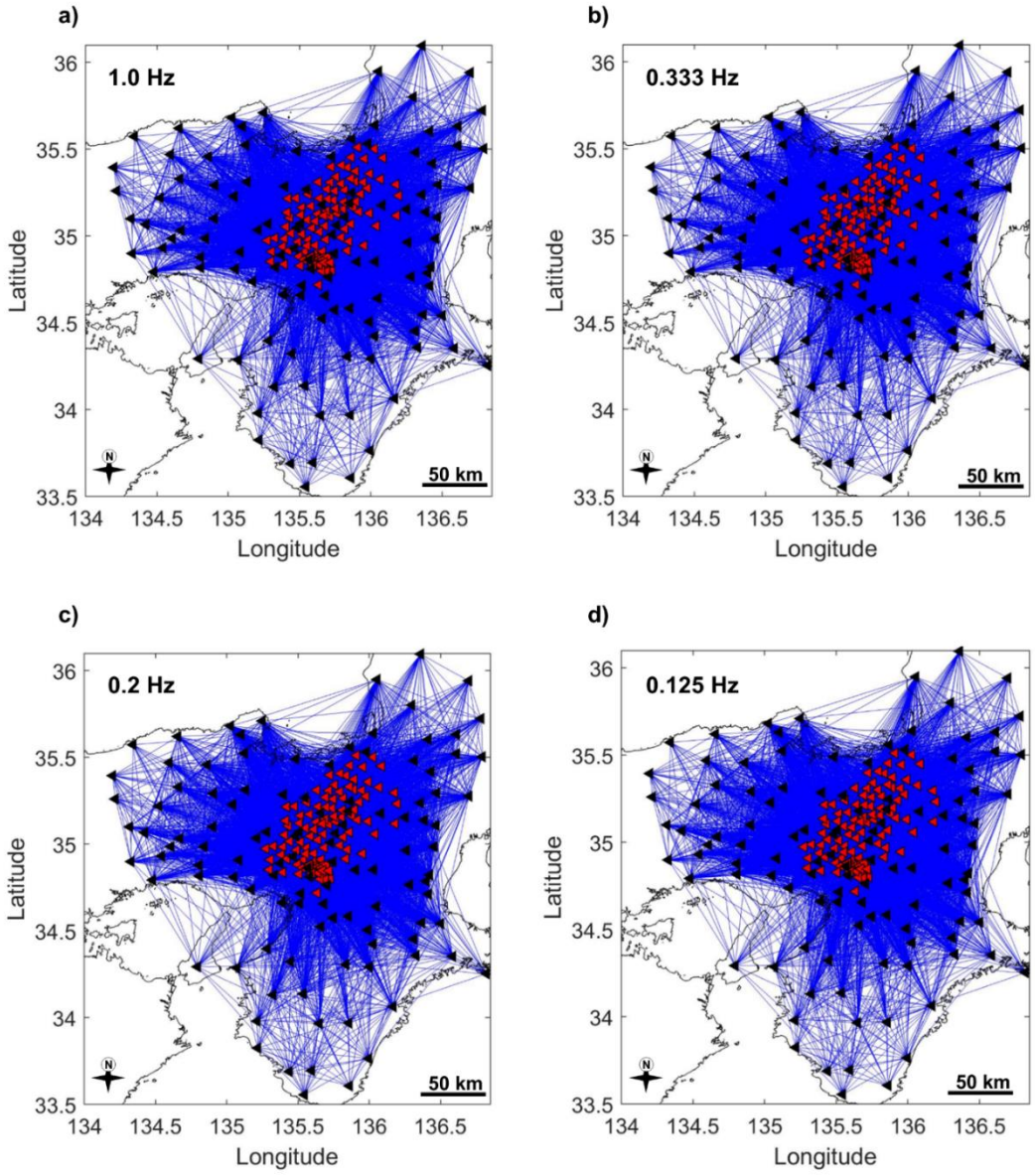

Fig. 5. Raypaths coverage derived from the inversion model at four frequencies: (a) 1.0 Hz, (b) 0.333 Hz, (c) 0.2 Hz and (b) 0.125 Hz. Black and red triangles represent the locations of permanent and temporary seismic stations, respectively. Blue lines represent the ray paths.

4.2 Checkerboard resolution test

I corroborated reliability of my S-wave velocity model by conducting a checkerboard resolution test using anomalies of ~0.12° (~13 km; Fig. 6a-c), ~0.2° (~22 km; Fig. 6d-f) and ~0.4° (~44 km; Fig. 6g-i) for the entire Kinki region, with an amplitude of the velocity anomaly set to ~5%. The checkerboard resolution test (Fig. 6a-c) reveals that tectonic and geological features of about 13 km could be well resolved in the central part of the study area where temporary stations are densely distributed, and anomalies of about 22 km (Fig. 6d-f) could be observed in most parts of the study area, whereas anomalies of about 44 km (Fig. 6g-i) could be resolved across the entire Kinki region.

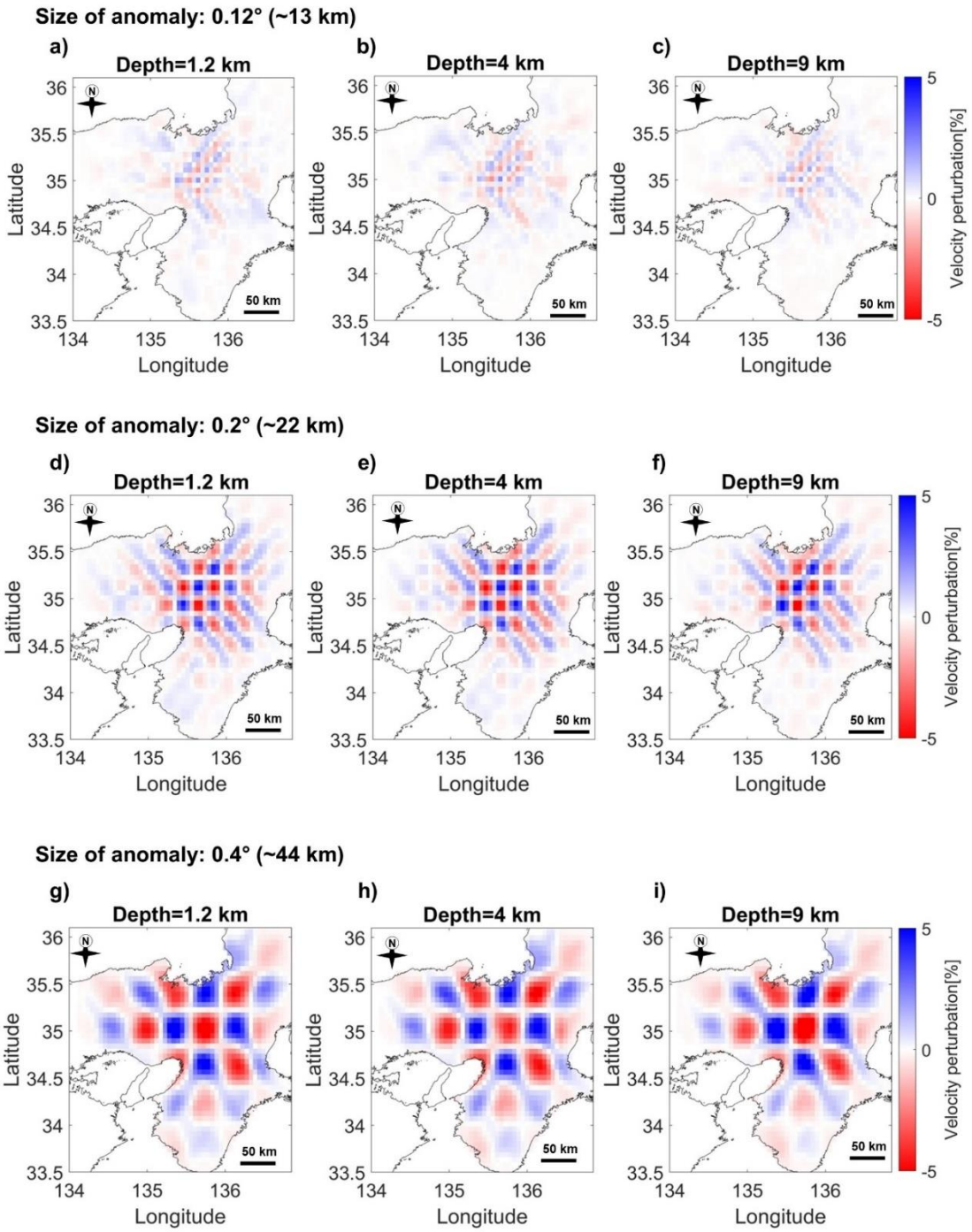

Fig. 6. Horizontal velocity perturbation slices of the checkerboard resolution test results with anomalies of three different sizes: **a-c** anomaly size of about 0.12° (~13 km), **d-f** anomaly size of about 0.2° (~22 km), and **g-I** anomaly size of about 0.4° (~44 km). The velocity amplitude was ~5%. Depth is shown above each horizontal slice.

As for anisotropy, I conducted checkerboard resolution tests (Figs. 7 and Fig. 8) with synthetic input models composed of alterning high and low velocity anomalies and fast polarization axes oriented north and east to assess the capacity of the dataset used in this study for resolving isotropic and anisotropic structures. The anomaly size for both the 3D isotropic Vsv and anisotropic models was set to be ~0.4° (~44.4 km; Fig. 7a) and ~0.15° (~16.5 km; Fig. 8). The isotropic velocity perturbation is ±4 % and anisotropic anomalies with magnitude of 6 % and 4 % for the entire Kinki region and the central part of the Kinki region, respectively, with orthogonal orientations assigned to adjacent cells (north and south; Fig. 7b and Fig. 8).

The checkerboard resolution test here reveals that isotropic anomalies of the size 0.15° (Figs. 7c, f) in both longitude and latitude directions can be recovered sufficiently in the central part of the study area where dense temporary stations are deployed, demonstrating that the density of ray path coverage is sufficient in this area. However, even isotropic anomalies of the size of about 0.4° (~44.4 km) laterally are poorly resolved on the edges and the southern part of the Kinki region (Figs. 8c, f). The poor resolution on the edges and the southern part of the study area can be attributable to sparsely distributed seismic stations in those areas. For anisotropic anomalies (Figs. 8d, f), anisotropy magnitude of about 4 % and the orientations of the fast polarization axes could be well recovered beneath the densely distributed temporary stations (Fig. 1c). However, the strength of anisotropy is significantly weaker and there is increased deviation of the fast axes orientations on the edges and the southern part of the study area, where the raypaths coverage is insufficient.

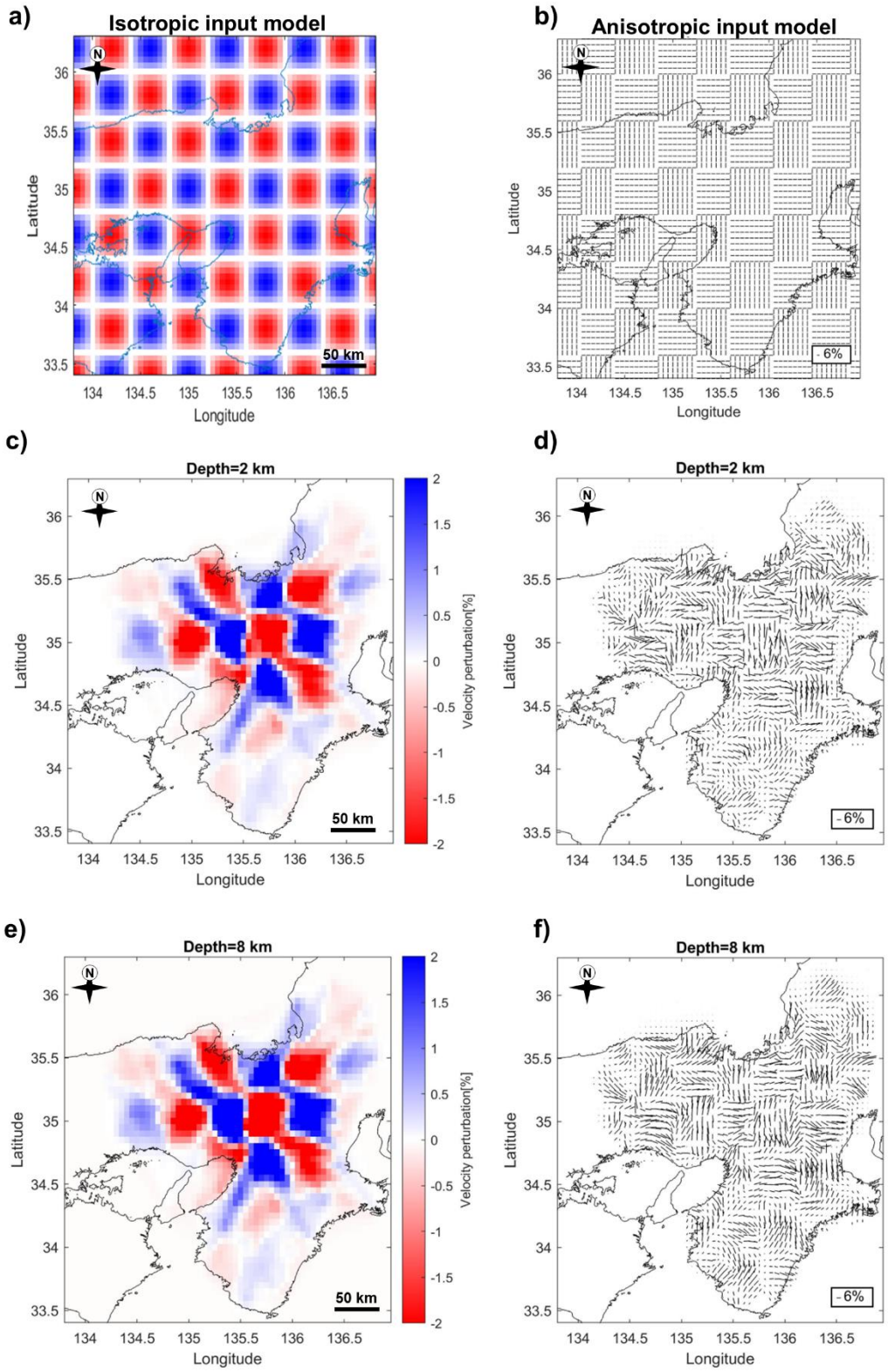

Fig. 7. Checkerboard resolution test results for the entire Kinki region: (a) 0.4° by 0.4° horizontal anomaly sizes of the isotropic velocity checkerboard input model, (b) anisotropic input model of anomaly size 0.4° by 0.4° and fast polarization axes that are oriented perpendicular to each other (north

and east), (c) and (e) are the recovered isotropic velocity models at 2 and 8 km depth slices, respectively. The color bar (in percent) represents the isotropic velocity perturbation with respect to the reference velocity model, (d) and (f) show the recovered models at 2 and 8 km depth levels, respectively, recovered from inversion of the input anisotropy model in (b).

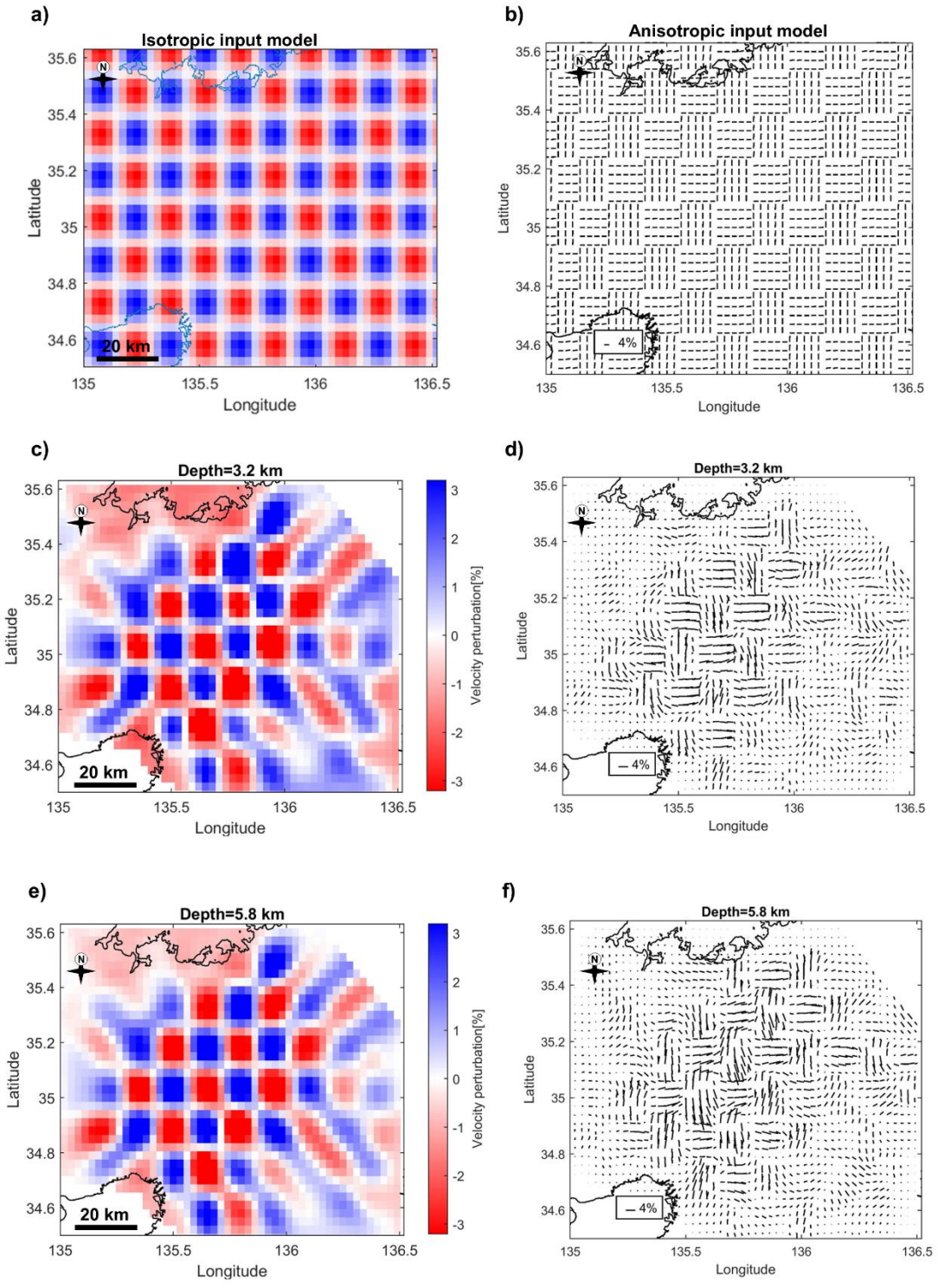

Fig. 8. Checkerboard resolution test results for the central part of the Kinki region (Fig. 1c). (a) 0.15° by 0.15° horizontal anomaly sizes of the isotropic velocity checkerboard input model, (b) anisotropic input model of anomaly size 0.15° by 0.15° and fast polarization axes that are oriented perpendicular to each other (north and east), (c) and (e) are the recovered isotropic velocity models at 3.2 and 5.8 km depth slices, respectively. The color bar (in percent) represents the isotropic velocity perturbation with respect to the reference velocity model, (d) and (f) show the recovered models at 3.2 and 5.8 km depth levels, respectively, recovered from inversion of the input anisotropy model in (b).

4.3 Spatial distribution of S-wave velocities

Figure 9 displays selected horizontal slices (map views) at different depths, exhibiting the lateral distribution of S-wave velocities within the study area. The third dimension (depth, in km) is given in the numerical form above each horizontal slice. Significant S-wave velocity heterogeneities are apparent and are discussed in the following sections. These anomalies highlight tectonic and geologic features associated with the study area.

Two broad high-velocity anomalies can be observed in the displayed horizontal slices. The first anomaly (marked NM, Fig. 9d) appears to be trending in the NE–SW direction, whereas the second high-velocity anomaly (marked KM) occurs from the southern side of the study area, trending roughly NE–SW across the MTL. These anomalies agree with the results of Nishida et al. (2008), which indicated comparable S-wave velocities in those areas, particularly at a depth of about 2 km (see Fig. 20 in Nishida et al., 2008).

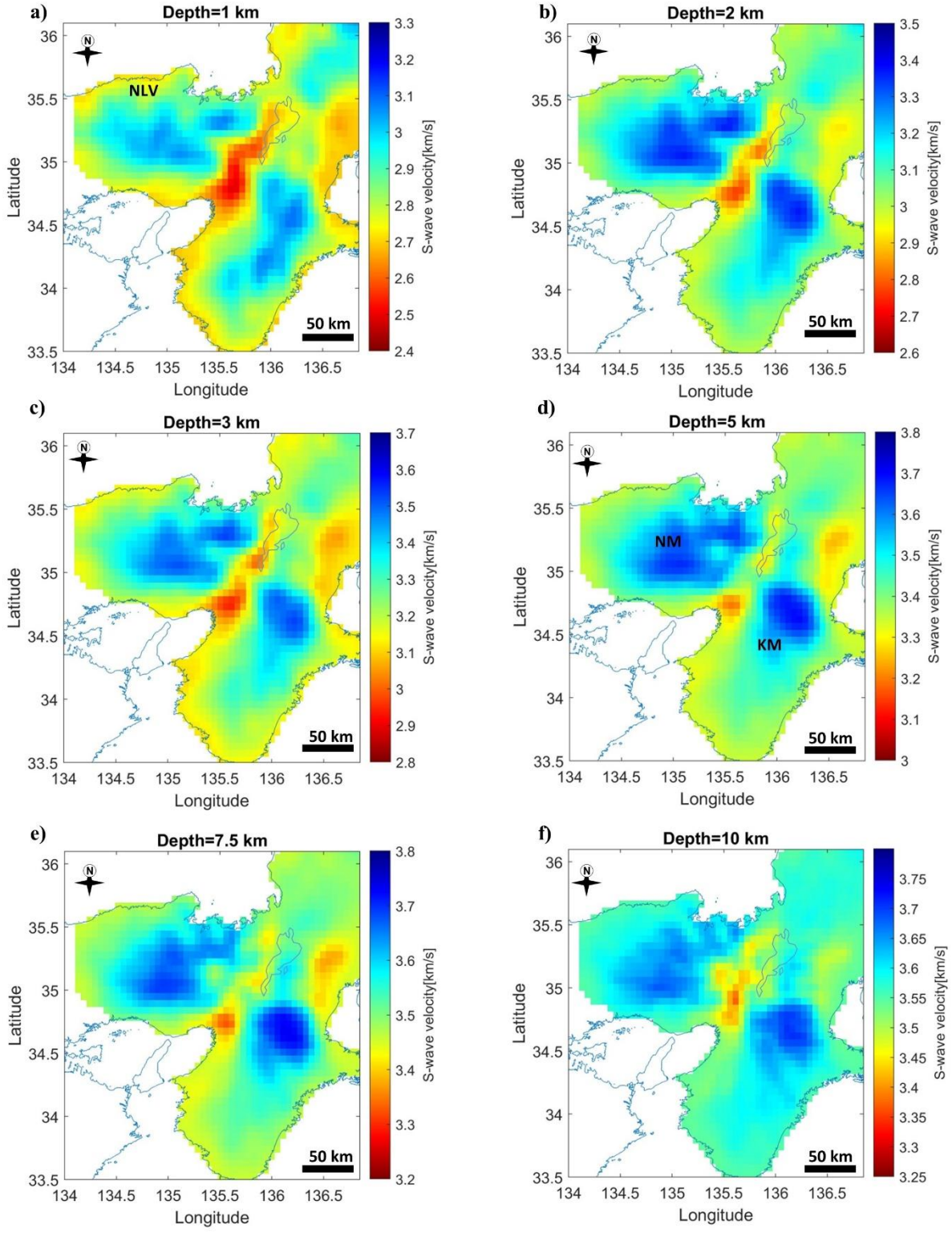

Fig. 9. Horizontal slices of the S-wave velocity model at discrete depth levels below sea level. Depth is shown above each respective panel. **a**–**f** S-wave velocity models without showing the active faults (S-wave velocity models before correcting for the effects of topography are shown in Fig. 14). NM and KM represent the prominent high-velocity anomalies.

Between the two distinct high-velocity zones exhibited in Nishida et al. (2008), an elongated low-velocity anomaly is evident. Likewise, a prominent low-velocity anomaly is observed in this study (Figs. 9-13), flanked on both sides by high-velocity zones (NM and KM) and trending roughly NE–SW. Although my results and those of Nishida et al. (2008) at a depth of about 2 km are similar, my S-wave velocity model shows prevalent small-scale (~13 km) low-velocity features at a depth of about 2 km and shallower. In the work of Nishida et al. (2008), the S-wave velocity model is constrained to a minimum depth of about 2 km and such narrow low-velocity zones could not be revealed clearly. The higher lateral resolution of my model at shallow depths ($\leq$ 2 km) than Nishida et al. (2008) model ascribes to the use of shorter wavelength surface waves and the dense seismic array, particularly in the most central part of the study area where temporary stations (red triangles in Figs. 1c and 5) are densely distributed. Most importantly, prominent anomalies identified in this study correlate well with known geologic features, including fault zones, sedimentary basins, and mountain ranges.

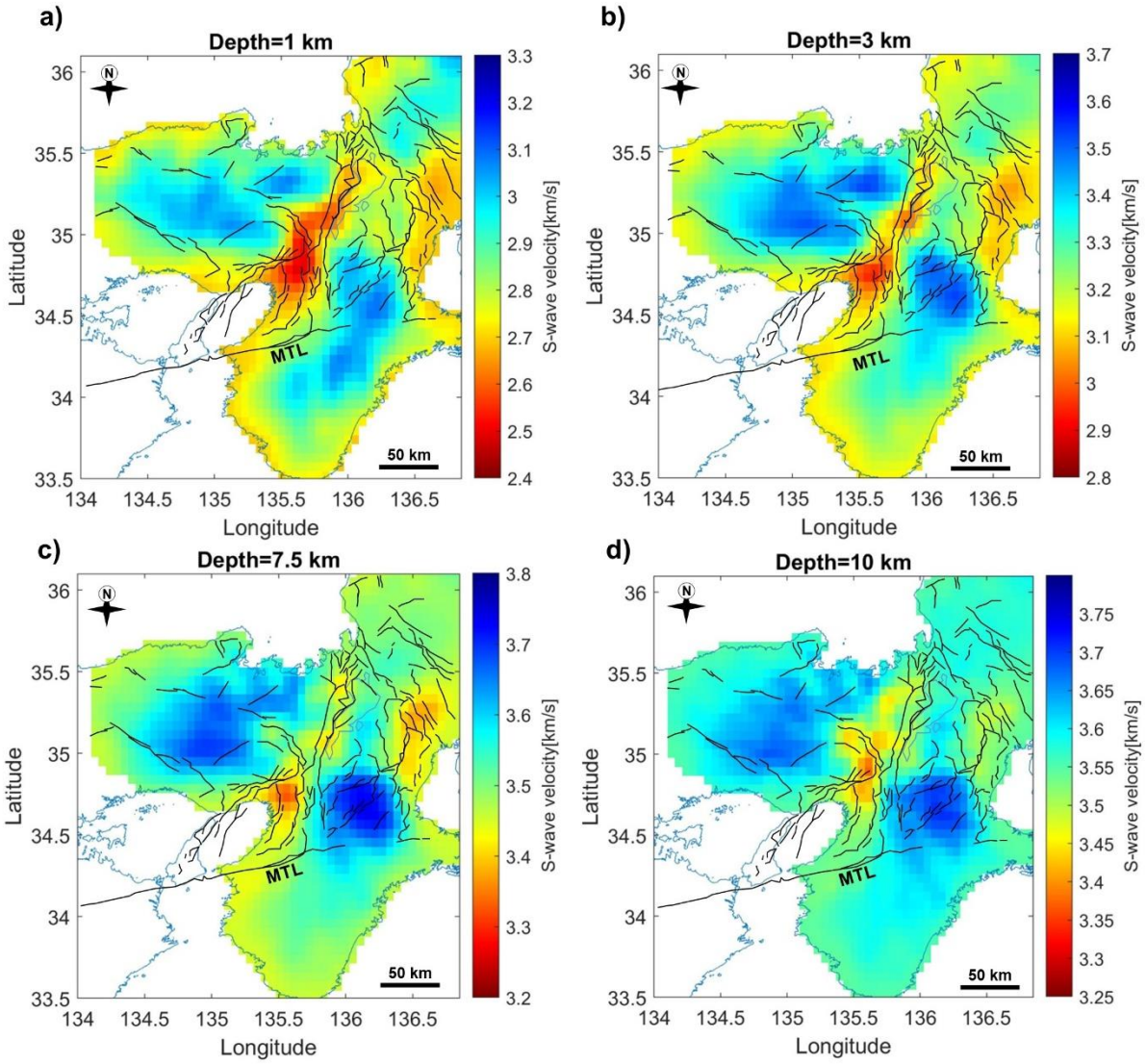

Fig. 10. Horizontal slices of the S-wave velocity model at discrete depth levels below sea level. a–d S-wave velocity models overlaid with active faults (black lines). Depth is shown above each respective panel. Also shown is the location of the Median Tectonic Line (MTL).

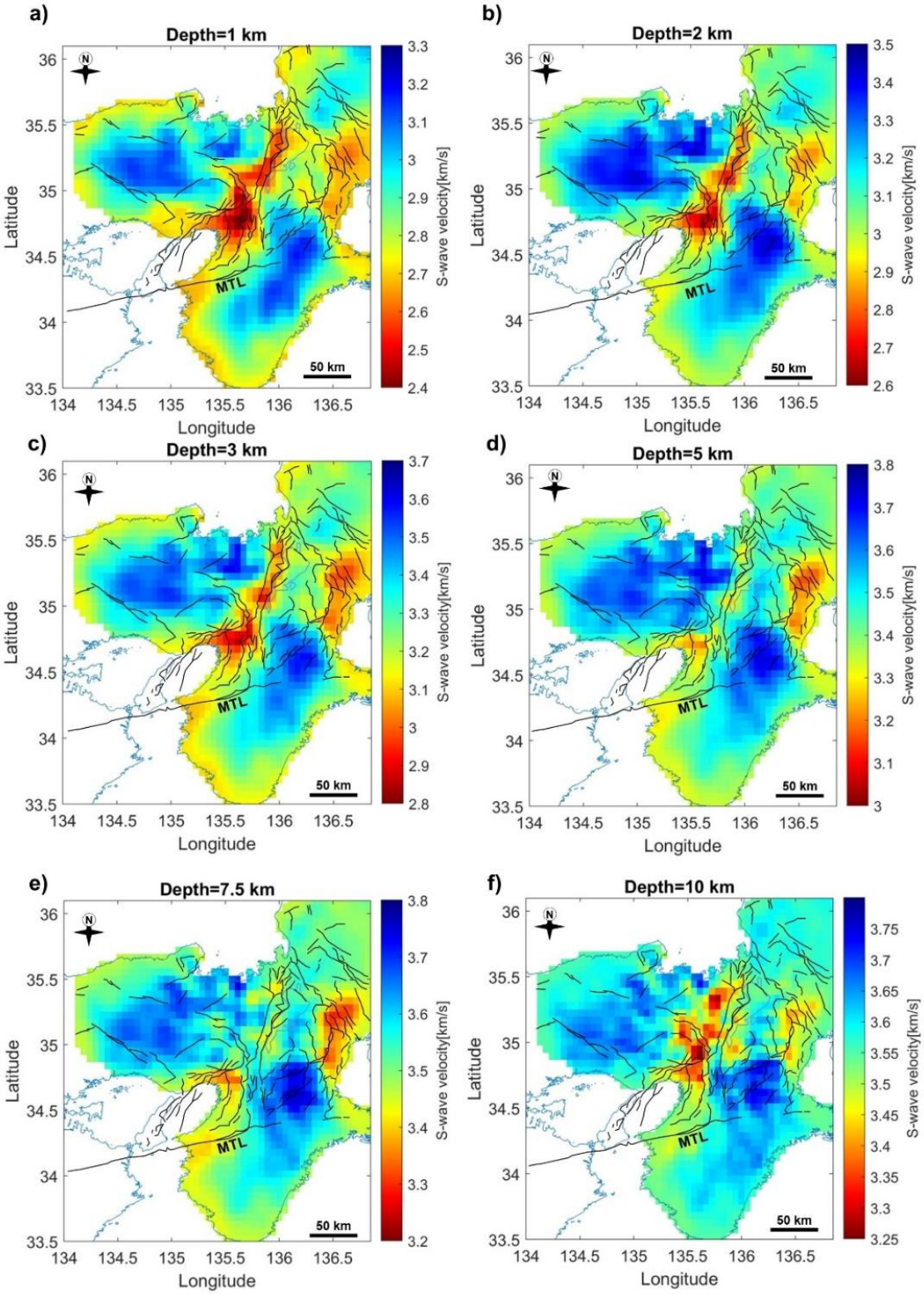

Fig. 11. Weakly smoothed S-wave velocity models with topography correction. This figure is relevant to Fig. 9, but the smoothing parameter in velocity inversion is weaker. (a–f) S-wave velocity models overlaid with active faults (black lines).

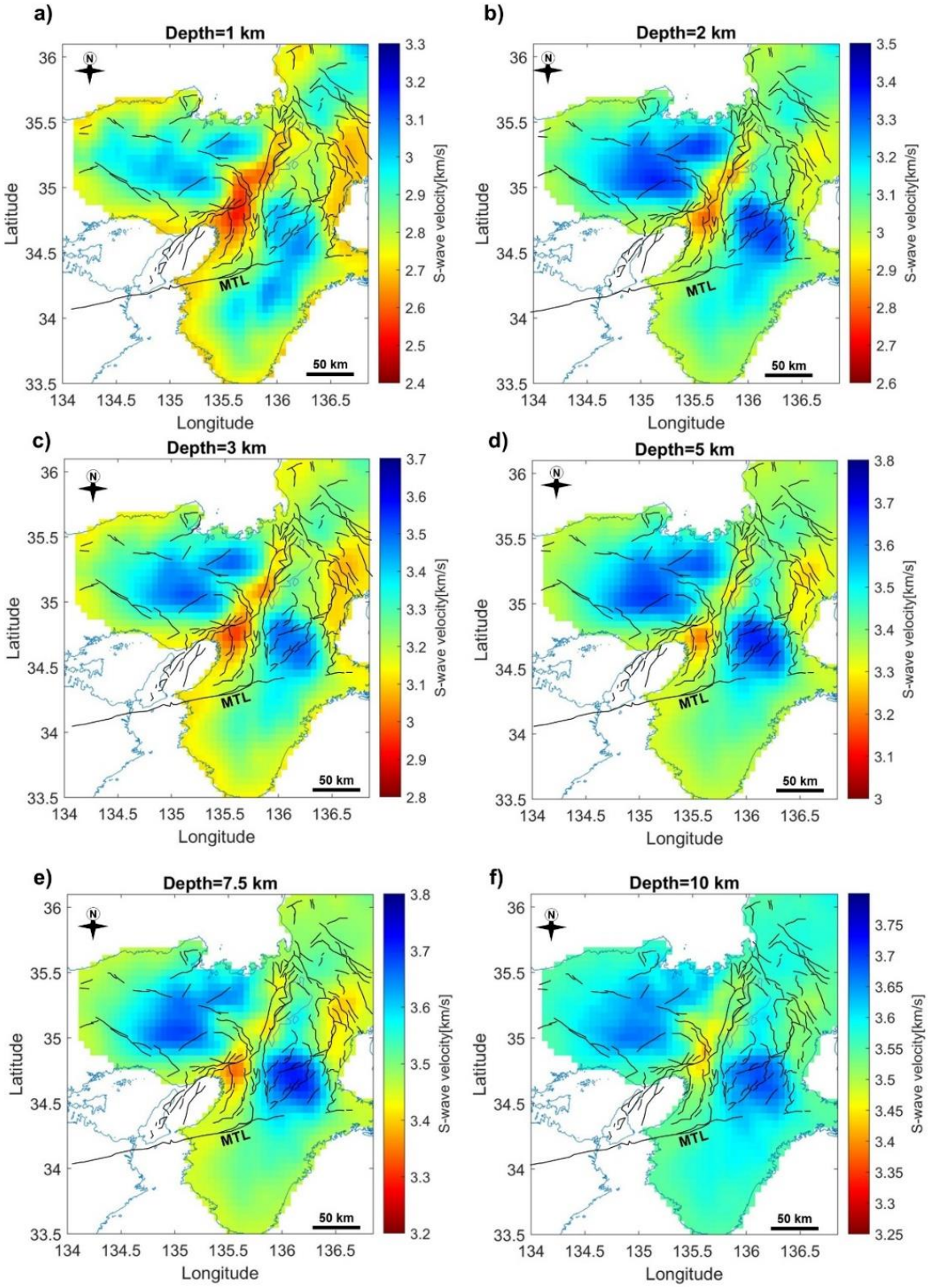

Fig. 12. Strongly smoothed S-wave velocity models with topography correction. This figure is relevant to Fig. 8, but the smoothing parameter in velocity inversion is stronger. (a–f) S-wave velocity models overlaid with active faults (black lines).

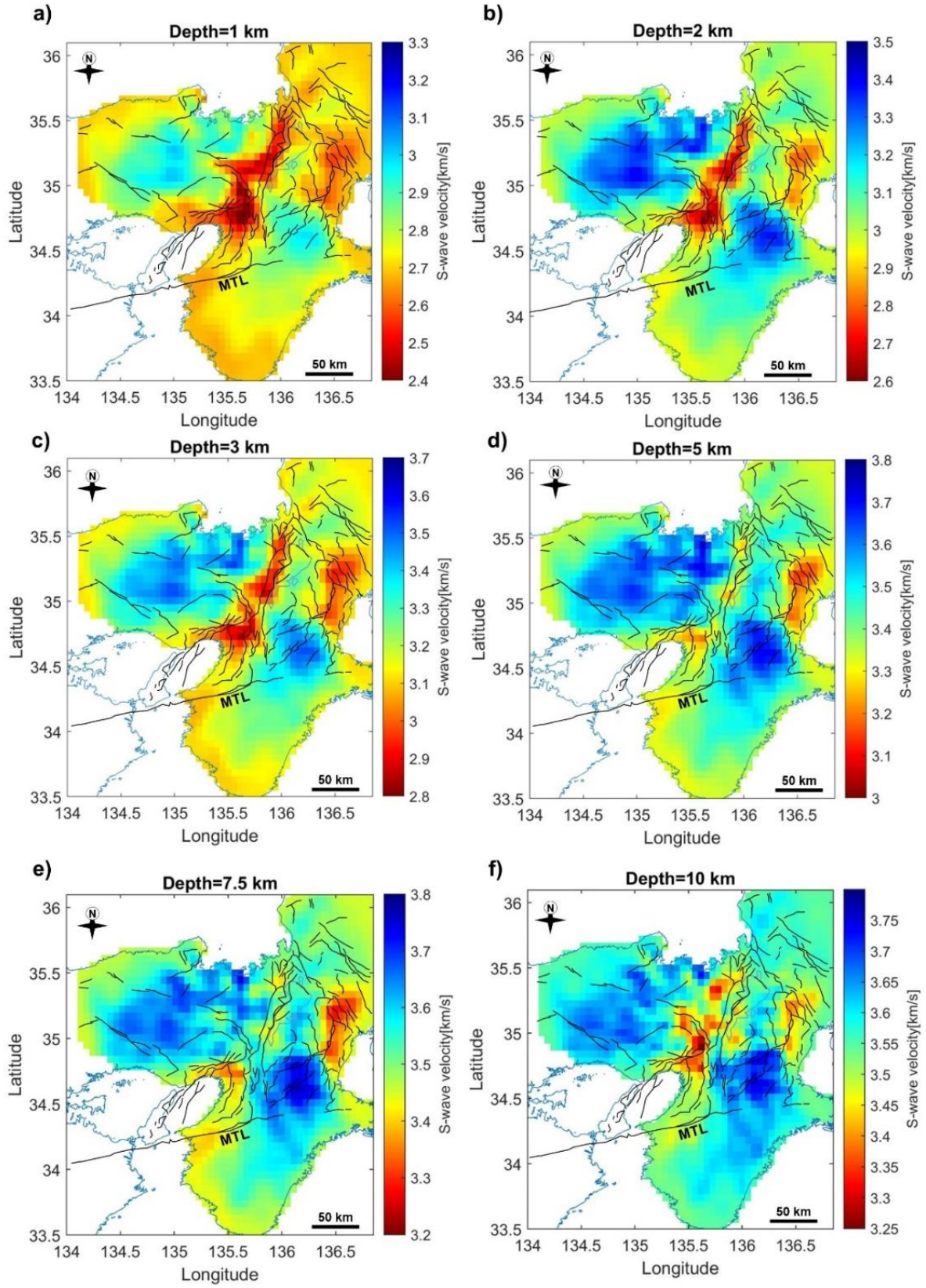

Fig. 13. Weakly smoothed S-wave velocity models without topographic correction. This figure is relevant to Fig. 11. (a–f) S-wave velocity models overlaid with active faults (black lines).

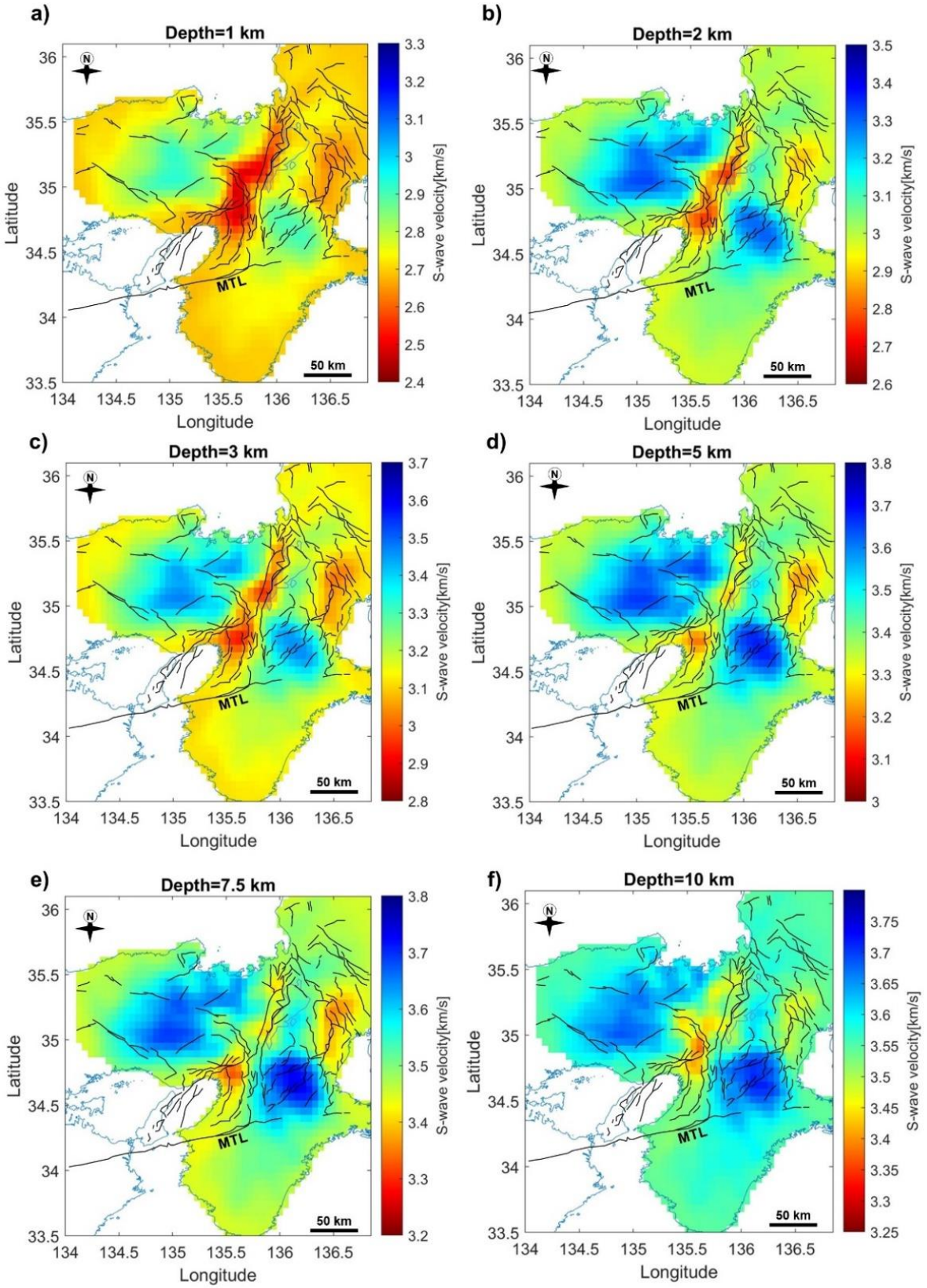

Fig. 14. Moderately smoothed S-wave velocity models without topographic correction. This figure is relevant to Fig. 9. (a–f) S-wave velocity models overlaid with active faults (black lines).

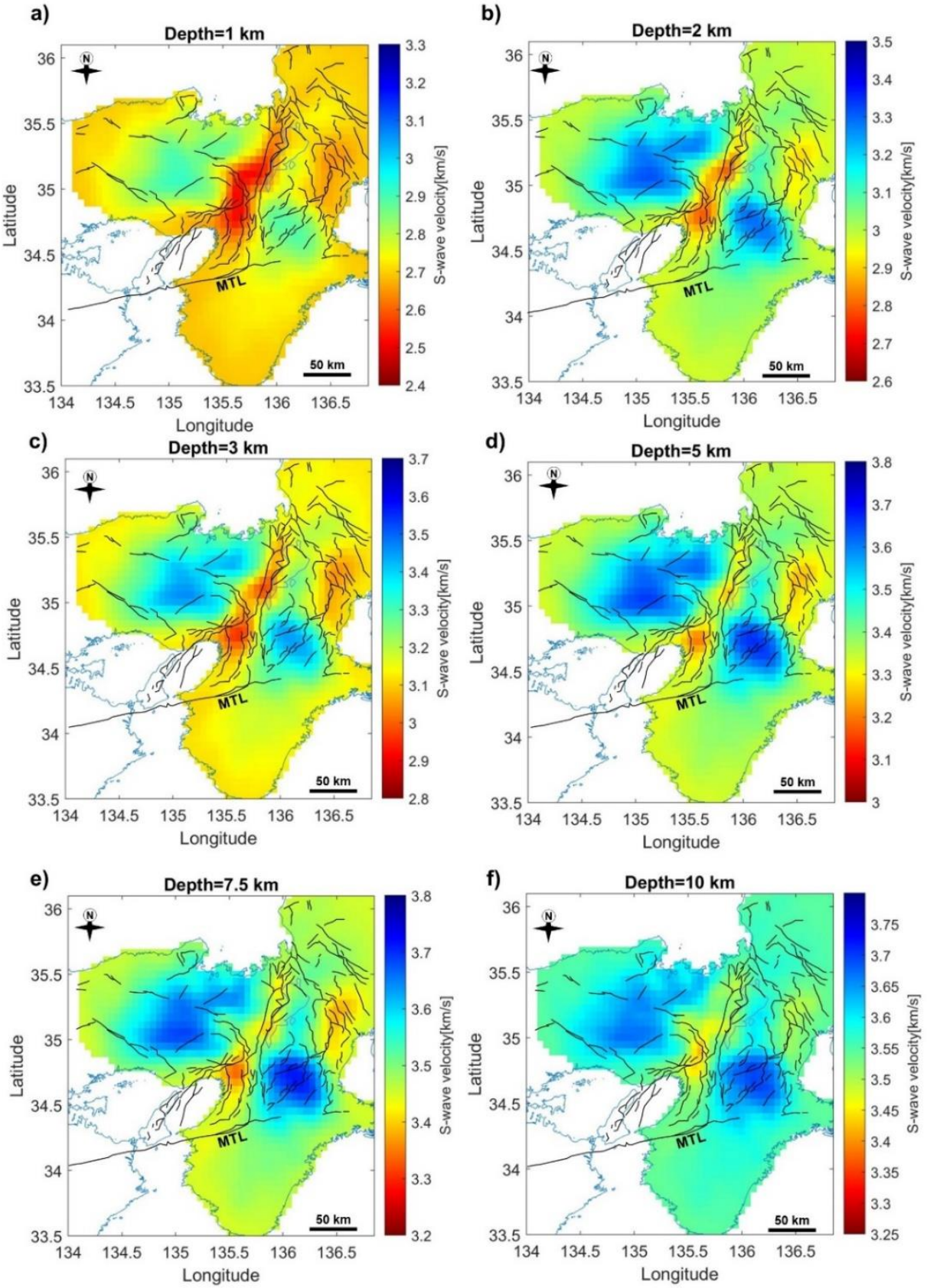

Fig. 15. Strongly smoothed S-wave velocity models without topographic correction. This figure is relevant to Fig. 12. (a–f) S-wave velocity models overlaid with active faults (black lines).

4.4 Spatial distribution of azimuthal anisotropy

The final azimuthal anisotropic models for the upper crustal structure of the Kinki region are illustrated in 3D horizontal slices (Figs. 16 and 17). Figure 16 represents the upper crustal structure of the entire Kinki region with a depth range of 2 to 11 km. Figure 17, showing the upper crustal structure with a depth range of 1 to 11 km, represents the inversion results for the central part of the Kinki region.

I overlay the isotropic velocity perturbations with fast polarization axes of seismic anisotropy. The results of this study (Figs. 16 and 17) reveal significant lateral variations and complex patterns of azimuthal anisotropy across the Kinki region. The patterns of the observed azimuthal anisotropy change around the boundary between the Inner Zone and Outer Zone (i.e., MTL).

In the Outer Zone, azimuthal anisotropy with predominantly NE-SW and E-W or ENE-WSW fast axes directions is observed. The E-W or ENE-WSW oriented fast axes can be observed in the western side of the Kii Mountainland (blue arrow in Fig. 16a), restricted within the low velocity zone and appear to be parallel to the MTL, whereas the NE-SW-oriented fast axes occur largely in the Kii Mountainland (red arrow in Fig. 16a) and are aligned in the same direction as the NE-SW trending part of the high velocity feature (elevated zone; Fig. 1b).

Figure 17 represents the isotropic S-wave velocity and azimuthal anisotropic model of the central part of the Kinki region (part of the Inner Zone). Here, three interesting anisotropy patterns are identified. On the northeastern part of the Kinki region (undemarcated zone in Fig. 17), NW-SE- and E-W-trending fast axes are dominant, with few vissible NE-SW directions.

Beneath the north central area (a zone demarcated by dashed, magenta closed curves in Fig. 17), there exist significant depth-dependent variation of the fast direction axes. Within the upper layers (less than 3 km), the fast polarization axes are predominantly aligned in the NW-SE or nearly E-W (Fig. 17a). The direction of the fast axes changes to largely NE-SW in layers

occurring from a depth range of 3 to 11 km, almost perpendicular to the NW-SE fast axes direction observed in the upper layers (less than 3 km). At 3 km depth (Fig. 17b), the NE-SW fast axes direction is consistent with the orientation of the high strain rate deformational zone, the NKTZ. I also note that from a depth of 3 km, these NE-SW-trending fast axes occur mainly within the eastern portion of the high velocity features, then gradually spreads to the east towards the NE-SW trending low velocity zone as the depth increases. Furthermore, the magnitude of anisotropy here is stronger than in other parts of the study area (exceeding 4 %).

The northeastern part of the study area (a zone demarcated by dashed, black closed curves in Fig. 17) forms part of the Kinki Triangle (Fig. 1c). It is characterized by significant lateral variations of the fast axes directions. Converging NW-SE and NE-SW fast axes directions and some curvilinear patterns are evident in this area. The magnitude of anisotropy here is much stronger between 3 and 9 km depth slices (Figs. 17b-f) in the high velocity zone (~ 4 %), where the fast polarization axes are predominantly aligned in the NW-SE direction (Fig. 17).

Around the high velocity zone denoted A1 in Fig. 16d, the azimuthal anisotropy pattern shows predominantly E-W and NW-SE fast axes directions in the center, and NE-SW fast axis directions at its western margin. The direction of the fast axes within the high velocity zone A1 is consistent from a depth of about 3 km to ~7 km. In layers occurring at a depth range of 9-11 km, the strength of anisotropy is relatively weaker compared to the upper layers, and the patterns within these layers (9-11 km) are different to the ones observed in the shallower layers.

The patterns of anisotropy within and around the high velocity zone denoted A2 in Fig. 16d significantly vary with depth. The pattern of anisotropy seems to be more complex in the shallow layer (Fig. 16a) than the observed ones in the underlying layers. Figures 16b-d (3-7 km depth slices) exhibit a concave up (NW-SE and NE-SW converging fast directions) anisotropy pattern. The strength of anisotropy is relatively stronger within the upper layers (2-

7 km; Figs. 16a-d). However, the strength of anisotropy seems to be slightly weaker within the deeper layers (9-11 km), and the fast axes are dominantly aligned in the E-W direction.

The high velocity zone occurring slightly to the north of the MTL (denoted B in Fig. 16d) is characterized by predominantly NW-SE trending fast axes, that are almost perpendicular or oblique to the documented active faults in this area. The magnitude of anisotropy appears to be stronger (~ 4 %) within the upper layers (2-7 km; Figs. 16a-d) and slightly weaker in the lower layers (9-11 km; Figs. 16e-f).

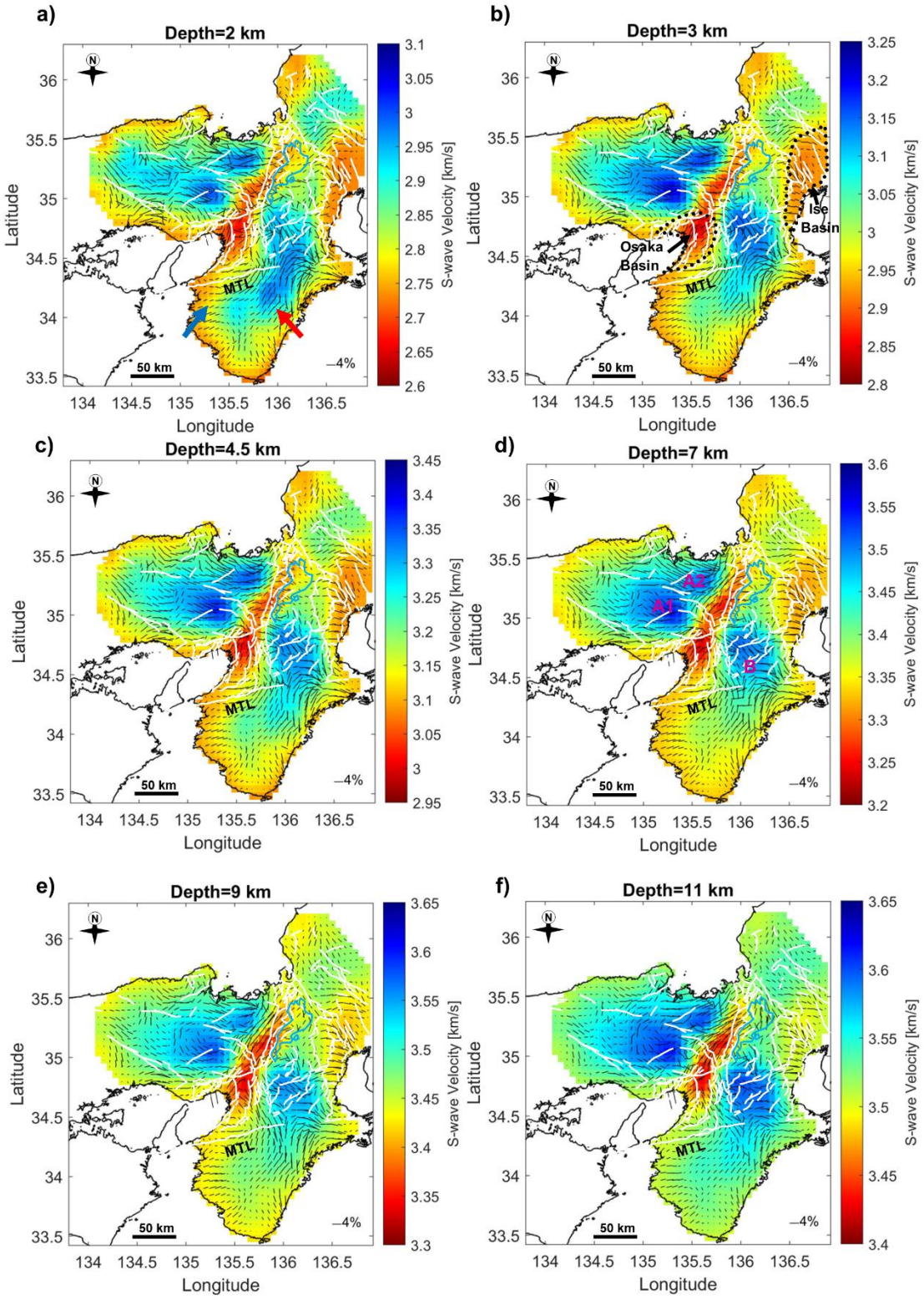

Fig. 16. (a-f) Horizontal slices showing the variation of isotropic S-wave velocities (background color) and azimuthal anisotropy (black bars) at discrete depth levels below sea level. White lines show the location of documented active faults. Depth (in km) is shown above each respective panel. Also shown

is the location of the Median Tectonic Line (MTL) and sedimentary basins (black, dashed closed curves in Fig. 16b).

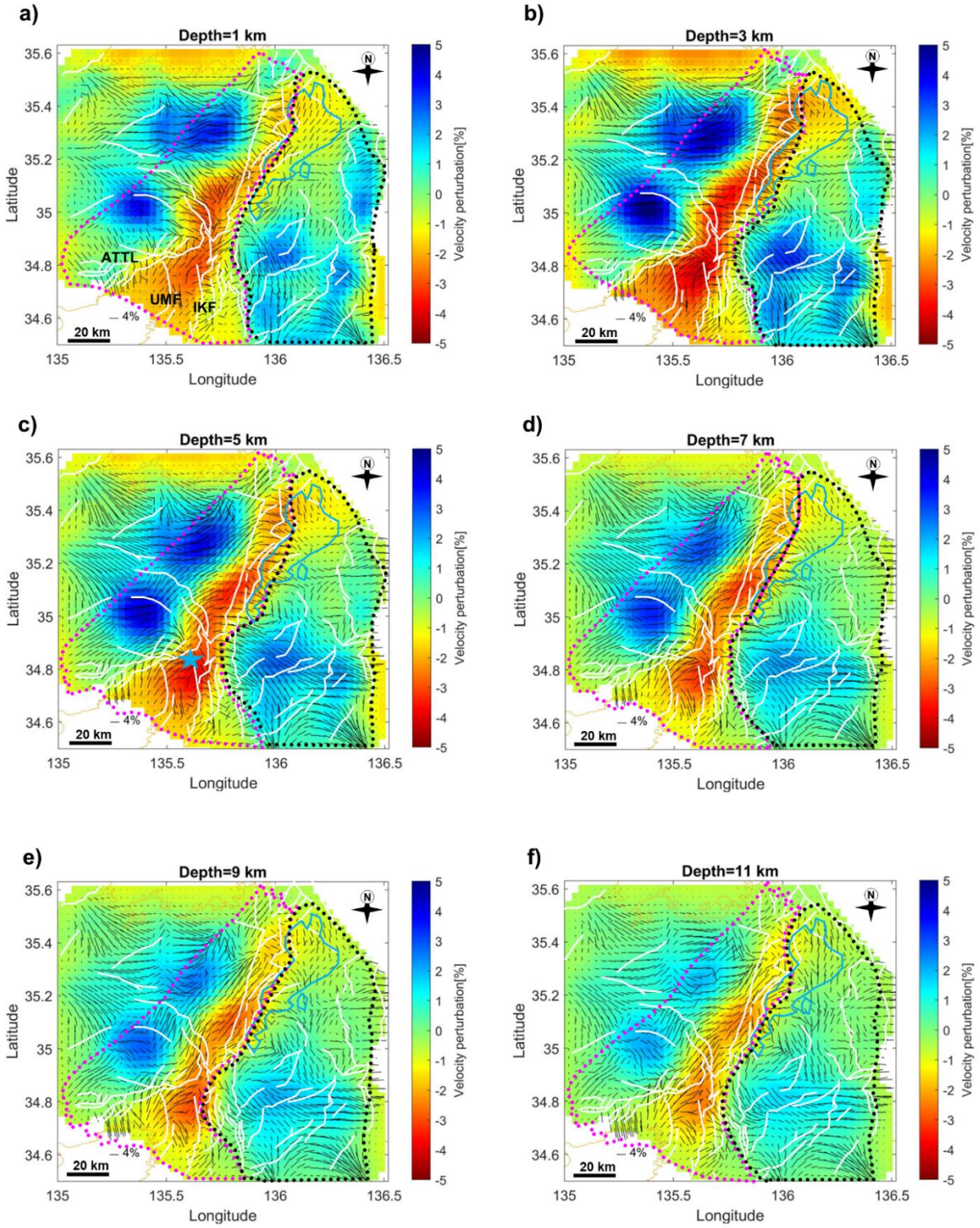

Fig. 17. (a) Horizontal slices showing the variation of isotropic S-wave velocities (background color) and azimuthal anisotropy (black bars) in the northern part of the Kinki region. Solid white lines indicate

the location of documented active faults. Blue star in (c) represents the location of the 2018 Osaka earthquake. Dashed magenta and black closed curves represent two zones with contrasting anisotropy patterns. Depth (in km) is shown above each respective panel.

5. Discussion

5.1 Crustal structure in the Kinki region

The high S-wave velocity features observed in the northwestern part of the Kinki region (marked NM in Figs. 9d and 18b) are attributable to the presence of the Yakuno intrusive rocks and the Mino/Tamba belts (Fig. 1a). The Yakuno intrusive rocks constitute the Maizuru zone, and the Mino/Tamba belts are Jurassic accretionary complexes composed of non-marine sediments, and the extensively distributed granite batholith (Matsushita, 1963; Nakae, 1993; Nakajima, 1994).

Moderate-low ray paths coverage towards the edges of the study area compromises the resolution of the S-wave velocity model obtained in this study. However, the extensive low-velocity anomaly labeled NLV in Fig. 9a is attributable to the Neogene volcanic and sedimentary series of the Tango-Tajima terrain (Matsushita, 1963). The high velocities on the southeastern side of the study area may be indicating the presence of the zonally arranged Paleozoic and fossiliferous Mesozoic of the Chichibu terrain, and the scanty fossils along with the undivided Mesozoic of the Hidaka terrain on the southern side of the MTL and the granitic rocks of the Ryoke terrain to the northern side of the MTL (Fig. 1a).

A prominent elongated NE–SW trending low-velocity anomaly occurring between the high-velocity anomalies denoted by NM and KM (Figs. 9f and 18b) is observed. This low-velocity feature is consistent with the location of the Niigata–Kobe Tectonic Zone (NKTZ, Fig. 1b) and the Biwako-seigan Fault Zone on the western shoreline of Lake Biwa (BSFZ; Figs. 18b and 20a). The BSFZ is constituted of the NNE–SSW-trending west-dipping faults separated by clear small gaps or steps (e.g., the Zeze, Hiei, Katata, Hira, Katsuno, Kamidera, Aibano, and Chinai faults; Fig. 20a), and is reported to have a reverse fault sense of east side subsidence (Takemura et al., 2013).

Both the western and eastern sides of the NKTZ are characterized by conspicuous fault systems, with some major faults running through geological units, such as the Yagi-Yabu faults (YGF-YBF) and the Mitoke Fault (MTF) (Mogi et al., 1991). The intervening spaces between fault pairs such as the YGF–YBF and MTF faults are often situated in the terrace and alluvial plain (Katsura, 1990). The results of this study show the presence of low-velocity anomaly between the YGF–YBF and the MTF (Fig. 20), probably representing sedimentary units within and around the Fukuchiyama basin (FB), but may also be indicating a possibility of the existence of active faults interconnecting these fault pairs. Besides the gaps between pairs of known active faults, several narrow, elongated low-velocity anomalies are identified, which, to some extent, coincide well with the locations of known active faults.

Distinct low-velocity anomalies occur at the Sanda basin (SB), FB, Osaka basin (OB), Nara basin (NB), Kyoto basin (KB), Oomi basin (OoB), and the Ise basin (IB) (Fig. 18). The OB manifest as a near-elliptical low-velocity zone, with the northern and southern edges of this zone appearing to be oriented ENE–WSW and NE–SW, respectively. The low-velocity values in this area are likely to be representing the Plio-Pleistocene Osaka Group sediments (Itihara et al., 1997). The ENE–WSW trending northern boundary of the OB coincides with the location of the Arima-Takatsuki Tectonic Line (ATTL; blue line in Fig. 18a), which is nearly parallel to the MTL (Mitchell et al., 2011). Based on this notion, the ATTL marks the boundary between high-velocity zones (mountainous regions, e.g., the Hokusetsu Mountains) and low-velocity zones (basins, e.g., the SB and OB in Fig. 18a).

According to Hallo et al. (2019), the OB is bounded by two near-parallel reverse faults on its eastern margin, the Uemachi Fault Zone (UFZ) and the Ikoma Fault Zone (IFZ). However, the effect of these fault zones is not clear in the results obtained in this study. Even so, this study reveals a low-velocity feature stretching to deeper parts of the displayed vertical sections (Fig. 18c) occurring between known locations of the UFZ and IFZ. This low-velocity

anomaly corresponds to a sub-basin of the OB between the elevated areas of Ikoma and Uemachi Upland (Fig. 18c), designated the Kawachi plain (Hatayama et al., 1995).

The high-velocity basement material exhibits undulating topographic pattern, with some synclinal parts representing depressional areas in which deep sedimentary basins occur and anticlinal parts corresponding to the basement upheavals or mountain ranges (Figs. 18c-f and 19c-d). Since surface wave inversion is significantly sensitive to the presence of sediments, the low-velocity anomalies observed at depressional areas are postulated to be representing the prevailing thick sediments (Miyamura et al., 1981; Nakayama, 1996; Takemura, 1985).

At the Ise basin (IB, Fig. 18e), the high-velocity material appears to have subsided significantly. This subsidence may be reflecting the effects of the Kuwana and the Yokkaichi reverse faults, which form part of the nearly N–S trending Yoro fault system (Research Group for Active Faults of Japan, 1991). Similar discontinuities within the high-velocity material are evident beneath the OB and KB low-velocity material (Fig. 18c-f), likely to be representing the effects of the NKTZ and/or BSFZ.

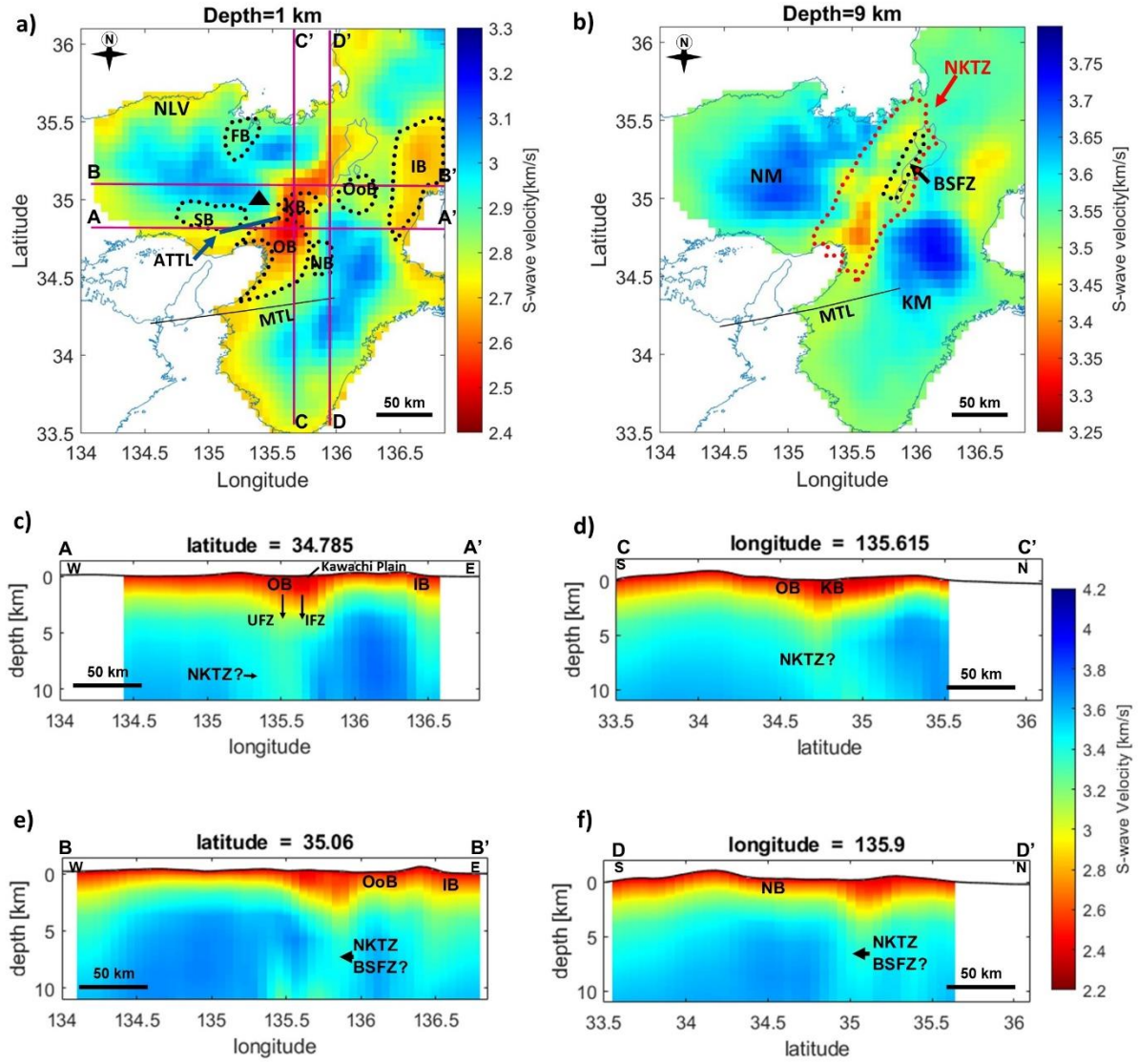

Fig. 18. S-wave velocity structure at 1 km **a** and 9 km **b** depths below sea level, and vertical slices **c**–**f** vertical S-wave velocity sections beneath the profiles marked in **a**, showing the variation of S-wave velocity with depth (bottom panels) and their respective elevation models in km (top panels). The solid black line represents the Median Tectonic Line (MTL), the dashed red closed-curve represents the Niigata-Kobe Tectonic Zone (NKTZ), and the thick solid blue line indicates the location of the Arima-Takatsuki Tectonic Line (ATTL). Black triangle represents the location of Hokusetsu mountains. Thin, dashed black closed curves show the locations of major sedimentary basins (SB, Sanda basin; FB, Fukuchiyama basin; OB, Osaka basin; NB, Nara basin; OoB, Oomi basin; KB, Kyoto basin; and IB, Ise basin). Also shown on the depth slices are the probable locations of the Kawachi plain, Nara basin

(NB), Uemachi Fault Zone (UFZ), Ikoma Fault Zone (IFZ), Biwako-seigan Fault Zone (BSFZ), NKTZ, Osaka basin (OB), and Ise basin (IB).

To assess the seismic activity correlating to the distribution of anomalous zones identified in this study, I superimposed earthquake hypocenters for the period 2001–2012 (Yano et al., 2017) on the S-wave velocity model (Figs. 19a and 20b). Numerous earthquake hypocenters are observed across the high-velocity zone on the western side of Hira Mountain (Mt. Hira in Fig. 20b). By contrast, aligned hypocenter clusters are evident within the NE-SW trending low-velocity zone consistent with the location of the NKTZ (Fig. 19a).

Besides these notable clusters, the northwestern part of the Kinki region has a wide distribution of hypocenters, some of which are aligned in the same trend as elongated low-velocity zones or along the low- and high-velocity zones interface (Figs. 19a and 20b). Some of the linear low-velocity zones that do not coincide with known active fault locations but exhibiting chains of earthquake hypocenters (Fig. 20b) may be representing the weathering effects and sediments associated with the activity of undocumented faults or fault zones.

The low-velocity zone along the western part of the Kii Mountainland (blue arrow in Figure 19a) show a dense distribution of earthquake hypocenters. These conspicuous seismic events are bounded to the north by the MTL and occur mainly within the Sambagawa and Chichibu metamorphic belts. The driving mechanisms of this seismic cluster have been discussed from different point of views in other studies (e.g., Kato et al., 2014; Maeda et al., 2021). In particular, Kato et al. (2014) attribute the observed low-velocity anomaly and a low Poisson’s ratio to the presence of fluid-filled cracks, with fluids such as water or partial melt being the key factors driving the increased seismicity. Whereas Maeda et al. (2021) posit that the dense seismic events are likely to be controlled by lithological properties of the crust, and

Kanamori and Tsumura (1971) associate the increased seismicity observed on this low-velocity zone with the regional structural heterogeneities due to the past activity of the MTL.

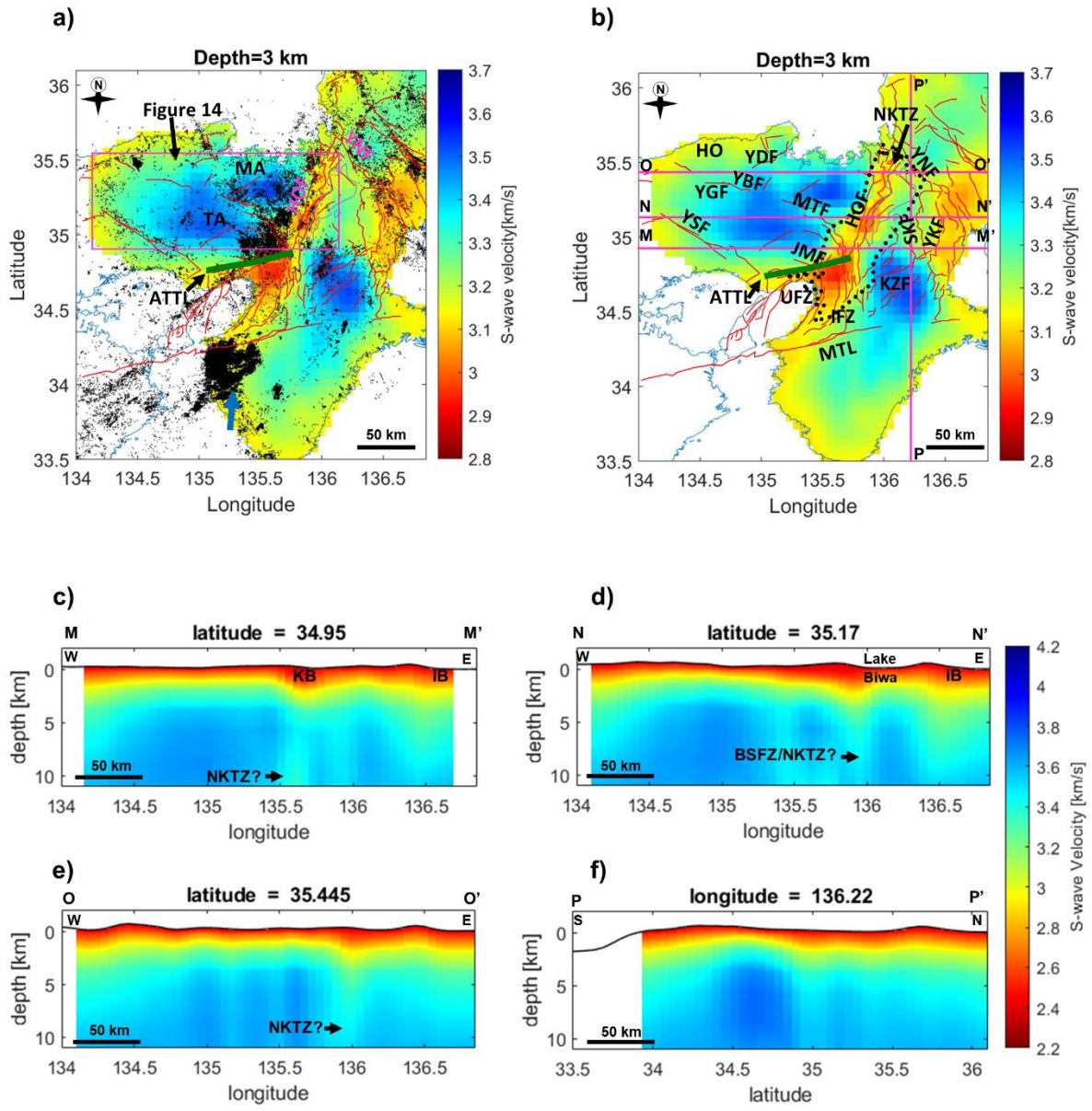

Fig. 19. a Map of seismic events that occurred during the January 2001 to December 2012 period (Yano et al., 2017) superimposed on the S-wave velocity model horizontal slice at 3 km depth below sea level. Plotted hypocenters (black dots) are for earthquakes ranging from 0 to 6.5 in moment magnitude for depths shallower than 12 km. Blue arrow indicates the location of dense distribution of earthquake hypocenters along the western part of the Kii Mountainland. **b** Distribution of active faults superimposed on the S-wave velocity model horizontal slice at 3 km depth below sea level. Solid red

lines represent active faults documented before this study (Research Group for Active Faults of Japan 1991). Thick dashed black closed-curve and a solid green line indicate the locations of the Niigata–Kobe Tectonic Zone (NKTZ) and the Arima–Takatsuki Tectonic Line (ATTL), respectively. Also shown are the locations of the Median Tectonic Line (MTL), Yamada Fault (YDF), Yamasaki Fault (YSF), Jumantsuji Fault (JMF, a member of the ATTL), Yabu Fault (YBF), Yagi Fault (YGF), Mitoke Fault (MTF), Hanaori Fault (HOF), Kizugawa Fault (KZF), Suzuka Fault (SKF), Yokkaichi Fault (YKF), Yanagase Fault (YNF), Uemachi Fault Zone (UFZ), Ikoma Fault Zone (IFZ), Tanba Block (TA), Hokutan Block (HO), and the Maizuru Block (MA). **c**–**f** Vertical sections showing the S-wave velocity variation beneath the profiles marked as solid magenta lines in Fig. 19b. Inferred locations of the Kyoto basin (KB), Ise basin (IB), Lake Biwa and the Biwako-seigan Fault Zone (BSFZ) and/or Niigata-Kobe Tectonic Line (NKTZ) along the profile are also shown on the vertical sections.

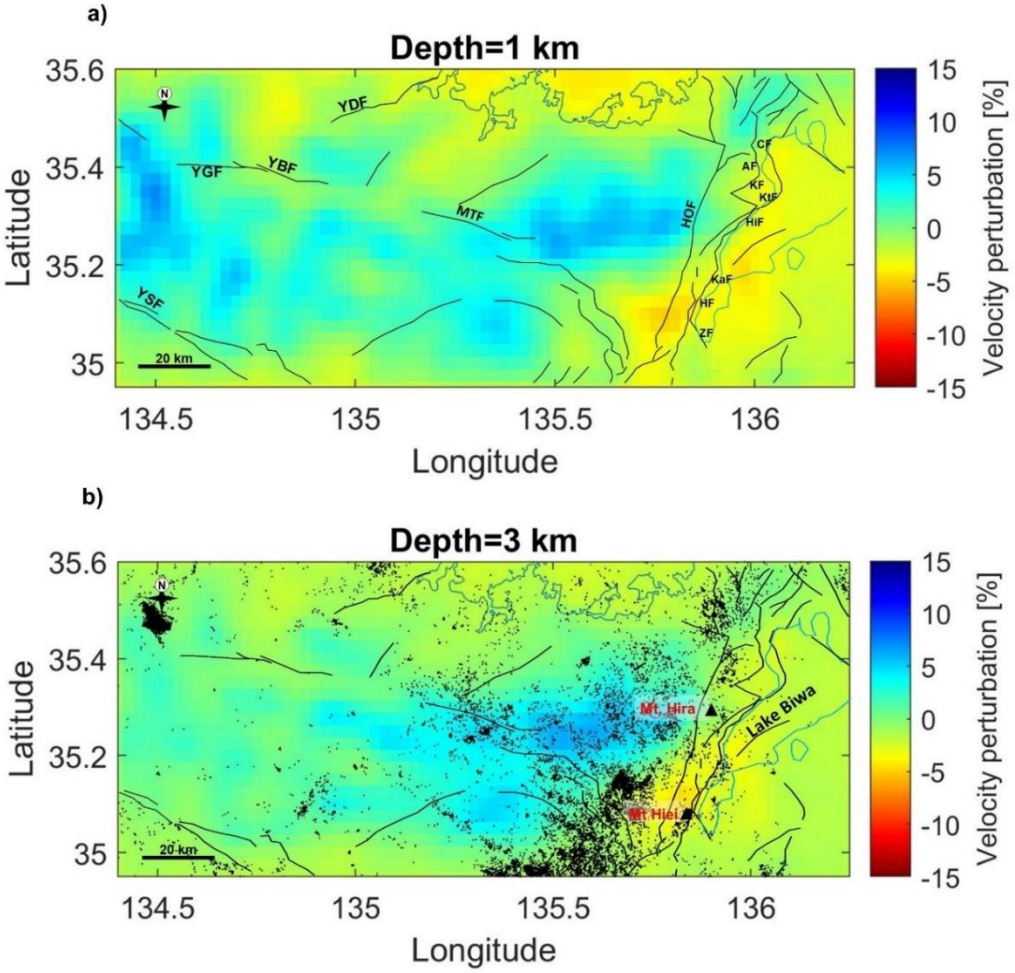

Fig. 20. a Enlarged view of the northern part of the Kinki region (shown in Fig. 19) showing the perturbation of S-wave velocity at a depth of 1 km below sea level. Also shown are the locations of the Yamada Fault (YDF), Yamasaki Fault (YSF), Yagi-Yabu Fault (YGF-YBF), Mitoke Fault (MTF), Hanaore Fault (HOF) and the Biwako-seigan Fault Zone members (Chinai Fault, CF; Aibano Fault, AF; Kamidera Fault, KF; Katsuno Fault, KtF; Hira Fault, HiF; Katata Fault, KaF; Hiei Fault, HF; Zeze Fault, ZF) (Kaneda et al., 2008). **b** perturbation of S-wave velocity at a depth of 3 km below sea level, overlaid with earthquake hypocenters (black dots; Yano et al., 2017) and active faults. Black triangles represent the Hira and Hiei mountains. Solid black lines show the location of documented active faults (Research Group for Active Faults of Japan, 1991).

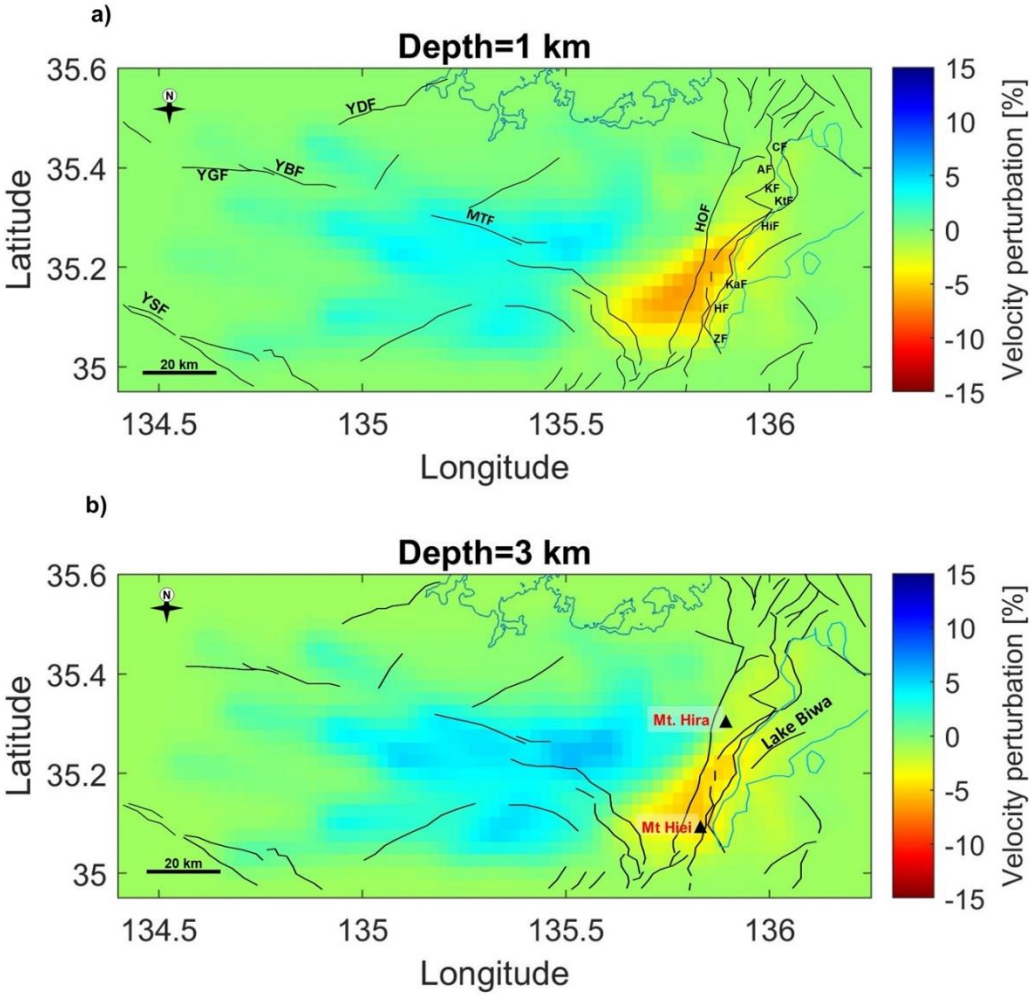

Fig. 21. S-wave velocity perturbation of the northern part of the Kinki region before topographic correction. (a) S-wave velocity perturbation at a depth of 1 km below sea level. Also shown are the locations of the Yamada Fault (YDF), Yamasaki Fault (YSF), Yagi-Yabu Fault (YGF-YBF), Mitoke Fault (MTF), Hanaore Fault (HOF) and the Biwako-seigan Fault Zone members (Chinai Fault, CF; Aibano Fault, AF; Kamidera Fault, KF; Katsuno, KtF; Hira Fault, HiF; Katata, KaF; Hiei Fault, HF; Zeze Fault, ZF). (b) S-wave velocity perturbation at a depth of 3 km below sea level. Solid black lines represent documented active faults.

5.2 Crustal deformation

In this section, I compare azimuthal anisotropy results with the shear-wave splitting measurements (Kaneshima, 1990; Hiramatsu et al., 1998; Iidaka et al., 2009; Hiramatsu et al.,

2010; Iidaka et al., 2016), the trajectories of the maximum horizontal compressional stress (Ukawa, 1982; Uchide et al., 2022) and the distribution of the principal strain rate axes estimated from the continuous GPS velocity field (Sagiya et al., 2000). Additionally, I superimposed earthquake hypocenters occurring at a depth range of 4 to 11 km for the period 2001–2012 (Yano et al., 2017) on the isotropic S-wave velocity and anisotropic model (Figs. 22a-b) in order to investigate the relationship between the seismic activity and the spatial distribution of anisotropy and isotropic velocity perturbations.

The results of this study show very complex spatial distribution of azimuthal anisotropy in the Kinki region. A sharp contrast in the fast axes direction and anisotropy patterns is observed between the northern (Inner Zone) and southern (Outer Zone) parts of the Kinki region. Potential sources of azimuthal anisotropy in each area are discussed below.

5.2.1 The southern part (Outer Zone) of the Kinki region

The Outer Zone exhibits coherent anisotropy with three prominent fast axes directions, the E-W, ENE-WSW, and the NE-SW. The NE-SW fast-direction axes seem to be island-parallel and are aligned along the Kii Mountainland. These fast-direction axes are persistent throughout the investigated depth range (2-11 km). This fast axes direction is consistent with both the trajectories of the maximum horizontal compressional stress (Uchide et al., 2022) and appear to be aligned in the same direction as the uplifted zone of the Kii Mountainland or normal to the ancient subduction direction (Fig. 1b; Tsuji et al., 2015). I posit that anisotropy observed in the central part of the Kii Mountainland may be largely induced by the stress field.

On the western side of the Kii Mountainland, prominent E-W and ENE-WSW fast axes directions are evident. These fast axes directions are spatially coincident with both the low velocity anomaly in the isotropic velocity model and the dense distribution of earthquake hypocenters (dark blue arrow in Fig. 22a). Moreover, the fast axis direction is inconsistent with

the NW-SE direction of the principal strain rate axes. However, the anisotropy orientation correlates well with both the compression stress trajectories (Ukawa, 1982) and the orientation of the MTL, suggesting that the observed anisotropy in this area could either be stress-induced or structure-induced. In the latter case, I postulate that the strike slip faulting of the MTL and its associated reactivation processes, or the mechanisms responsible for the seismic cluster prevailing here, may be having a strong influence on the observed azimuthal anisotropy in the western side of the Kii Mountainland, or may be influenced by the geological formations in this area.

5.2.2 The northern part (Inner Zone) of the Kinki region

The fast axes polarizations show significant lateral and vertical variations in the Inner Zone of the Kinki region, revealing different patterns of azimuthal anisotropy. These anisotropy patterns and the fast axes directions can be observed clearly in the enlarged view of the central part of the Kinki region (Fig. 17). In Fig. 17, I identified three zones with interesting anisotropy patterns: the northwestern area (undemarcated zone in Fig. 17), the north central area (a zone demarcated by dashed, magenta closed curves in Fig. 17b-f), and northeastern part (dashed, black closed curves in Fig. 17a-f).

5.2.2.1 Northwestern part of the Kinki region

On the northwestern part of the Kinki region (undemarcated zone in Fig. 17), the fast polarization axes are generally aligned in the NW-SE or near E-W directions, with small occurrences of the NE-SW-trending fast axes. These fast axes are consistent throughout the investigated depth range of 1 to 11 km, and significantly correlate with the axis of maximum horizontal compression stress (Ukawa, 1982), the axis of maximum horizontal compression strain rate (Sagiya et al., 2000), suggesting that the sources of anisotropy are mainly from both

the ambient stress field and strain rate. Also, a rotation of the fast axes direction from roughly WNW-ESE to NW-SE proximal to the Japan sea coast may be indicating the existence of different deformation patterns resulting from stress changes towards the coast. Several studies have demonstrated that anisotropy observed in the upper crustal structure is associated primarily with the structural fabric and stress-induced microcracks alignment, with the fast axes directions aligning with these microcracks (Crampin, 1978; Crampin and Peacock, 2008; Yang et al., 2018; Bem et al., 2022).

5.2.2.2 Central part of the Kinki region

On the central part of the Kinki region (a zone demarcated by dashed, magenta closed curves in Fig. 17), there is evident depth-dependent variation of the fast axes directions, changing from NW-SE and E-W (less than 3 km depth) to NE-SW (beneath 3 km depth). This change in the directions of the fast axes may be reflecting the existence of different deformational mechanisms in the upper crustal structure (less than 3 km depth) from the deeper parts (beneath 3 km depth). In this area, the axis of maximum horizontal compression stress and strain rate do not correlate well. The principal strain rate axes are oriented roughly WNW-ESE, while the axis of maximum horizontal compression stress are oriented roughly E-W. In the shallow part (less than 3 km depth), the observed anisotropy appears to be largely consistent with the principal strain rate axes (Sagiya et al., 2000). However, there are exceptions in some parts, for example, between latitudes 35.2-35.4 and longitudes 135.2-135.8 (high velocity zone in Fig. 17), where the near E-W oriented fast axes are significantly consistent with the directions of compressional stress trajectories (Ukawa, 1982) than with the strain rate. Despite the poor correlation between strain rate and stress in this area, it likely that the observed anisotropy in the shallower part (less than 3 km depth) may be stress-induced (Tsuji et al., 2011).

Beneath 3 km depth, the fast axes direction (NE-SW) is consistent with the direction of the horizontal displacement rate vectors (Sagiya et al., 2000) but inconsistent with the orientation of the maximum horizontal compressional stress and the principal strain rate axes. Additionally, this NE-SW fast axes direction coincides majorly with the NE-SW oriented Niigata-Kobe Tectonic Zone (NKTZ) and the NNE–SSW-trending west-dipping faults, designated the Biwako-seigan Fault Zone (BSFZ). Furthermore, in the central part of the Kinki region, many earthquake hypocenters are aligned in the NE-SW direction, fitting well with the NE-SW polarized fast axes (Fig. 22). Therefore, there could be anisotropy mechanism change between shallow softer formation (stress-induced) and deep harder formation (structure-induced anisotropy).

In the southeast end of this area (red arrow in Fig. 22b), that is, proximal to the location of the 2018 Osaka earthquake of Mw 5.6 (blue star in Fig. 22b) and at a zone where the ENE–WSW strike-slip Arima-Takatsuki Tectonic Line (ATTL) links up with the N-S trending Uemachi fault (UMF) and Ikoma fault (IKF; Figs. 17a and 22b), NE-SW- and NW-SE-trending fast axes are observed. Here, earthquake hypocenters are densely aligned in the same direction as both the NW-SE and NE-SW-trending fast axes. Moreover, there is a clear correlation of earthquake hypocenters with the NE-SW fast axes directions below a depth of 4 km (Figs. 23a-d), and the magnitude of anisotropy varies significantly in zones spatially correlating with or proximal to the location of earthquake hypocenters (Figs. 24a-d). Therefore, I posit that the observed azimuthal anisotropy beneath a depth of 3 km may be linked to the localized, high-strain-rate crustal deformation, extensive faulting and its associated fault fabrics, shearing in these fault zones or earthquake-related fractures/cracks that are fluid-filled and oriented in the same direction as the fast axes. Regarding the likely existence of fluid-filled cracks/fractures, my interpretation follows that of Hiramatsu et al. (1998), who suggested that the cause of the observed anisotropy in the central part of the Kinki region is related to the heterogeneous

structures created by fluid-filled cracks, and the interpretation of Nakajima and Matsuzawa (2017), who attributed the apparent low-velocity and high-attenuation anomaly in this area to the presence of aqueous fluids.

To probe further, I compare my azimuthal anisotropy results with the shear-wave splitting measurements conducted in and around the north central part of the study area by Hiramatsu et al. (2010) and Iidaka et al. (2016). For clarity, the north central part of my study area corresponds to areas 3 and 4 (Figs. 5 and 7) of Hiramatsu et al. (2010) and regions C and D (Fig. 3c) of Iidaka et al. (2016). The dataset used in Hiramatsu et al. (2010) had source depths restricted within 30 km, whereas Iidaka et al. (2016) used dataset consisting of earthquakes deeper than 230 km.

In Hiramatsu et al. (2010), the fast axes are oriented in the NW-SE direction in this area, correlating well with only the fast axes directions observed at shallow depths (less than 3 km) in my model, whereas, regions C and D of Iidaka et al. (2016) show NE-SW and ENE-WSW fast axes directions. The NE-SW direction of the fast axes observed below a depth of 3 km in this study is inconsistent with the model of Hiramatsu et al. (2010), but appears to be partially consistent with the model of Iidaka et al. (2016). Unlike the shear-wave splitting measurements of Hiramatsu et al. (2010) and Iidaka et al. (2016), the results of this study resolve the depth-dependent variation of anisotropy in this area. Anisotropy observed in the shallower layers (less than 3 km) is attributed to the stressing rate or strain rate, as suggested by Hiramatsu et al. (2010).

However, despite the consistency of the results of this study with those of Iidaka et al. (2016) for zones beneath 3 km, I posit that the cause of anisotropy within 3 to 11 km depth range is mainly caused by structural features prevailing beneath the central zone of the Kinki region. Even so, it must be noted that I do not dispute the suggestion of Iidaka et al. (2016) that the anisotropy observed in regions C and D could be caused by the alignment of olivine crystals

in the mantle wedge, with the crystal alignment inferred to be resulting from mantle flow related to subduction of the Pacific plate, considering the source depths of earthquakes used in their study.

5.2.2.3 Northeastern part of the Kinki region

Finally, I discuss the possible source of anisotropy observed in the northeastern part (a zone demarcated by dashed, black closed curves in Fig. 17), which forms part of the Kinki Triangle (Fig. 1c). This area has been dominated by the E-W compressional stress field, leading to the existence of predominantly N–S-oriented reverse active faults and some NE–SW or NW–SE strike-slip faults (Research Group for Active Faults of Japan, 1991). It is suggested that the E-W trending reverse faults occurred earlier than the N-S trending reverse faults in the Kinki region (Hallo et al., 2019), and some of the older E-W-trending faults have since switched from reverse to strike-slip regime due to the presently active movements in the Kinki Triangle (Huzita, 1969). The converging NW-SE and NE-SW fast axes directions and some curvilinear anisotropy patterns may be related to the geological structures such as faults and folds as opposed to the prevailing ambient stress field.

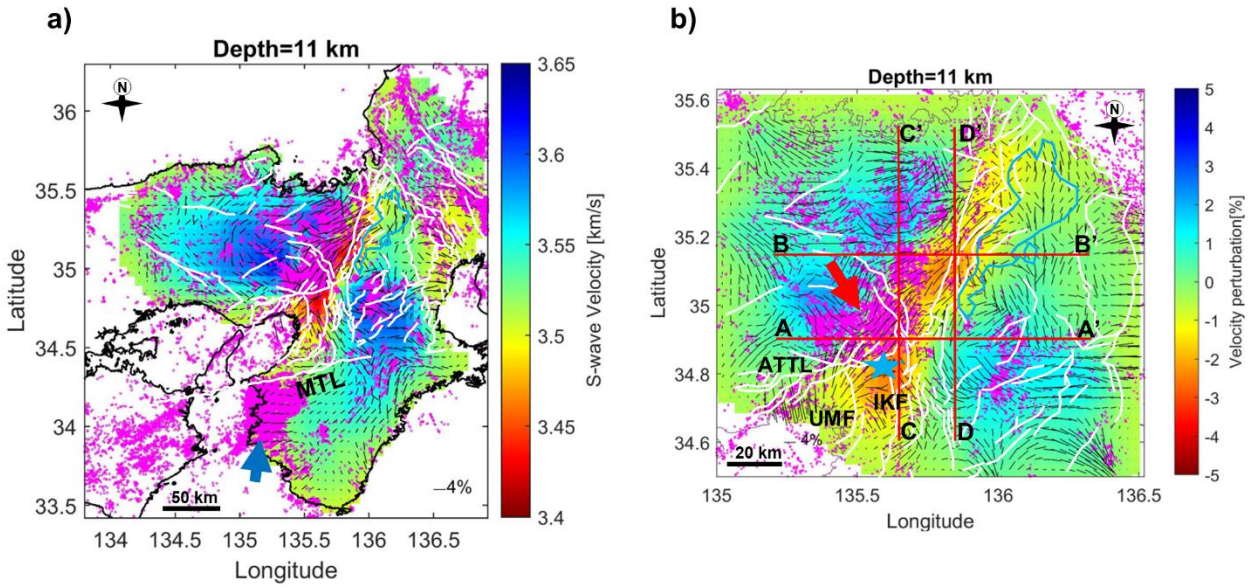

Fig. 22. Horizontal slices showing the variation of isotropic S-wave velocities (background color) and azimuthal anisotropy (black bars) at 11 km depth, overlaid with earthquake hypocenters (magenta dots; Yano et al., 2017) and active faults. Solid white lines show the location of documented active faults. Blue star in (b) indicates the location of the 2018 Osaka earthquake. Also shown are the locations of the Median Tectonic Line (MTL), Arima-Takatsuki Tectonic Line (ATTL), Uemachi Fault (UMF) and the Ikoma Fault (IKF).

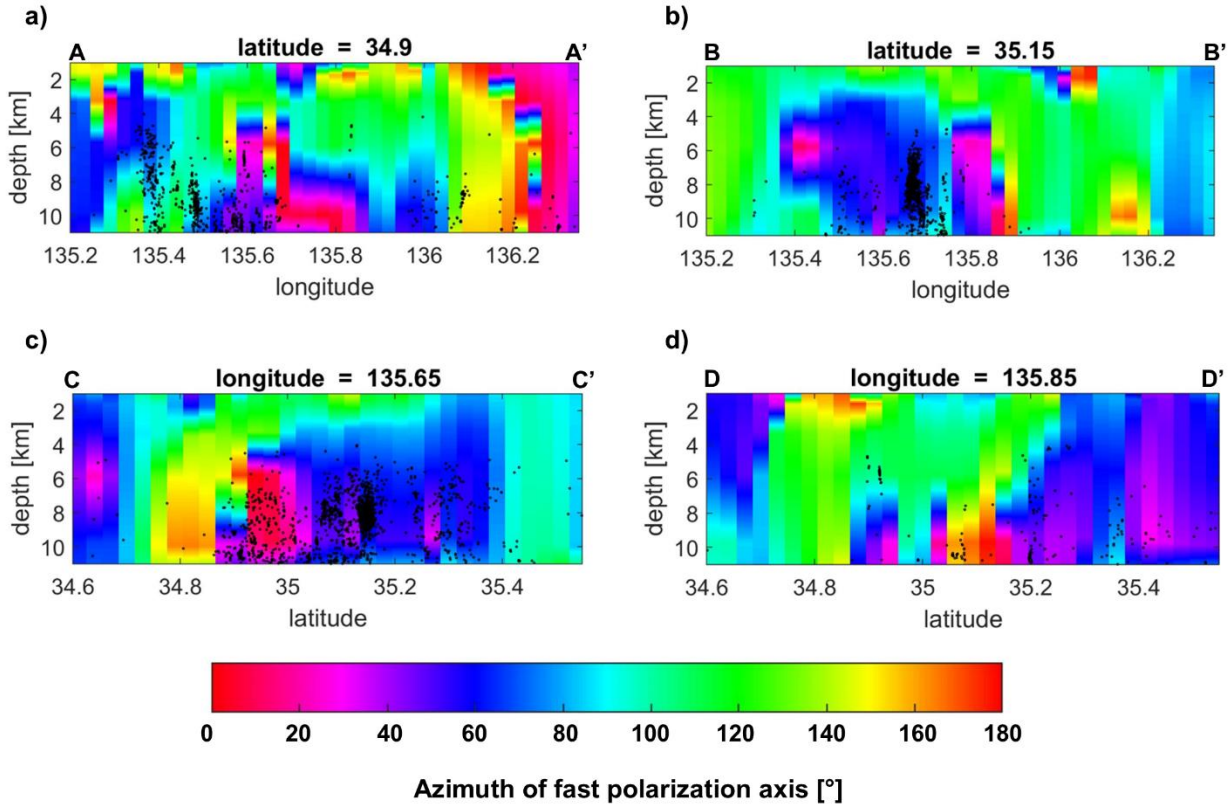

Fig. 23. (a–d) Vertical slices of the profiles marked as red lines in Fig. 15b, showing the variation of fast axes direction with depth. Black dots indicate earthquake hypocenters ranging from 0 to 6.5 in moment magnitude for depths ranging 4-12 km (Yano et al., 2017). Background color represents azimuth of fast polarization axis.

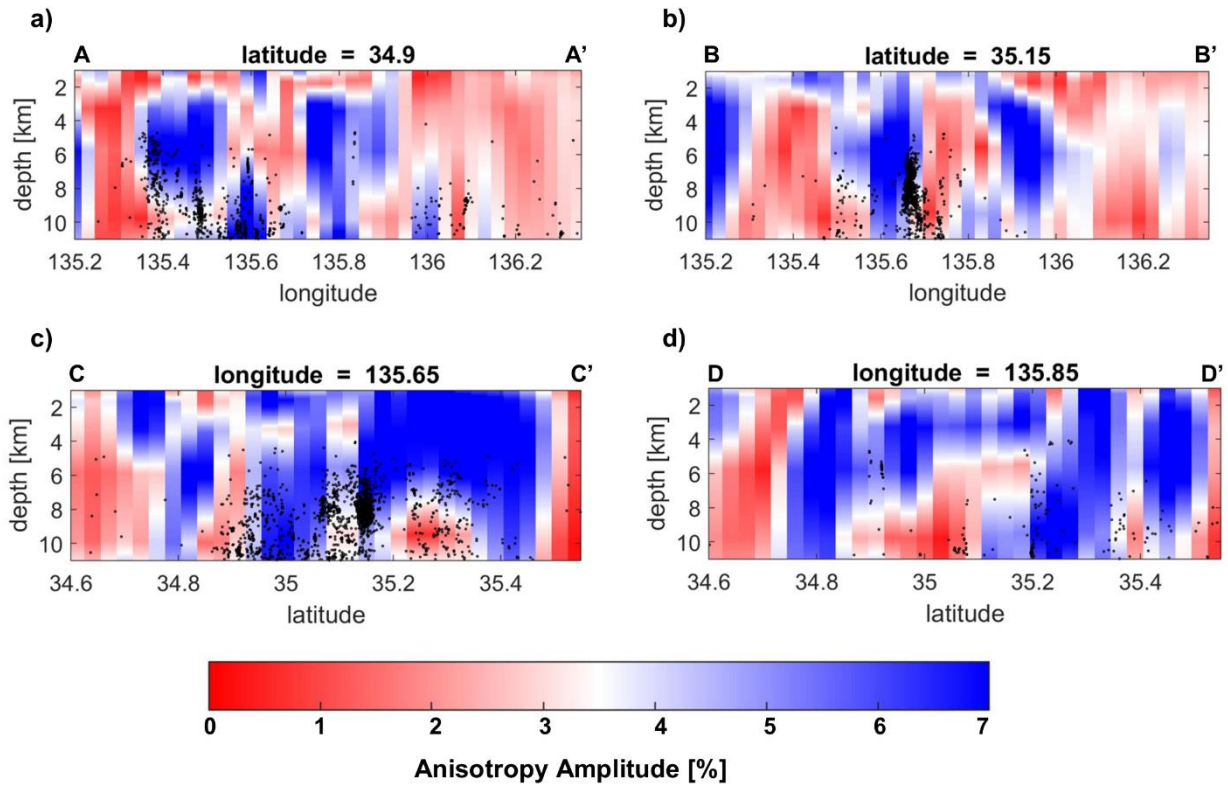

Fig. 24. (a–d) Vertical slices of the profiles marked as red lines in Fig. 15b, showing the variation of anisotropy amplitude both laterally and with depth. Black dots indicate earthquake hypocenters ranging from 0 to 6.5 in moment magnitude for depths ranging 4-12 km (Yano et al., 2017). Background color represents anisotropy amplitude.

6. Summary

I used data continuously recorded by a dense seismic array consisting of 221 permanent and temporary seismic stations to estimate a high-resolution shallow 3D S-wave velocity model of the Kinki region by ambient noise tomography approach. Additionally, I estimated the first depth-dependent high-spatial resolution 3D azimuthal anisotropic upper crustal structure of the Kinki region. Based on my results, the following conclusions were made:

- High-velocity zones identified in the northwestern and southeastern parts of the study area are likely to be representing the shallow basement material, mountainous regions, or sedimentary complexes. Sedimentary basins manifest as low-velocity zones.
- The high-resolution S-wave velocity model obtained in this study revealed fine-scale low-velocity tectonic structures, coexisting with known active faults, such as the N–S-, ENE–WSW-, and NE–SW-trending active faults on the eastern side of the Niigata–Kobe Tectonic Zone.
- Despite the limited resolution of my S-wave velocity model on the northwestern side of the Kinki area, elongated low-velocity features that are not consistent with known active faults were revealed, likely to be indicating a possible existence of unidentified faults on the northwestern side of the Kinki region (Fig. 20).
- The alternating pattern of subsided and uplifted zones observed in the vertical slices of the S-wave velocity model obtained in this study is consistent with the tectonic history of the Kinki triangle, which has been dominated by the E–W compressional movement and has numerous active faults of diverse orientations.
- The resolved linear low-velocity zones that are characterized by aligned distribution of earthquake hypocenters may be indicating the presence of hidden tectonic structures (e.g., fault zones), therefore, will be useful for hazard assessment and disaster mitigation.

- My anisotropy model reveals very detailed spatial variation of azimuthal anisotropy compared with the previous studies that estimated anisotropy in some parts of the Kinki region from shear-wave splitting measurements.
- Anisotropy patterns resolved in this study vary significantly across the Kinki region, suggesting a possibility of multistage crustal deformation and multiple sources of anisotropy in the Kinki region.
- The Outer Zone exhibits coherent NE-SW-trending fast axes in the center of the Kii Mountainland, which are likely to be reflecting stress-induced or fossil anisotropy.
- The E-W and ENE-WSW trending fast polarization axis observed in the western side of the Kii Mountainland are largely influenced by the horizontal compressional stress field. However, the activity of the Median Tectonic Line may also have a role in the anisotropy observed in this area.
- The NW-SE-trending fast axes observed on the northern side of the Median Tectonic Line and also in the northwestern part of the Inner Zone are consistent with the maximum horizontal compression strain rate, and are also in agreement with the shear-wave splitting results reported in previous studies. Therefore, the observed anisotropy in these areas is likely to be largely influenced by strain rate.
- In the central part of the Inner Zone (in and around the Niigata-Kobe Tectonic Zone), depth-dependent variation of anisotropy is evident, where the fast axes direction change from NW-SE and near E-W (shallower than 3 km) to NE-SW (beneath 3 km depth), suggesting a possible existence of different deformational mechanisms in this area. I posit that anisotropy observed shallower than 3 km in the central part of the Inner Zone may be stress induced, whereas, anisotropy observed below a depth of 3 km is likely to be caused by the localized, high-strain-rate crustal deformation, which may as well be associated with the dense distribution of earthquakes in this zone, shearing or fluid-

filled earthquake-related fractures/cracks oriented in the same direction as the fast axes direction.

- In the eastern part of the Inner Zone, the converging NW-SE and NE-SW fast axes directions and some curvilinear anisotropy patterns may be related to the prevalent NE–SW or NW–SE strike-slip faults and folds in the Kinki Triangle (structure-induced anisotropy).

These findings allude to the improved resolution of my S-wave velocity and azimuthal anisotropy models compared with those obtained in previous studies of the Kinki region, and therefore contribute significantly towards understanding the shallow crustal structure, state of stress and deformational mechanisms in the Kinki region.

7. Acknowledgements

I give thanks to the Lord, God of Mount Zion, for His mercies and protection, the wisdom and the strength to persevere.

Without the assistance of many people during my PhD at Kyushu University, this Thesis would not have been a success. Together, we made it possible and if I forget to mention your names, just know that your input in this work is greatly acknowledged.

First and foremost, I would like to thank Professor Takeshi Tsuji for giving me the opportunity to be a PhD student under his guidance before he transferred to the University of Tokyo and the many useful discussions, his patience to correct my errors in manuscripts writing and for providing all the support I needed during my study. I would also like to thank Professor Akira Imai for his supervision and guidance. To Professor Tatsunori Ikeda, your input towards the success of this thesis can never go unnoticed, your critical comments during my research. I learnt so many things from you and I had a very good experience working with you. I will forever be indebted to you.

I wish to acknowledge Dr. Hiro Nimiya for the scientific discussions we had and the suggestions you made for my manuscript. To Yudai Suemoto san, I would like to thank you profusely for your assistance when I first got introduced to the ambient noise tomography method and for assisting me with our scripts. Also, it would be remiss of me not to mention Kota Mukumoto, the discussions we had benefited me in so many ways. I am also grateful to my lab mates; you guys are all a joy to with.

I am grateful to my uncle Mr. Simon Joni who has always supported me in many ways, for his calls and for keeping me in his prayers. I appreciate the constant support from my lovely wife, Joyce, for all she has done and for being patient with me being this far away from them

during my PhD. She has been taking care of our daughter, Chendzimu, in my absence, with the assistance of her parents Mr. Isaac Chilisa and Mrs. Julia Chilisa. Thank you so much.

I would like to acknowledge the Japan International Cooperation Agency (JICA) for giving the opportunity to participate in one of their long-term training programs, the Human Resources Development in the Mining Sector (KIZUNA Program) and for their support and funding during my PhD. I would also like to thank the department of Earth Resources Engineering at Kyushu University for enrolling as one of their PhD candidates and for assisting me in many possible ways during study.

For both paper one and paper two, Seismic data were obtained from the National Research Institute for Earth Science and Disaster Resilience (NIED), the National Institute of Advanced Industrial Science and Technology, the Japan Meteorological Agency, the Disaster Prevention Research Institute of Kyoto University, University of Tokyo, Nagoya University, and Kyushu University. The computations in this work were partly performed using the computer facilities at the Research Institute for Information Technology, Kyushu University. This work was supported by Japan Society for the Promotion of Science (JSPS) KAKENHI (Grant Numbers JP19K23544, JP20K04133, JP20H01997 and JP21H05202).

References

Aki, K. (1957) Space and time spectra of stationary stochastic waves, with special reference to microtremors. Bull Earth Res Ins 35:415-456.

Adimah, N. I., & Padhy, S. (2020). Depth dependent azimuthal anisotropy in Madagascar island from ambient noise tomography. Tectonophysics, 789, 228513. https://doi.org/10.1016/j.tecto.2020.228513

Ando, M. (1979). The stress field of the Japanese Island in the last 0.5 million years. In Earth Mon. Symp. (Vol. 7, pp. 541-546).

Aoki, S., Iio, Y., Katao, H., Miura, T., Yoneda, I., & Sawada, M. (2016). Three-dimensional distribution of S wave reflectors in the northern Kinki district, southwestern Japan. Earth, Planets and Space, 68(1), 1-9. https://doi.org/10.1186/s40623-016-0468-3

Asano, K., Iwata, T., Sekiguchi, H., Somei, K., Miyakoshi, K., Aoi, S., & Kunugi, T. (2017). Surface wave group velocity in the Osaka sedimentary basin, Japan, estimated using ambient noise cross-correlation functions. Earth, Planets and Space, 69(1), 1-20. https://doi.org/10.1186/s40623-017-0694-3

Asten, M. W. (2006). On bias and noise in passive seismic data from finite circular array data processed using SPAC methods. Geophysics, 71(6), V153-V162. https://doi.org/10.1190/1.2345054

Balfour, N. J., Savage, M. K., & Townend, J. (2005). Stress and crustal anisotropy in Marlborough, New Zealand: evidence for low fault strength and structure-controlled anisotropy. Geophysical Journal International, 163(3), 1073-1086. https://doi.org/10.1111/j.1365-246X.2005.02783.x

Barnes, G. L. (2008). The making of the Japan Sea and the Japanese mountains: Understanding Japan's volcanism in structural context. Nichibunken Japan Review, 3-52.

Bem, T. S., Liu, C., Yao, H., Luo, S., Yang, Y., & Liu, B. (2022). Azimuthally Anisotropic Structure in the Crust and Uppermost Mantle in Central East China and Its Significance to Regional Deformation Around the Tan-Lu Fault Zone. Journal of Geophysical Research: Solid Earth, 127(3), e2021JB023532. https://doi.org/10.1029/2021JB023532

Bensen, G. D., Ritzwoller, M. H., Barmin, M. P., Levshin, A. L., Lin, F., Moschetti, M. P., ... & Yang, Y. (2007). Processing seismic ambient noise data to obtain reliable broad-band surface wave dispersion measurements. Geophysical journal international, 169(3), 1239-1260. https://doi.org/10.1111/j.1365-246X.2007.03374.x

Boness, N. L., & Zoback, M. D. (2006). Mapping stress and structurally controlled crustal shear velocity anisotropy in California. Geology, 34(10), 825-828. https://doi.org/10.1130/G22309.1

Boschi, L., & Ekström, G. (2002). New images of the Earth's upper mantle from measurements of surface wave phase velocity anomalies. Journal of Geophysical Research: Solid Earth, 107(B4), ESE-1. https://doi.org/10.1029/2000JB000059

Boschi, L., & Weemstra, C. (2015). Stationary phase integrals in the cross correlation of ambient noise. Reviews of Geophysics, 53(2), 411-451. https://doi.org/10.1002/2014RG000455

Brocher, T. M. (2005). Empirical relations between elastic wave speeds and density in the Earth's crust. Bulletin of the seismological Society of America, 95(6), 2081-2092. https://doi.org/10.1785/0120050077

Brown, M. (2010). Paired metamorphic belts revisited. Gondwana Research, 18(1), 46-59. https://doi.org/10.1016/j.gr.2009.11.004

Campillo, M., & Roux, P. (2015). Crust and lithospheric structure – Seismic imaging and monitoring with ambient noise correlations, in Treatise on Geophysics, 2nd edn, Vol. 1, pp. 391–417, eds Romanowicz, B., & Dziewonski, A., Elsevier, Amsterdam. https://doi.org/10.1016/B978-0-444-53802-4.00024-5

Chang, L. J., Ding, Z. F., & Wang, C. Y. (2015). Upper mantle anisotropy beneath the southern segment of North-South tectonic belt, China. Chinese Journal of Geophysics, 58(11), 4052-4067. https://doi.org/10.6038/cjg20151114

Chen, D., Zhang, F., Chen, H., Dilek, Y., Yang, S., Meng, Q., & Yang, C. (2015). Structural architecture and tectonic evolution of the Fangzheng sedimentary basin (NE China), and implications for the kinematics of the Tan-Lu fault zone. Journal of Asian Earth Sciences, 106, 34-48. https://doi.org/10.1016/j.jseaes.2015.02.028

Chen, K. X., Gung, Y., Kuo, B. Y., & Huang, T. Y. (2018). Crustal magmatism and deformation fabrics in northeast Japan revealed by ambient noise tomography. Journal of Geophysical Research: Solid Earth, 123(10), 8891-8906. https://doi.org/10.1029/2017JB015209

Cho, I., Senna, S., Wakai, A., Jin, K., & Fujiwara, H. (2021). Basic performance of a spatial autocorrelation method for determining phase velocities of Rayleigh waves from microtremors, with special reference to the zero-crossing method for quick surveys with mobile seismic arrays. Geophysical Journal International, 226(3), 1676-1694. https://doi.org/10.1093/gji/ggab149

Choi, P. Y., Nakae, S., & Kim, H. (2011). Fault tectonic analysis of Kii peninsula, Southwest Japan: Preliminary approach to Neogene paleostress sequence near the Nankai subduction zone. Island Arc, 20(4), 455-476. https://doi.org/10.1111/j.1440-1738.2011.00779.x

Crampin, S. (1977). A review of the effects of anisotropic layering on the propagation of seismic waves. Geophysical Journal International, 49(1), 9-27. https://doi.org/10.1111/j.1365-246X.1977.tb03698.x

Crampin, S. (1978). Seismic-wave propagation through a cracked solid: polarization as a possible dilatancy diagnostic. Geophysical Journal International, 53(3), 467-496. https://doi.org/10.1111/j.1365-246X.1978.tb03754.x

Crampin, S. (1998). Shear-wave splitting in a critical crust: the next step. Revue de l'Institut Français du Pétrole, 53(5), 749-763.

Crampin, S., & Chastin, S. (2003). A review of shear wave splitting in the crack-critical crust. Geophysical Journal International, 155(1), 221-240. https://doi.org/10.1046/j.1365-246X.2003.02037.x

Crampin, S., & Peacock, S. (2008). A review of the current understanding of seismic shear-wave splitting in the Earth's crust and common fallacies in interpretation. Wave Motion, 45(6), 675-722. https://doi.org/10.1016/j.wavemoti.2008.01.003

Dreiling, J., Tilmann, F., Yuan, X., Giese, J., Rindraharisaona, E. J., Rümpker, G., & Wysession, M. E. (2018). Crustal radial anisotropy and linkage to geodynamic processes: a study based on seismic ambient noise in southern Madagascar. Journal of Geophysical Research: Solid Earth, 123(6), 5130-5146. https://doi.org/10.1029/2017JB015273

Ekström, G., Abers, G. A., & Webb, S. C. (2009). Determination of surface-wave phase velocities across USArray from noise and Aki's spectral formulation. Geophysical Research Letters, 36(18), 5-9. https://doi.org/10.1029/2009GL039131

Ekström, G. (2014). Love and Rayleigh phase-velocity maps, 5–40 s, of the western and central USA from USArray data. Earth and Planetary Science Letters, 402, 42-49. https://doi.org/10.1016/j.epsl.2013.11.022

Fang, H., Yao, H., Zhang, H., Huang, Y. C., & van der Hilst, R. D. (2015). Direct inversion of surface wave dispersion for three-dimensional shallow crustal structure based on ray tracing: methodology and application. Geophysical Journal International, 201(3), 1251-1263. https://doi.org/10.1093/gji/ggv080

Feng, M., & An, M. (2010). Lithospheric structure of the Chinese mainland determined from joint inversion of regional and teleseismic Rayleigh-wave group velocities. Journal of Geophysical Research: Solid Earth, 115(B6), 1-16. https://doi.org/10.1029/2008JB005787

Foti, S., Lai, C. G., Rix, G. J., & Strobbia, C. (2014). Surface wave methods for near-surface site characterization. CRC press, Taylor & Francis Group LLC.

Gu, N., Wang, K., Gao, J., Ding, N., Yao, H., & Zhang, H. (2019). Shallow crustal structure of the Tanlu Fault Zone near Chao Lake in eastern China by direct surface wave tomography from local dense array ambient noise analysis. Pure and Applied Geophysics, 176(3), 1193-1206. https://doi.org/10.1007/s00024-018-2041-4

Guo, Z., & Chen, Y. J. (2017). Mountain building at northeastern boundary of Tibetan Plateau and craton reworking at Ordos block from joint inversion of ambient noise tomography and receiver functions. Earth and Planetary Science Letters, 463, 232-242. https://doi.org/10.1016/j.epsl.2017.01.026

Hallo, M., Opršal, I., Asano, K., & Gallovič, F. (2019). Seismotectonics of the 2018 northern Osaka M6. 1 earthquake and its aftershocks: joint movements on strike-slip and reverse

faults in inland Japan. Earth, Planets and Space, 71(1), 1-21. https://doi.org/10.1186/s40623-019-1016-8

Hasselmann, K. (1963). A statistical analysis of the generation of microseisms. Reviews of Geophysics, 1(2), 177-210. https://doi.org/10.1029/RG001i002p00177

Hatayama, K., Matsunami, K., Iwata, T., & Irikura, K. (1995). Basin-induced Love waves in the eastern part of the Osaka basin. Journal of Physics of the Earth, 43(2), 131-155. https://doi.org/10.4294/jpe1952.43.131

Hayashi, K. (2008). Development of surface-wave methods and its application to site investigations, (Doctoral dissertation). Retrieved from Kyoto University Research Information Repository. (https://doi.org/10.14989/doctor.k13774). Japan: Kyoto University.

Heki, K., & Miyazaki, S. I. (2001). Plate convergence and long-term crustal deformation in central Japan. Geophysical Research Letters, 28(12), 2313-2316. https://doi.org/10.1029/2000GL012537

Hirahara, K., Ando, M., Hoso, Y., Wada, Y., & Nakano, T. (1998). Search for the movement of an active fault by GPS measurements, Earth Monthly, 225, 149–153, (in Japanese).

Hirahara, K., Ikami, A., Ishida, M., & Mikumo, T. (1989). Three-dimensional P-wave velocity structure beneath central Japan: low-velocity bodies in the wedge portion of the upper mantle above high-velocity subducting plates. Tectonophysics, 163(1-2), 63-73. https://doi.org/10.1016/0040-1951(89)90118-2

Hiramatsu, Y., Ando, M., Tsukuda, T., & Ooida, T. (1998). Three-dimensional image of the anisotropic bodies beneath central Honshu, Japan. Geophysical Journal International, 135(3), 801-816. http://dx.doi.org/10.1046/j.1365-246X.1998.00663.x

Hiramatsu, Y., Iidaka, T. & The Research Group for the Joint Seismic Observations at the Nobi Area. (2015). Stress state in the upper crust around the source region of the 1891 Nobi earthquake through shear wave polarization anisotropy. Earth, Planets and Space, 67(1), 1-7. https://doi.org/10.1186/s40623-015-0220-4

Hiramatsu, Y., Iwatsuki, K., Ueyama, S., & Iidaka, T. (2010). Spatial variation in shear wave splitting of the upper crust in the zone of inland high strain rate, central Japan. Earth, planets and space, 62(9), 675-684. https://doi.org/10.5047/eps.2010.08.003

Huzita K (1962). Tectonic development of the Median Zone (Setouchi) of southwest Japan, since the Miocene, with special reference of the characteristic structure of Kinki area. Jour, Geosci, Osaka City Univ, 6(4), 103-144.

Huzita, K. (1969). Tectonic development of southwest Japan in the Quaternary period. J. Geosci. Osaka City Univ, 12, 53-70.

Huzita, K. (1980). Role of the Median Tectonic Line in the Quaternary tectonics of the Japanese Islands. Mem. Geol. Soc. Jpn., 18, 129-153. Huzita, K., Kishimoto, Y., & Shiono, K. (1973). Neotectonics and seismicity in the Kinki area, Southwest Japan. Journal of geosciences Osaka City University, (16), 93-124.

Hyodo, M., & Hirahara, K. (2003). A viscoelastic model of interseismic strain concentration in Niigata-Kobe Tectonic Zone of central Japan. Earth, planets and space, 55(11), 667-675. https://doi.org/10.1186/BF03352473

Iidaka, T., Hiramatsu, Y. & The Japanese University Group of the Joint Seismic Observations at NKTZ (2009). Shear-wave splitting analysis of the upper mantle at the Niigata-Kobe Tectonic Zone with the data of the Joint Seismic Observations at NKTZ. Earth, planets and space, 61(2), 227-235. https://doi.org/10.1186/BF03352903

Iidaka, T., Hiramatsu, Y. & The Research Group for the Joint Seismic Observations at the Nobi Area (2016). Heterogeneous mantle anisotropy and fluid upwelling: implication for generation of the 1891 Nobi earthquake. Earth, Planets and Space, 68(1), 1-9. https://doi.org/10.1186/s40623-016-0540-z

Iio, Y. (1996). A possible generating process of the 1995 southern Hyogo Prefecture earthquake: Stick of fault and slip on detachment. Jishin, 49(1), 103-112. https://doi.org/10.4294/zisin1948.49.1_103

Iio, Y., Kishimoto, S., Nakao, S., Miura, T., Yoneda, I., Sawada, M., & Katao, H. (2018). Extremely weak fault planes: an estimate of focal mechanisms from stationary seismic activity in the San'in district, Japan. Tectonophysics, 723, 136-148. https://doi.org/10.1016/j.tecto.2017.12.007

Itihara, M., Yoshikawa, S., & Kamei, T. (1997). 24 The Pliocene-Pleistocene boundary in Japan: the Osaka Group. The Pleistocene boundary and the beginning of the Quaternary, 41, 239. https://doi:10.1017/CBO9780511585760.026

Ito, K., Umeda, Y., Sato, H., Hirose, I., Hirata, N., Kawanaka, T., & Ikawa, T. (2006). Deep seismic surveys in the Kinki district: Shingu-Maizuru line. Bull. Earthquake Res. Inst. Univ. Tokyo, 81, 239-245.

Kanamori, H. (1995). The Kobe (Hyogo-ken Nanbu), Japan, earthquake of January 16, 1995. Seismological Research Letters, 66(2), 6-10. https://doi.org/10.1785/gssrl.66.2.6

Kanamori, H., & Tsumura, K. (1971). Spatial distribution of earthquakes in the Kii peninsula, Japan, south of the Median Tectonic Line. Tectonophysics, 12(4), 327-342. https://doi.org/10.1016/0040-1951(71)90020-5

Kaneda, H., Kinoshita, H., & Komatsubara, T. (2008). An 18,000-year record of recurrent folding inferred from sediment slices and cores across a blind segment of the Biwako-seigan fault zone, central Japan. Journal of Geophysical Research: Solid Earth, 113(B5). https://doi.org/10.1029/2007JB005300

Kaneshima, S. (1990). Origin of crustal anisotropy: Shear wave splitting studies in Japan. Journal of Geophysical Research: Solid Earth, 95(B7), 11121-11133. https://doi.org/10.1029/JB095iB07p11121

Kaneshima, S., Ando, M., & Crampin, S. (1987). Shear-wave splitting above small earthquakes in the Kinki district of Japan. Physics of the earth and planetary interiors, 45(1), 45-58. https://doi.org/10.1016/0031-9201(87)90196-8

Kästle, E. D., El-Sharkawy, A., Boschi, L., Meier, T., Rosenberg, C., Bellahsen, N., Cristiano, L., & Weidle, C. (2018). Surface wave tomography of the Alps using ambient-noise and earthquake phase velocity measurements. Journal of Geophysical Research: Solid Earth, 123(2), 1770-1792. https://doi.org/10.1002/2017JB014698

Katao, H., Maeda, N., Hiramatsu, Y., Iio, Y., & Nakao, S. (1997). Detailed mapping of focal mechanisms in/around the 1995 Hyogo-ken Nanbu earthquake rupture zone. Journal of Physics of the Earth, 45(2), 105-119. https://doi.org/10.4294/jpe1952.45.105

Kato, A., Kurashimo, E., Igarashi, T., Sakai, S., Iidaka, T., Shinohara, M., Kanazawa, T., Yamada, T., Hirata, N., & Iwasaki, T. (2009). Reactivation of ancient rift systems triggers devastating intraplate earthquakes. Geophysical Research Letters, 36(5). https://doi.org/10.1029/2008GL036450

Kato, A., Saiga, A., Takeda, T., Iwasaki, T., & Matsuzawa, T. (2014). Non-volcanic seismic swarm and fluid transportation driven by subduction of the Philippine Sea slab beneath

the Kii Peninsula, Japan. Earth, Planets and Space, 66(1), 1-8. https://doi.org/10.1186/1880-5981-66-86

Kato, A., Sakai, S. I., Matsumoto, S., & Iio, Y. (2021). Conjugate faulting and structural complexity on the young fault system associated with the 2000 Tottori earthquake. Communications Earth & Environment, 2(1), 1-9. https://doi.org/10.1038/s43247-020-00086-3

Kato, A., & Ueda, T. (2019). Source fault model of the 2018 Mw 5.6 northern Osaka earthquake, Japan, inferred from the aftershock sequence. Earth, Planets and Space, 71(1), 1-9. https://doi.org/10.1186/s40623-019-0995-9

Katoh, S., Iio, Y., Katao, H., Sawada, M., Tomisaka, K., Miura, T., & Yoneda, I. (2018). The relationship between S-wave reflectors and deep low-frequency earthquakes in the northern Kinki district, southwestern Japan. Earth, Planets and Space, 70(1), 1-11. https://doi.org/10.1186/s40623-018-0921-6

Katsura, I. (1990). Block structure bounded by active strike-slip faults in the northern part of Kinki district, southwest Japan. Memoirs of the Faculty of Science, Kyoto University. Series of geology and mineralogy, 55(1-2), 57-123. Retrieved from Kyoto University Research Information Repository. (http://hdl.handle.net/2433/186665)

Legendre, C. P., Zhao, L., & Tseng, T. L. (2021). Large-scale variation in seismic anisotropy in the crust and upper mantle beneath Anatolia, Turkey. Communications Earth & Environment, 2(1), 1-7. https://doi.org/10.1038/s43247-021-00142-6

Li, T., Gu, Y. J., Wang, Z., Wang, R., Chen, Y., Song, T. R. A., & Wang, R. (2019). Spatiotemporal variations in crustal seismic anisotropy surrounding induced

earthquakes near Fox Creek, Alberta. Geophysical Research Letters, 46(10), 5180-5189. https://doi.org/10.1029/2018GL081766

Li, C., Yao, H., Fang, H., Huang, X., Wan, K., Zhang, H., & Wang, K. (2016). 3D near-surface shear-wave velocity structure from ambient-noise tomography and borehole data in the Hefei urban area, China. Seismological Research Letters, 87(4), 882-892. https://doi.org/10.1785/0220150257

Lin, F. C., Moschetti, M. P., & Ritzwoller, M. H. (2008). Surface wave tomography of the western United States from ambient seismic noise: Rayleigh and Love wave phase velocity maps. Geophysical Journal International, 173(1), 281-298. https://doi.org/10.1111/j.1365-246X.2008.03720.x

Liu, C., Yao, H., Yang, H. Y., Shen, W., Fang, H., Hu, S., & Qiao, L. (2019). Direct inversion for three-dimensional shear wave speed azimuthal anisotropy based on surface wave ray tracing: Methodology and application to Yunnan, southwest China. Journal of Geophysical Research: Solid Earth, 124(11), 11394-11413. https://doi.org/10.1029/2018JB016920

Longuet-Higgins, M. S. (1950). A theory of the origin of microseisms. Philosophical Transactions of the Royal Society of London. Series A, Mathematical and Physical Sciences, 243(857), 1-35. https://doi.org/10.1098/rsta.1950.0012

Maeda, S., Toda, S., Matsuzawa, T., Otsubo, M., & Matsumoto, T. (2021). Influence of crustal lithology and the thermal state on microseismicity in the Wakayama region, southern Honshu, Japan. earth, planets and space, 73(1), 1-10. https://doi.org/10.1186/s40623-021-01503-3

Matsushita, S. (1963). Geological history of the Kinki District, Japan during the Cainozoic Era (Preliminary note). Special Contributions of the Geophysical Institute, Kyoto University, 2, 113-124.Retrieved from Kyoto University Research Information Repository. (http://hdl.handle.net/2433/178442)

Matsushita, R., & Imanishi, K. (2015). Stress fields in and around metropolitan Osaka, Japan, deduced from microearthquake focal mechanisms. Tectonophysics, 642, 46-57. https://doi.org/10.1016/j.tecto.2014.12.011

Matsubara, M., Obara, K., & Kasahara, K. (2008). Three-dimensional P-and S-wave velocity structures beneath the Japan Islands obtained by high-density seismic stations by seismic tomography. Tectonophysics, 454(1-4), 86-103. https://doi.org/10.1016/j.tecto.2008.04.016

Mazzotti, S., Le Pichon, X., Henry, P., & Miyazaki, S. I. (2000). Full interseismic locking of the Nankai and Japan-west Kurile subduction zones: An analysis of uniform elastic strain accumulation in Japan constrained by permanent GPS. Journal of Geophysical Research: Solid Earth, 105(B6), 13159-13177. https://doi.org/10.1029/2000JB900060

Mitamura, M., Matsuyama, N., Nakagawa, K., Yamamoto, K., & Suwa, S. (1994). Stratigraphy and subsurface structure of Holocene deposits around Uemachi Upland in the central Osaka Plain. Journal of Geosciences, Osaka City University, 37, 183-212.

Mitchell, T. M., Ben-Zion, Y., & Shimamoto, T. (2011). Pulverized fault rocks and damage asymmetry along the Arima-Takatsuki Tectonic Line, Japan. Earth and Planetary Science Letters, 308(3-4), 284-297. https://doi.org/10.1016/j.epsl.2011.04.023

Miyamura, M., Yoahida, F., Yamada, N., Sato, T., & Sangawa, A. (1981). Geology of the Kameyama district, Quadrangle Series, Scale 1: 50,000. Geological Survey of Japan 128.

Miyazaki, S. I., & Heki, K. (2001). Crustal velocity field of southwest Japan: Subduction and arc-arc collision. Journal of Geophysical Research: Solid Earth, 106(B3), 4305-4326. https://doi.org/10.1029/2000JB900312

Mizuno, T., Yomogida, K., Ito, H., & Kuwahara, Y. (2001). Spatial distribution of shear wave anisotropy in the crust of the southern Hyogo region by borehole observations. Geophysical Journal International, 147(3), 528-542. https://doi.org/10.1046/j.1365-246x.2001.01534.x

Mogi, T., Katsura, I., & Nishimura, S. (1991). Magnetotelluric survey of an active fault system in the northern part of Kinki District, southwest Japan. Journal of structural geology, 13(2), 235-240. https://doi.org/10.1016/0191-8141(91)90070-Y

Montagner, J. P. (1994). Can seismology tell us anything about convection in the mantle?. Reviews of Geophysics, 32(2), 115-137. https://doi.org/10.1029/94RG00099

Montagner, J. P., & Nataf, H. C. (1986). A simple method for inverting the azimuthal anisotropy of surface waves. Journal of Geophysical Research: Solid Earth, 91(B1), 511-520. https://doi.org/10.1029/JB091iB01p00511

Montagner, J. P., & Tanimoto, T. (1991). Global upper mantle tomography of seismic velocities and anisotropies. Journal of Geophysical Research: Solid Earth, 96(B12), 20337-20351. https://doi.org/10.1029/91JB01890

Nakae, S. (1993). Jurassic accretionary complex of the Tamba Terrane, Southwest Japan, and its formative process. Jour. Geosci., Osaka City Univ, 36, 15-70.

Nakajima, T. (1994). The Ryoke plutonometamorphic belt: crustal section of the Cretaceous Eurasian continental margin. Lithos, 33(1-3), 51-66. https://doi.org/10.1016/0024-4937(94)90053-1

Nakajima, J., & Hasegawa, A. (2007). Subduction of the Philippine Sea plate beneath southwestern Japan: Slab geometry and its relationship to arc magmatism. Journal of Geophysical Research: Solid Earth, 112(B8). https://doi.org/10.1029/2006JB004770

Nakajima, J., Hirose, F., & Hasegawa, A. (2009). Seismotectonics beneath the Tokyo metropolitan area, Japan: Effect of slab-slab contact and overlap on seismicity. Journal of Geophysical Research: Solid Earth, 114(B8), 1-23. https://doi.org/10.1029/2008JB006101

Nakajima, J., & Matsuzawa, T. (2017). Anelastic properties beneath the Niigata–Kobe tectonic zone, Japan. Earth, Planets and Space, 69(1), 1-9. https://doi.org/10.1186/s40623-017-0619-1

Nakata, T., & Imaizumi, T. (2002). Digital active fault map of Japan, University of Tokyo press, Tokyo (in Japanese).

Nakayama, K. (1996). Depositional models for fluvial sediments in an intra-arc basin: an example from the Upper Cenozoic Tokai Group in Japan. Sedimentary Geology, 101(3-4), 193-211. https://doi.org/10.1016/0037-0738(95)00065-8

Nimiya, H., Ikeda, T., & Tsuji, T. (2020). Three-Dimensional S Wave Velocity Structure of Central Japan Estimated by Surface-Wave Tomography Using Ambient Noise. Journal of Geophysical Research: Solid Earth, 125(4), e2019JB019043. https://doi.org/10.1029/2019JB019043

Nishida, K., Kawakatsu, H., & Obara, K. (2008). Three-dimensional crustal S wave velocity structure in Japan using microseismic data recorded by Hi-net tiltmeters. Journal of Geophysical Research: Solid Earth, 113(B10), 1-22. https://doi.org/10.1029/2007JB005395

Nishiwaki, H., Okudaira, T., Ishii, K., & Mitamura, M. (2021). Dip angles of active faults from the surface to the seismogenic zone inferred from a 2D numerical analysis of visco-elasto-plastic models: a case study for the Osaka Plain. Earth, Planets and Space, 73(1), 1-18. https://doi.org/10.1186/s40623-021-01390-8

Obara, K., Kasahara, K., Hori, S., & Okada, Y. (2005). A densely distributed high-sensitivity seismograph network in Japan: Hi-net by National Research Institute for Earth Science and Disaster Prevention. Review of scientific instruments, 76(2), 021301. https://doi.org/10.1063/1.1854197

Oike, K. (1976). Spatial and temporal distribution of micro-earthquakes and active faults. Mem. Geol. Soc. Japan, 12, 59-73.

Ojo, A. O., Ni, S., Chen, H., & Xie, J. (2018). Crust-mantle coupling mechanism in Cameroon, West Africa, revealed by 3D S-wave velocity and azimuthal anisotropy. Physics of the Earth and Planetary Interiors, 274, 195-213. https://doi.org/10.1016/j.pepi.2017.12.006

Okamura, Y., & Shishikura, M. (2020). New hypothesis to explain Quaternary forearc deformation and the variety of plate boundary earthquakes along the Suruga–Nankai Trough by oblique subduction of undulations on the Philippine Sea Plate. Earth, Planets and Space, 72(1), 1-14. https://doi.org/10.1186/s40623-020-01183-5

Paige, C. C., & Saunders, M. A. (1982). LSQR: An algorithm for sparse linear equations and sparse least squares. ACM Transactions on Mathematical Software (TOMS), 8(1), 43-71. https://doi.org/10.1145/355984.355989

Pilz, M., Parolai, S., Picozzi, M., & Bindi, D. (2012). Three-dimensional shear wave velocity imaging by ambient seismic noise tomography. Geophysical Journal International, 189(1), 501-512. https://doi.org/10.1111/j.1365-246X.2011.05340.x

Rawlinson, N., & Sambridge, M. (2004). Wave front evolution in strongly heterogeneous layered media using the fast marching method. Geophysical Journal International, 156(3), 631-647. https://doi.org/10.1111/j.1365-246X.2004.02153.x

Research Group for Active Faults of Japan. (1991). Active faults in Japan: Sheet maps and inventories. University of Tokyo press, 437.

Sabra, K. G., Gerstoft, P., Roux, P., Kuperman, W. A., & Fehler, M. C. (2005). Surface wave tomography from microseisms in Southern California. Geophysical Research Letters, 32(14), 1-4. https://doi.org/10.1029/2005gl023155

Sadeghisorkhani, H., Gudmundsson, Ó., Roberts, R., & Tryggvason, A. (2016). Mapping the source distribution of microseisms using noise covariogram envelopes. Geophysical Journal International, 205(3), 1473-1491. https://doi.org/10.1093/gji/ggw092

Sadeghisorkhani, H., Gudmundsson, Ó., & Tryggvason, A. (2018). GSpecDisp: a matlab GUI package for phase-velocity dispersion measurements from ambient-noise correlations. Computers & Geosciences, 110, 41-53. https://doi.org/10.1016/j.cageo.2017.09.006

Sagiya, T., Miyazaki, S. I., & Tada, T. (2000). Continuous GPS array and present-day crustal deformation of Japan. Pure and applied Geophysics, 157(11), 2303-2322. https://doi.org/10.1007/PL00022507

Sato, H., Ito, K., Abe, S., Kato, N., Iwasaki, T., Hirata, N., Ikawa, T., & Kawanaka, T. (2009). Deep seismic reflection profiling across active reverse faults in the Kinki Triangle, central Japan. Tectonophysics, 472(1-4), 86-94. https://doi.org/10.1016/j.tecto.2008.06.014

Sato, H., Kato, N., Abe, S., Van Horne, A., & Takeda, T. (2015). Reactivation of an old plate interface as a strike-slip fault in a slip-partitioned system: Median Tectonic Line, SW Japan. Tectonophysics, 644, 58-67. https://doi.org/10.1016/j.tecto.2014.12.020

Savage, M. K. (1999). Seismic anisotropy and mantle deformation: what have we learned from shear wave splitting?. Reviews of Geophysics, 37(1), 65-106. https://doi.org/10.1029/98RG02075

Schaeffer, A. J., Lebedev, S., & Becker, T. W. (2016). Azimuthal seismic anisotropy in the Earth's upper mantle and the thickness of tectonic plates. Geophysical Supplements to the Monthly Notices of the Royal Astronomical Society, 207(2), 901-933. https://doi.org/10.1093/gji/ggw309

Schippkus, S., Zigone, D., Bokelmann, G., & AlpArray Working Group. (2018). Ambient-noise tomography of the wider Vienna Basin region. Geophysical Journal International, 215(1), 102-117. https://doi.org/10.1093/gji/ggy259

Sekiguchi, S. (1991). Three-dimensional Q structure beneath the Kanto-Tokai district, Japan. Tectonophysics, 195(1), 83-104. https://doi.org/10.1016/0040-1951(91)90145-I

Shapiro, N. M., & Campillo, M. (2004). Emergence of broadband Rayleigh waves from correlations of the ambient seismic noise. Geophysical Research Letters, 31(7). https://doi.org/10.1029/2004GL019491

Shapiro, N. M., Campillo, M., Stehly, L., & Ritzwoller, M. H. (2005). High-resolution surface-wave tomography from ambient seismic noise. Science, 307(5715), 1615-1618. https://doi.org/10.1126/science.1108339

Shapiro, N. M., & Ritzwoller, M. H. (2002). Monte-Carlo inversion for a global shear-velocity model of the crust and upper mantle. Geophysical Journal International, 151(1), 88-105. https://doi.org/10.1046/j.1365-246X.2002.01742.x

Shimazaki, K., & Zhao, Y. (2000). Dislocation model for strain accumulation in a plate collision zone. Earth, planets and space, 52(11), 1091-1094. https://doi.org/10.1186/BF03352336

Smith, M. L., & Dahlen, F. A. (1973). The azimuthal dependence of Love and Rayleigh wave propagation in a slightly anisotropic medium. Journal of Geophysical Research, 78(17), 3321-3333. https://doi.org/10.1029/JB078i017p03321

Suemoto, Y., Ikeda, T., Tsuji, T., & Iio, Y. (2020). Identification of a nascent tectonic boundary in the San-in area, southwest Japan, using a 3D S-wave velocity structure obtained by ambient noise surface wave tomography. Earth, Planets and Space, 72(1), 1-13. https://doi.org/10.1186/s40623-020-1139-y

Sugiyama, Y. (1992). Neotectonics of the forearc zone and the Setouchi Province in southwest Japan. Chishitsugaku ronshū, 40, 219-233.

Taira, A. (2001). Tectonic evolution of the Japanese island arc system. Annual Review of Earth and Planetary Sciences, 29(1), 109-134. https://doi.org/10.1146/annurev.earth.29.1.109

Takemura, K. (1983). The Plio-Pleistocene Tokai Group and the tectonic development around Ise Bay of central Japan since Pliocene. Mem Fac Sci Kyoto Univ Ser Geol

Mineral 51:21-96. Retrieved from Kyoto University Research Information Repository. (http://hdl.handle.net/2433/186655)

Takemura, K., Haraguchi, T., Kusumoto, S., & Itoh, Y. (2013). Tectonic basin formation in and around Lake Biwa, Central Japan. Mechan. Sedim. Basin Form, 9, 209-229. https://doi.org/10.5772/56667

Tamura, T., Oohashi, K., Otsubo, M., Miyakawa, A., & Niwa, M. (2020). Contribution to crustal strain accumulation of minor faults: a case study across the Niigata–Kobe Tectonic Zone, Japan. Earth, Planets and Space, 72(1), 1-17. https://doi.org/10.1186/s40623-020-1132-5

Teanby, N. A., Kendall, J. M., & Van der Baan, M. (2004). Automation of shear-wave splitting measurements using cluster analysis. Bulletin of the Seismological Society of America, 94(2), 453-463. https://doi.org/10.1785/0120030123

Tsai, V. C., & Moschetti, M. P. (2010). An explicit relationship between time-domain noise correlation and spatial autocorrelation (SPAC) results. Geophysical Journal International, 182(1), 454-460. https://doi.org/10.1111/j.1365-246X.2010.04633.x

Tsuji, T., Dvorkin, J., Mavko, G., Nakata, N., Matsuoka, T., Nakanishi, A., Kodaira, S., & Nishizawa, O. (2011). VP/VS ratio and shear-wave splitting in the Nankai Trough seismogenic zone: Insights into effective stress, pore pressure, and sediment consolidation. Geophysics, 76(3), WA71-WA82. https://doi.org/10.1190/1.3560018

Tsuji, T., Ashi, J., Strasser, M., Kimura, G., 2015. Identification of the static backstop and its influence on the evolution of the accretionary prism in the Nankai Trough, Earth and Planetary Science Letters, 431, 15-25, https://doi.org/10.1016/j.epsl.2015.09.011

Uchide, T., Shiina, T., & Imanishi, K. (2022). Stress map of Japan: Detailed nationwide crustal stress field inferred from focal mechanism solutions of numerous microearthquakes. Journal of Geophysical Research: Solid Earth, 127(6), e2022JB024036. https://doi.org/10.1029/2022JB024036

Ukawa, M., 1982. Lateral stretching of the Philippine Sea plate subducting along the Nankai‐Suruga trough. Tectonics, 1(6), 543-571. https://doi.org/10.1029/TC001i006p00543

Usami, T. (2003). Materials for comprehensive list of destructive earthquakes in Japan. Univ. of Tokyo Press, Tokyo, 605.

Wakita, K. (2013). Geology and tectonics of Japanese islands: a review–the key to understanding the geology of Asia. Journal of Asian Earth Sciences, 72, 75-87. https://doi.org/10.1016/j.jseaes.2012.04.014

Wang, M., Hubbard, J., Plesch, A., Shaw, J. H., & Wang, L. (2016). Three-dimensional seismic velocity structure in the Sichuan basin, China. Journal of Geophysical Research: Solid Earth, 121(2), 1007-1022. https://doi.org/10.1002/2015JB012644

Wang, Z., & Zhao, D. (2021). 3D anisotropic structure of the Japan subduction zone. Science advances, 7(4), eabc9620. https://doi.org/10.1126/sciadv.abc9620

Weaver, R. L., & Lobkis, O. I. (2004). Diffuse fields in open systems and the emergence of the Green's function (L). The Journal of the Acoustical Society of America, 116(5), 2731-2734. https://doi.org/10.1121/1.1810232

Wu, C., Xu, T., Ai, Y., Dong, W., Li, L., & Hou, J. (2021). Crustal azimuthal anisotropy in the Jiaodong Peninsula: Evidence for the suture between the North China Craton and South China Block. Physics of the Earth and Planetary Interiors, 314, 106705. https://doi.org/10.1016/j.pepi.2021.106705

Xu, X., Ding, Z., Li, L., & Niu, F. (2021). Crustal Anisotropy Beneath the Trans-North China Orogen and its Adjacent Areas From Receiver Functions. Frontiers in Earth Science, 998. https://doi.org/10.3389/feart.2021.753612

Yang, Y. (2014). Application of teleseismic long-period surface waves from ambient noise in regional surface wave tomography: a case study in western USA. Geophysical Journal International, 198(3), 1644-1652. https://doi.org/10.1093/gji/ggu234

Yang, H. Y., & Hung, S. H. (2005). Validation of ray and wave theoretical travel times in heterogeneous random media. Geophysical research letters, 32(20). https://doi.org/10.1029/2005GL023501

Yang, Y., Yao, H., Zhang, P., & Chen, L. (2018). Crustal azimuthal anisotropy in the trans-North China orogen and adjacent regions from receiver functions. Science China Earth Sciences, 61(7), 903-913. https://doi.org/10.1007/s11430-017-9209-9

Yano, T. E., Takeda, T., Matsubara, M., & Shiomi, K. (2017). Japan unified high-resolution relocated catalog for earthquakes (JUICE): crustal seismicity beneath the Japanese Islands. Tectonophysics, 702, 19-28. https://doi.org/10.1016/j.tecto.2017.02.017

Yao, H., Beghein, C., & Van Der Hilst, R. D. (2008). Surface wave array tomography in SE Tibet from ambient seismic noise and two-station analysis-II. Crustal and upper-mantle structure. Geophysical Journal International, 173(1), 205-219. https://doi.org/10.1111/j.1365-246X.2007.03696.x

Yao, H., van Der Hilst, R. D., & De Hoop, M. V. (2006). Surface-wave array tomography in SE Tibet from ambient seismic noise and two-station analysis—I. Phase velocity maps. Geophysical Journal International, 166(2), 732-744. https://doi.org/10.1111/j.1365-246X.2006.03028.x

Yao, H., Van Der Hilst, R. D., & Montagner, J. P. (2010). Heterogeneity and anisotropy of the lithosphere of SE Tibet from surface wave array tomography. Journal of Geophysical Research: Solid Earth, 115(B12). https://doi.org/10.1029/2009JB007142

Yolsal-Cevikbilen, S., Biryol, C. B., Beck, S., Zandt, G., Taymaz, T., Adiyaman, H. E., & Özacar, A. A. (2012). 3-D crustal structure along the North Anatolian Fault Zone in north-central Anatolia revealed by local earthquake tomography. Geophysical Journal International, 188(3), 819-849. https://doi.org/10.1111/j.1365-246X.2011.05313.x

Appendices

Appendix A

Characterizing coal seams hosted in Mmamabula Coalfield, Central Botswana using pseudo-3D electrical resistivity imaging technique

Bokani Nthaba[a,b], Elisha Shemang[a*], Amogelang Hengari[a], Boniface Kgosidintsi[a], Takeshi Tsuji[b]

[a] Earth and Environmental Sciences Department, Botswana International University of Science and Technology, P/Bag 16, Palapye, Botswana.

[b] Earth Resources Engineering, Kyushu University, Fukuoka, Japan.

ABSTRACT

We used 2D and 3D electrical resistivity imaging (ERI) data inversion to locate and characterize the coal seams in Mmamabula Coalfield. The 2D ERI data inversion usually assumes that subsurface geological units (e.g., coal seams) are infinitely continuous in the direction perpendicular to the profiles. However, this assumption might be violated due to the heterogeneous nature of fluvial/deltaic environments. The lateral variation of the subsurface material can be effectively determined in 3D ERI inversion models. In this study, 2D ERI data were acquired along ten parallel profiles trending north-south, then inverted to produce 2D and 3D models. From the 2D ERI inversion results, we observed that the shallower coal seam occurs

around a consistent depth of 13.6 m whereas the second observable coal seam occurs at variable depths including at 50 m and 60 m along the two profiles. Discontinuities in coal seams were also identified. However, the information provided by 2D data inversion in such an environment is insufficient to determine the geometry of coal seams as well as to produce accurate and precise resource estimates for future exploitation. As an alternative, 3D data inversion gives better insight on the subsurface geology complexity and significantly resolves the geometry of coal within the study area. The presented 3D inversion results indicate that coal seams are intermittent and alternate well with other coexisting sedimentary units. We also deduced that they trend east-west and are split and adjoined in some areas along the north-south direction. Overall, 3D data inversion result resolves the elongated coal seams in Mmamabula Coalfield and reveals additional information that cannot be determined on 2D ERI inversion results.

Keywords: Coal seams, Electrical resistivity imaging, Isosurface, Mmamabula Coal Field, Middle Ecca Subgroup

1. Introduction

Coal is an organic sedimentary rock that forms from the accumulation and preservation of plant materials buried millions of years ago, usually in swampy environments. Coal is the world's most abundant fossil fuel with approximately 990 billion tonnes of coal reserves (BGR, 2009). Coal fuels ~42% of global electricity production, and is still expected to fill a significant role in meeting electricity demands well into the foreseeable future, especially with the growing demand in developing countries (Mohammed et al., 2016). In Botswana, the coal resources require detailed exploration and evaluation, with current coal reserves estimated to be 212 billion tonnes (Grynberg, 2012). Once proven, these figures are likely to make Botswana one

of the world's largest producers of coal. Despite multiple discoveries of coal reserves in Botswana, only one coal mine (Morupule) is operating at present. Due to the current instability in mining and insufficient energy supply to the nation it is necessary to study the unexploited Mmamabula coal reserve, which is reported to host coal deposits of identical grade (sub-bituminous to bituminous) to those at Morupule (Grynberg, 2012). As such, to assess and manage coal resources in green-fields (e.g., Mmamabula coal field) and in operational sites (e.g., Morupule), it is necessary to develop a good insight of the nature and distribution of the coal resources in those sites.

The use of exploration geophysics is not only limited to detecting new coal deposits, but its application also extends to assessing the nature of new or existing deposits to determine the quantity and quality of the coal contained. The techniques used in exploration geophysics also play a key role in detecting intrusive dykes and sills, as well as in identifying structural and in-seam discontinuities such as faults and lenses (Van Schoor & Fourie, 2014) which may adversely impact the future mining operations. The successful application of surface geophysical measurements for these purposes relies on the existence of suitable contrasts between the physical properties of target strata and those of surrounding materials (Green et al., 1988; Johnson–D'Appolonia, 2003). The unique physical properties of coal make it a suitable target for detection by geophysical methods. Coal is distinct from other sedimentary rocks in that it exhibits very low density, low gamma ray, and very high electrical resistivity (Ayodeji et al., 2018; Green et al., 1988). These properties make coal an excellent target for exploration using surface based geophysical techniques. Coal seams, especially those of sub-bituminous and bituminous grade usually have high resistivities compared to other sedimentary rocks such as shale, mudstones and fine sandstones, which generally have lower resistivities (Ayodeji et al., 2018; Ewing et al., 1936; Johnson–D'Appolonia, 2003; Kang, 2009; Reeves, 1981). Such contrasts form the basis for distinguishing coal from other sedimentary rocks.

However, some sedimentary rocks such as resistive sandstones and limestone constitute high resistivity anomalies and may be mistaken for coal (Wood et al., 1983). Fortunately, limestone beds are absent in Mmamabula Coalfield (Carney et al., 1994; Green, 1961; Williamson, 1996).

There is a great need for the use of non-invasive geophysical techniques with better data density to investigate the Mmamabula coal area in order to support its future exploration and possibly subsequent coal mining processes. In our study, we employ the electrical resistivity imaging (ERI) method, with particular emphasis on the effectiveness of pseudo-3D ERI surveys using parallel 2D profiles for investigation of coal seams hosted in an environment characterized by a complexity of fluvial and delta plain systems. In the past decades, substantial advances have been made towards improving the quality of interpretation of geological structures and effective means of delineating coal seams through the use of electrical resistivity methods (e.g., Mohammed et al., 2016; Krishnamurthy et al., 2009; Rao et al., 2015; Samanlangi, 2018; Singh et al., 2004; Van Schoor & Fourie, 2014). However, in complex geologic environments frequently encountered in coal exploration, even 2D data inversions are often inadequate and limited when interpreting complex 3D geologic structures. Due to the uncertainty and limitation of 2D data inversion in characterizing 3D geologic structures, we postulate that the widespread application of pseudo-3D ERI succeeded by 3D data inversion as a primary coal exploration tool in deltaic environments warrants more quantitative interpretation of the complex nature of coal seams and associated geologic structures than is currently offered by single or multiple-divergent 2D resistivity profiles investigations. The goal of this study is therefore to acquire multiple 2D ERI parallel profiles, from which 2D data inversion of selected profiles and 3D data inversion of the collated 2D data files will be carried out in order to delineate the coal seams, detect coal seam discontinuities, and determine the general coal seam geometry in the area.

2. Location and geological setting

The study area is situated between 23.5916^0 S to 23.5975^0 S latitudes and 26.5788^0 E to 26.5724^0 E longitudes in the Mmamabula coal area (Fig 1a), within the northeast-southwest trending Kalahari Karoo Basin (KKB) in Botswana (Carney et al., 1994). Mmamabula coal area occurs in a roughly triangular up-faulted area lying between the converging east-north-east trending Zoetfontein and the north-north-west trending Mabuane faults (Green, 1961).

The three coal seams present in our study area are located within the Mmamabula and Dibete Formations, and within the Middle Stage of the Ecca Series (Carney et al., 1994; Green, 1961; Spalding, 1999) (Fig. 1b). The lowest of the three seams is hosted within the Mmamabula Formation, and consists of mixed bright banded coal with few laminations of shale (Carney et al., 1994; Spalding, 1999). Similarly, the middle coal seam lies at the base of Mmamabula Formation and is separated from the lower coal seam by feldspathic, gritty sandstone, thin mudstones and many bands of carbonaceous mudstone (Spalding, 1999). The upper coal seam is situated within the Dibete Formation and occurs roughly 10 m above the middle coal seam, and comprises bright coal intercalated with carbonaceous bands of shale (Spalding, 1999).

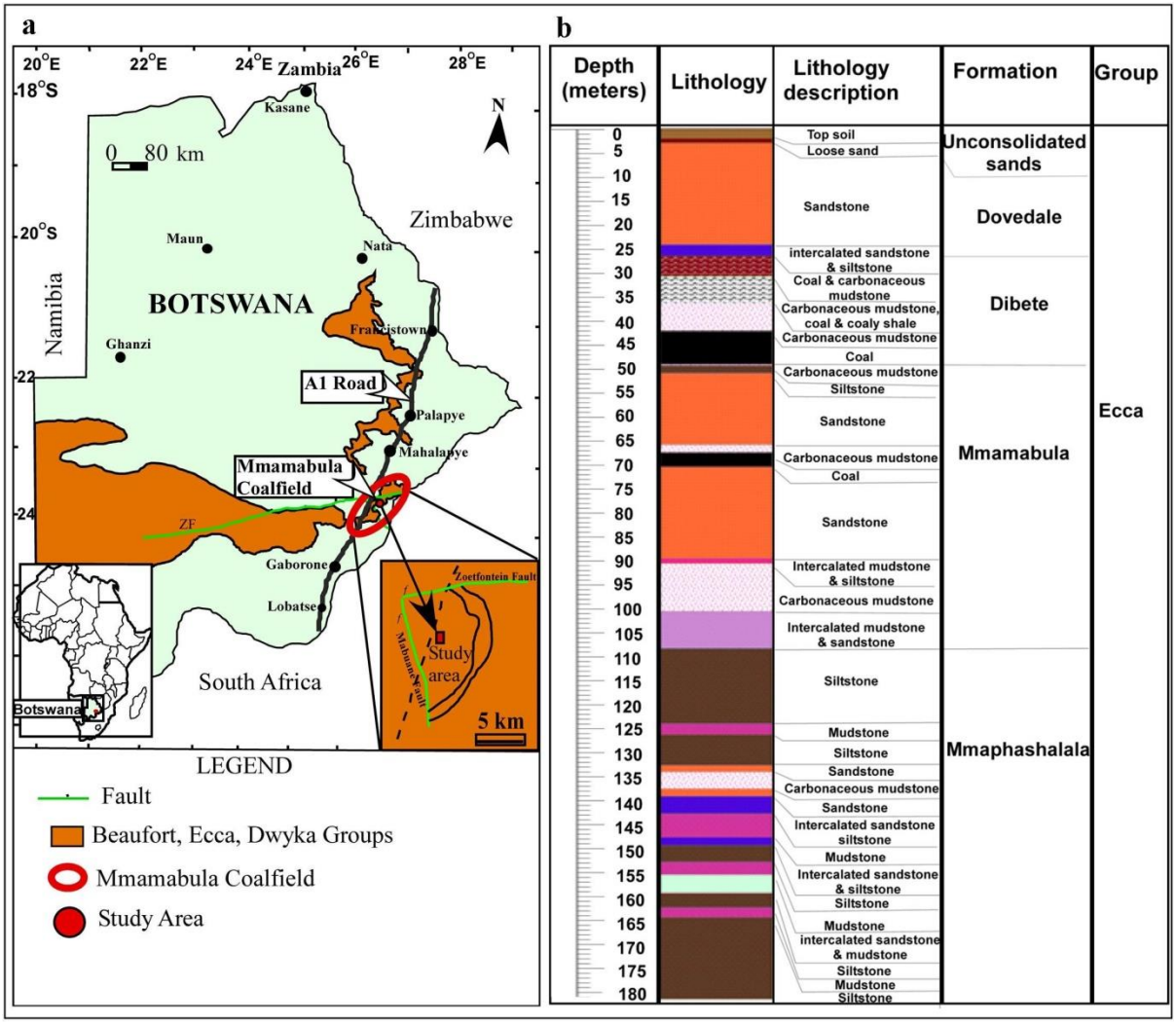

Fig.1. (a) Distribution of the Karoo Supergroup and the location of Mmamabula Coalfield (red circle) (modified from Carney et al., 1994) and an insert showing the geographic location of Botswana in Africa, (b) the stratigraphic and depositional sequence of the Mmamabula Coalfield, as established from the BOTC181borehole. The coal seams occur within the Dibete and Mmamabula Formations.

3. Data and Method

3.1 Data

Electrical resistivity imaging method was adopted for this study using the SYSCAL Pro™ resistivity/IP equipment, which is a ten-channel multi-electrode resistivity meter that uses a command file to acquire measurements from pre-determined current electrode and potential electrode configurations. It combines a transmitter, a receiver and a switching unit in one single casing. The SYSCAL Pro Switch uses multi-core cables for controlling a set of electrodes. Ten parallel 2D resistivity profiles of 470 m length and 50 m profile spacing were established across the general strike (E-W) of the geologic units in a 470 m by 450 m area (Fig. 2). A dipole-dipole electrode configuration was used to acquire resistivity measurements because of its better lateral resolution and efficiency when used with the multichannel reception system (Akingboye & Ogunyele, 2019; Mahato, 2018; Stummer et al., 2004).

Data acquisition was conducted shortly after the rainy season (April-2019) to obtain good ground-electrode contact. The field campaign lasted for five (5) days, in which two (2) profiles were completed each day. The SYSCAL Pro Switch units use segmented imaging cables with one take-out every 5 m or 10 m adjustable (adjustable electrode spacing). The depth of investigation is a function of the spread length employed (electrode spacing times the number of electrodes) and varies as a function of subsurface electrical resistivities (Loke, 1994). The maximum depth of investigation is typically of the order of 0.2 times the total spread length (Bernard, 2003; Ismail & Anderson, 2012). In this study, a 10 m electrode separation was used in order to achieve a maximum investigation depth of approximately 100 m. Stainless steel electrodes were driven at least 10 cm into the ground to establish good ground-electrode contact. Ground coupling was checked before the survey was undertaken. High contact resistances were successfully lowered by adding brine to the ground. A transmitter-current injection time window (T_n) was set to be 4 seconds and performed 3 to 6 stacks to improve the signal-to-noise ratio without significantly affecting the rate of acquisition. The quality factor (i.e., the standard deviation of the stacked signal) was set to be 3 %.

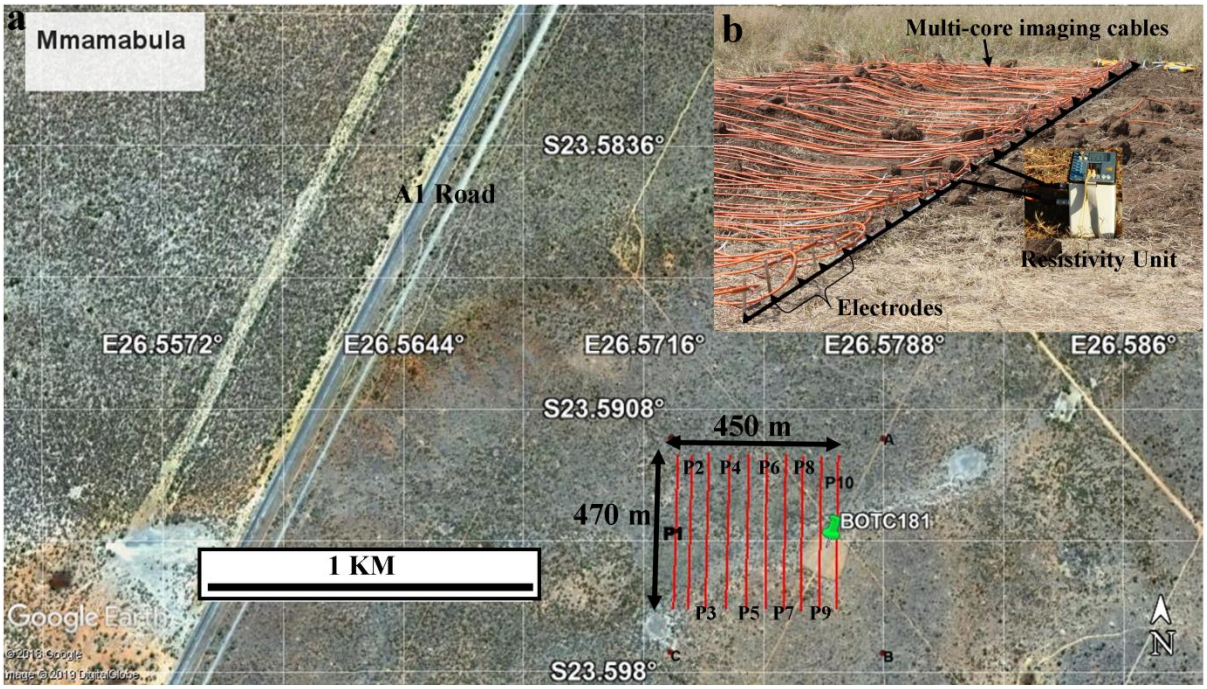

Fig. 2. (a) Satellite image showing the layout of the 10 profiles surveyed and, (b) an insertion showing data acquisition setup consisting of the Syscal Pro resistivity unit, multi-core imaging cable laid on the ground and stainless steel electrodes planted into the ground and connected to the multi-core cables via the connecting cables. Profile denotations are given by the letter P preceding the respective profile numbers.

3.2 Method

The 2D electrical resistivity data collected along the 10 profiles each with 906 data points were prepared for both 2D and 3D data inversions. Firstly, all the datasets were filtered to eliminate spurious apparent resistivity data points, which are likely to have resulted from bad electrodes contact, instrumental errors (the wrong current injection and receiving noise potentials) and background noise. Secondly, an additional file was created by consolidating the ten 2D datasets into a single text file for 3D data inversion. Consolidation of the 2D data files

arranged the apparent resistivity measurements of the ten profiles and the electrodes layout in a rectangular grid according to the electrode positions and direction of the ten profiles used.

The measured ERI data were inverted using the Res2Dinv (Loke, 2016) and Res3Dinv (Loke, 2017) software, applying the smoothness-constrained nonlinear least-square algorithm to the model perturbation vector and model resistivity values as well. The inversion routine uses a homogeneous starting model of the subsurface with logarithmic averages of the measured apparent resistivity values (Loke & Barker, 1995). In the inversion routine, the subsurface is divided into a large number of rectangular cells and the optimization method of the user's preference seeks to determine the true resistivity distribution of the cells that minimizes the difference between the calculated and measured apparent resistivity values (Loke et al., 2003; Sjödahl, 2006; Ganse, 2008). We used the standard Gauss-Newton optimization method, in which the program solves the least-squares equation using double precision calculations (Claerbout & Muir, 1973; Loke, 2003). A measure of the difference between the measured and the calculated resistivity values is given by the root-mean-square (RMS) error. Equation (1) below is solved in the inversion procedure.

$$(\mathbf{J}_i^T\mathbf{R}_d\mathbf{J}_i + \lambda_i\mathbf{W}^T\mathbf{R}_m\mathbf{W})\Delta r_i = \mathbf{J}_i^T\mathbf{R}_d g_i - \lambda_i\mathbf{W}^T\mathbf{R}_m\mathbf{W}r_{i-1} \quad \ldots\ldots (1).$$

where $\mathbf{g_i}$ is the data misfit vector containing the difference between the logarithms of the calculated and the apparent resistivity values, **J** is the Jacobian matrix of partial derivatives, Δr_i is the change in the model parameter for the i^{th} iteration and r_{i-1} is the model parameters vector for the previous iteration, containing the logarithm of the model resistivity values and **W** is a first-order roughness filter (deGroot-Hedlin & Constable, 1990).

Since the resolution of the resistivity method decreases exponentially with depth, we setup the damping factor to start at a program default value of 1.25 given the satisfactory quality of the data, and to increase by 1.20 times with each deeper layer in order to stabilize the

inversion process. The damping factor determines the relative importance given to minimizing the model roughness and the data misfit (Sjödahl, 2006). $\mathbf{R}_d$ and $\mathbf{R}_m$ are weighting matrices introduced to modify the weights given to the different elements of the data misfit and model roughness vectors. The robust constraint (L1-norm) and the standard least-squares constraint (L2-norm) can be used to minimize the data misfit and the model roughness by adjusting the form of these weighting matrices. The L1- norm minimizes the sum of the absolute values of the data misfit, whereas L2-norm attempts to minimize the square of the difference between the measured and calculated apparent resistivity values and tends to produce better results where the model resistivity changes in a smooth manner (typical scenario in sedimentary basins) (Loke et al., 2003). To accommodate both scenarios, we used the combined scheme (the Marquardt and Occam inversion method), which combines the Marquardt (or dumped least square method) with the smoothness-constrained method. It seems to give better results in resolving compact structures where the width and the thickness are slightly smaller than the depth (Lecocq & Camelbeeck, 2017).

The target structures (coal seams) may be laterally extensive but can also assume the geometry of the elongated geologic structures (e.g., streams) especially when hosted in fluvial or deltaic environments. We therefore applied a smaller weight of 0.5 for the vertical filter and used equal horizontal filter weight (i.e., 1.0) in both the x- and y-directions. A detailed description of the inversion process is given in Farquharson & Oldenburg (1998), Loke & Dahlin (2002) and Loke et al. (2003).

To obtain better inversion models, trial inversions were performed, and RMS errors distribution was displayed in the form of a bar chart (Fig. 3a) and a correlation plot of the measured and calculated apparent resistivity values (Fig. 3b). Bad data points with relatively large errors were subsequently removed from the dataset before performing the final inversion process. It is expected that bad data points will have relatively large apparent resistivity

percentage errors, e.g., above 100 % (Loke, 2009). Hence, the data points with apparent resistivity percentage errors of 30 % or less were used. For 3D data inversion, only 8595 data points from an initial sum of 8650 data points were used in the final inversion.

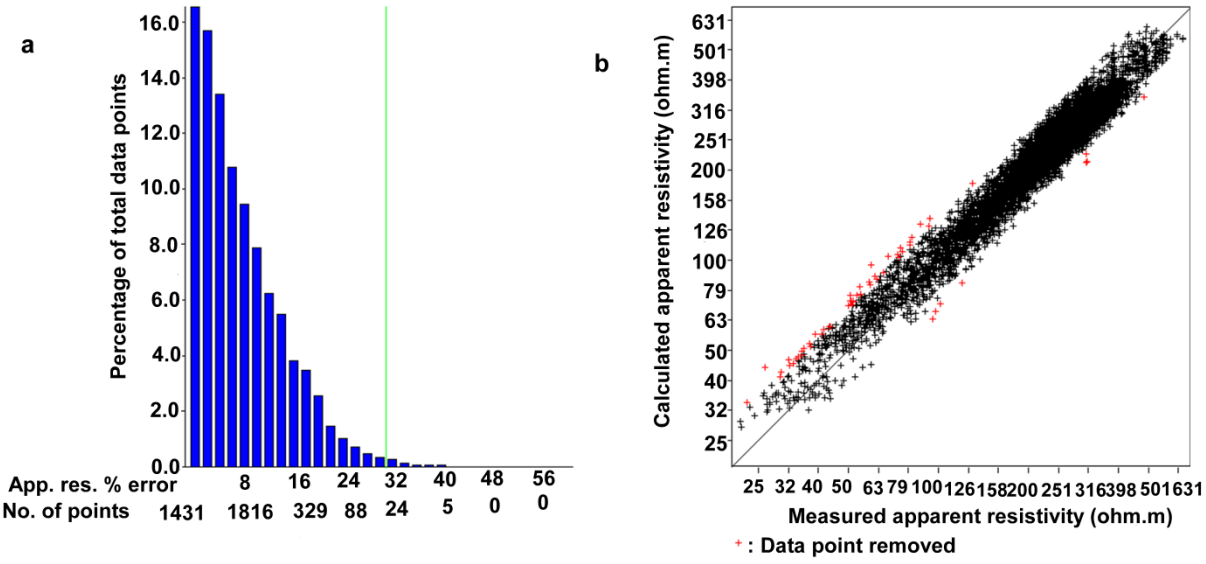

Fig. 3. (a) Bar chart showing the apparent resistivity percentage error distribution and, (b) correlation of the measured and calculated apparent resistivity values. Also shown on the bar chart is a green data selection line used to set the maximum cut-off error. The red dots on the correlation plot represent removed data points while the black dots represent retained data points

4. Results and Interpretation

4.1. 2D Resistivity models

The survey was conducted along 10 profiles, out of which three (Profile 2, Profile 6 and Profile 10 in Fig. 2) were processed to generate 2D inverse resistivity sections that were subsequently correlated with the stratigraphy log of BOTC181 borehole (Fig. 1b).

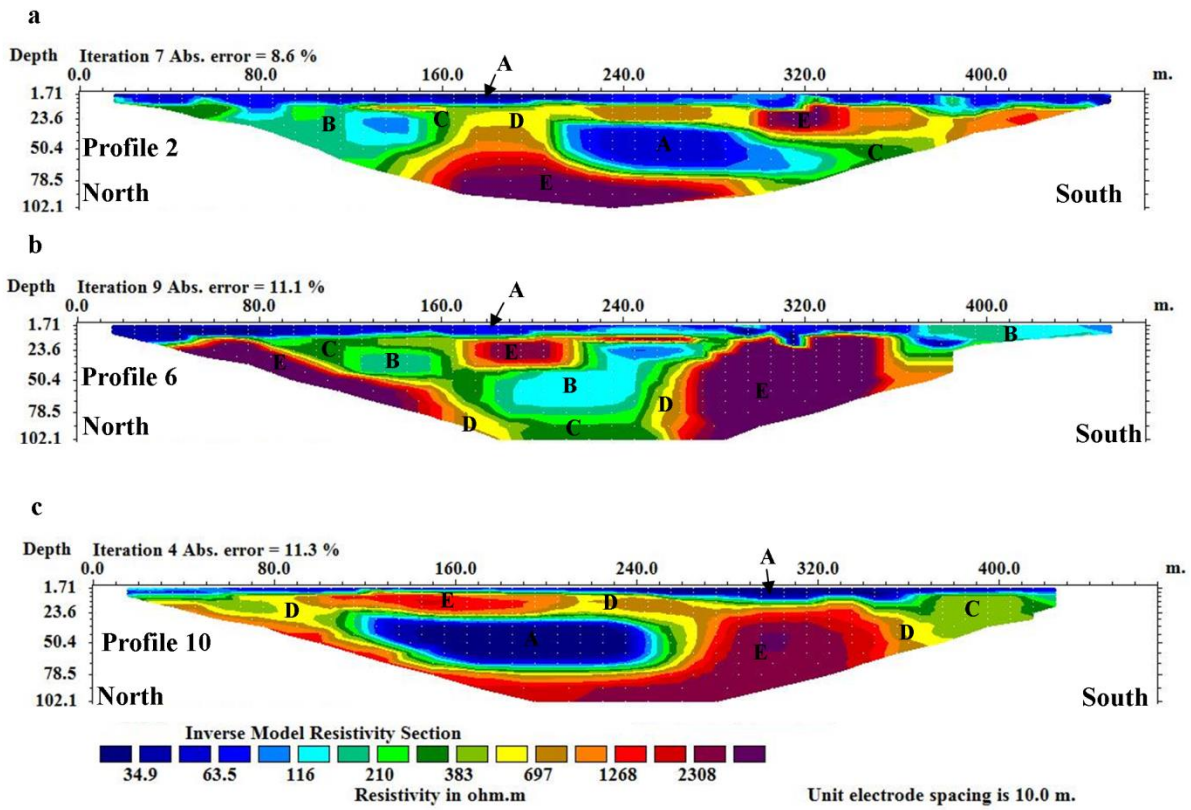

Fig. 4. (a) The inverse resistivity model of profile 2 situated at y=50 m, (b) the inverse model of profile 6 located at y=250 m and, (c) the inverse resistivity model of profile 10 located at y=450 m and 25 m to the west of borehole BOTC181. Letters A-E indicate observed electrical resistivity anomalies representing different geological units observed.

The inverse resistivity sections of the three profiles (profiles 2, 6 and 10) were interpreted to characterize the subsurface geology of the study area (Fig. 4). Our attribution of various resistivity ranges to specific formations in the study area was premised on the assumption that the information provided by Borehole BOTC181 stratigraphic log is representative of the area investigated, and was used as a guide for the resistivity models interpretation. The three resistivity models show the subsurface imaged to a depth of about 102.1 m, with electrical resistivity variation ranging from 34.9 to 3114 Ωm. The resistivity anomalies observed (A to E) represent different geological units consisting of a wide range of resistivity

values and variable spatial geometry. Of the marked anomalous zones, anomaly A has resistivity values ranging from 34.9 to 85.7 Ωm, attributable to the carbonaceous mudstones/shale or mudstones; anomaly B comprises of resistivity values ranging from 85.7 to 210 Ωm, and is inferred to represent intercalated fine sandstone and. Anomaly C comprises resistivity values ranging from 210 to 517 Ωm, attributable to the medium/coarse grained sandstones inter-bedded with siltstone. Anomaly D exhibits resistivity values ranging from 517 to 1,268 Ωm that corresponds to the coal and coaly shale zone. Coal is represented by relatively high resistivity anomalies (1,268 to 3,114 Ωm), denoted by E in the inverse resistivity sections. Anomaly A occupies the shallowest portions of all the models presented in Fig. 4 This lenticular-shaped zone is restricted to the central zones of profiles 2 and 10 (Figs. 4a, b). While anomalies C and D manifest as thin laminations around more prominent anomalies (A, B and D), anomaly E exhibits different geometries. It occurs as a stratiform layer in the central-north and shallower portions of the models (Fig. 4a-c). It also occurs as massive, vertically stretched bodies towards the end (south) of profiles 6 and 10 (Figs. 4b, c), while it seems to be an inclined plane at the beginning of profile 6 (Fig. 4b). These disparities in shape observed between the same anomalies (geological units) are testimony to the expected spatial geometry variability of the Mmamabula coal area and similar environments (Carney et al., 1994; Venable et al., 2013; Williamson, 1996).

Zones with identical anomalies along different profiles (Fig. 4a-c) do not correlate, alluding to the complexity in the subsurface geology. In all the presented inverse resistivity sections, the five prominent anomalies identified occur at variable depths and at different lateral locations. Anomaly A, inferred to be carbonaceous mudstones/shale appears to be prevalent along the shallowest zones (0-13.6 m) of the presented inverse resistivity sections (Fig. 4a-c). The same anomaly (A) appears to be restricted between 210-300 m along profile 2 (Fig. 4a), and between 120-240 m along profile 10 (Fig. 4c) at a depth of about 29.4 to 68 m. To the

contrary, at this depth range (29.4-68 m) in profile 6 (Fig. 4b), anomaly B which represents fine sandstone and siltstone is observed. Anomalies C and D do not exhibit a clear pattern or trend across the three presented profiles (Figs. 4a-c). Instead, they appear as thin laminations sandwiched between prominent anomalies A and E (Figs. 4a, c) or between B and E (Fig. 4b). Despite the obscured trend, coal (E) is evident in all the three resistivity sections (Figs. 4a-c). Laterally, it occurs at: 300-340 m and 160-290 m (Fig. 4a); 40-170 m, 170-220 m, 220-270 m, and 270-380 m (Fig. 4b); 90-210 m, 240-270 m, and 270-340 m (Fig. 4c). Likewise, its depth of placement varies. Coal occurs between 13.6 m to 38 m (Fig. 4a and 4b), between 46 m to 102.1 m (Fig. 4a); from 13.6 m to 102.1 m, 13.6 to 102.1 m (Fig. 4b); it also occurs at 13.6-29.4 m and is ubiquitous beneath 68 m depth (Fig. 4c). There is an apparent shift of the shallowest, stratiform-like coal seam zone observed (anomaly A, depth: 13.6-38.0 m) from the south (Fig. 4a) to the north (Fig. 4c).

4.2. 3D Resistivity models

The horizontal slices that exhibit the distribution of the electrical resistivity of the subsurface, generated from the consolidated datasets for the 10 profiles are presented in Fig. 5. The third dimension (depth) is given in numerical form above the respective horizontal slices. The horizontal slices show lateral resistivity variation at different depth levels. For a lucid comparison with the 2D models presented in Fig. 4, we used the same denotations for the anomalies. Anomaly A (carbonaceous mudstones/shale or mudstones) is evidently dominant in layers 1, 2 and 3 (depth: 0.0-12.2 m), with anomaly B (fine sandstone and siltstone) occupying the most central portion of the three shallower layers in Fig. 5. Layer 4 (depth: 12.2 -17.5 m) shows a slightly different pattern to that observed in overlying layers. The carbonaceous mudstones/shale (A) occupies the first 180 m along the x-axes and the intercalated fine

sandstones and siltstone (B) occur between 180 and 470 m along the x-axes. However, the central portion of layer 4 appears to be composed predominantly of admixed coarse grained sandstone and siltstone (C).

In layer 5, the edges are occupied by a mixture of fine sandstone and siltstone (B), whereas the inner zones are composed of medium-coarse grained sandstone and siltstone (C) which surround an isolated anomaly of coal and coaly shale (D). Layer 6 (depth: 23.6-30.6 m) is composed largely of medium-coarse sandstone and siltstone (C), with coal and coaly shale (D) restricted between 150 m and 280 m along the x-axes. In layer 7 (depth: 30.6-38.7 m) and layer 8 (depth: 38.7-48.0 m) a regular lateral alternation of sandstone/siltstone and coaly material is observed. Layers 9 to 12 (depth: 48.0-101.5 m) show similar arrangement of geologic units to the preceding layers, with an east-west trend.

From the presented 3D horizontal sections, it can be deduced that the coal seams observed in Fig. 5 are generally overlain predominantly by layers of mudstones/shale and in some portions fine sandstone intercalated with siltstone, and medium to coarse sandstones mixed with siltstones. Additionally, significant coal and coaly shale does not only appear to be interlayered with other sedimentary formations (sandstones, siltstones, shale and carbonaceous mudstones), but also occur in alternating pattern with these formations in the north-south direction, meandering throughout the y-direction (east-west) and adjoined in some areas.

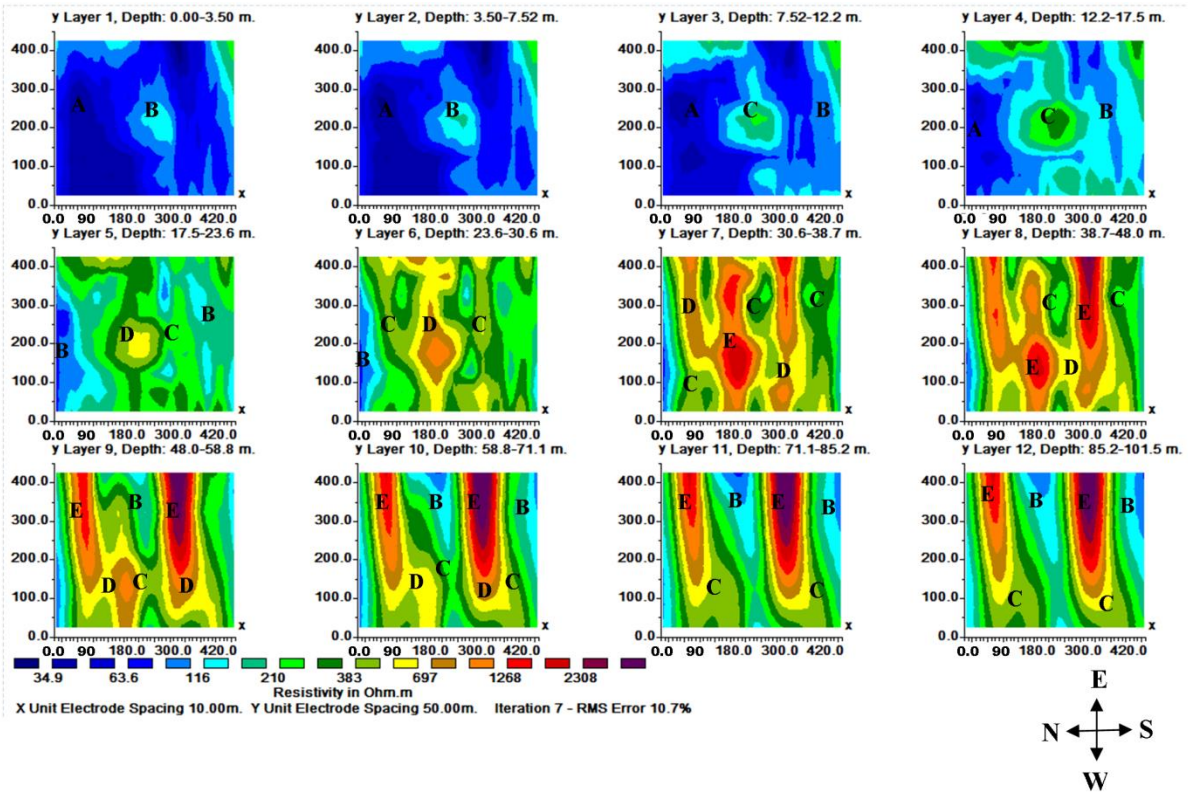

Fig.5. 3D horizontal (X-Y) plane resistivity distribution sections of the subsurface. The third dimension (Z) is given above each section (layer). The RMS error is 10.7 %. Letters A-E denote distinct electrical resistivity anomalies attributable to different geological lithologies.

Although the 2D inverse resistivity sections (Fig. 4) and the 3D horizontal sections (Fig. 5) of the data enable a satisfactory delineation of the surveyed area, they do not entirely provide lucid architectural framework and structural geometry of the area. Therefore, visualizing the data accurately has to be enhanced by plotting the data as resistivity isosurfaces. By this approach, the data are plotted to display features with similar resistivity values as continuous surfaces. It enables mapping features of interest (clustering the data according to the resistivity values of interest) while suppressing the resistivity values of the surrounding material. For this study, the key material of interest was coal and a mixture of coal and coaly shale and so the ERI results were plotted for a range of high resistivity values (517-3114 Ωm). This was able to map the external boundaries of coal and a mixture of coal and coaly shale which can clearly be

identified without being concealed by the presence of relatively low resistivity values of other sedimentary units. The Slicer Dicer Software (PIXOTEC, LLC, Slicer Dicer) was used to display the 3D resistivity isosurfaces of relatively high resistive features corresponding to regions of coal or coaly material (Fig. 6) in an attempt to analyze the 3D geometry of coal seams and how they relate to geological structures. The resulting high resistivity isosurface image of the surveyed area indicates that there are several zones of discontinuity in the coal seams. The coal seams also manifest as elongated structures which trend from east to west, and appear to be intermittent.

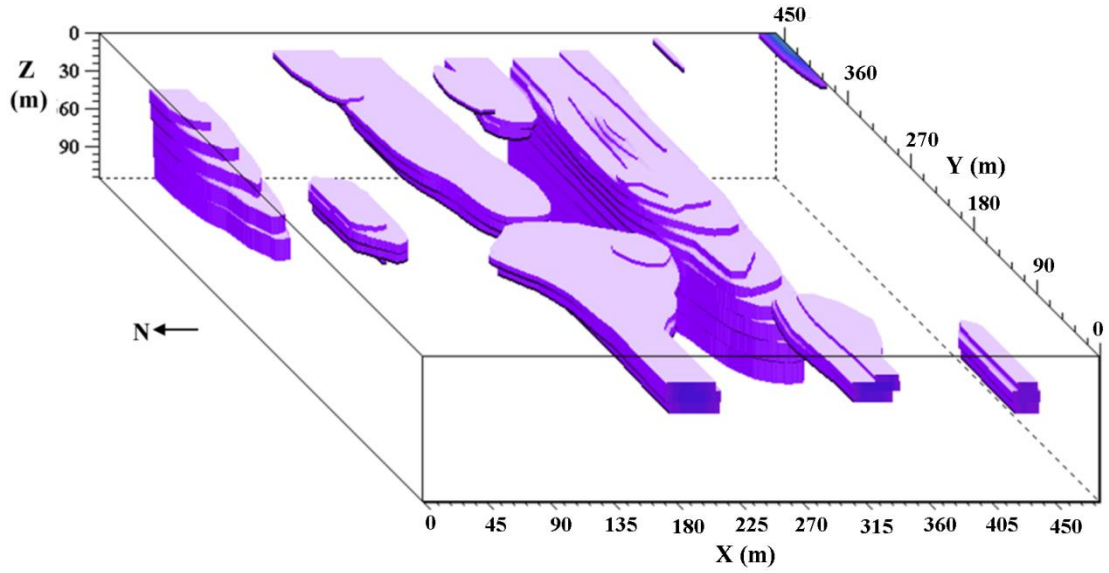

Fig. 6. 3D resistivity model from the Slicer Dicer program presented as isosurfaces showing only relatively high resistivity values ranging from 517 Ωm-3114 Ωm, representing both coal and coaly material.

5. Discussion

The study involved deployment of equally spaced parallel 2D profiles along which electrical resistivity data were acquired to enable the generation of 2D inverse subsurface

models. Consolidation of these parallel 2D profile datasets generated 3D horizontal sections to illustrate the distribution and variation of the subsurface electrical resistivity values along horizontal (x and y) and vertical (z) directions (Ismail & Anderson, 2012). The distinction of subsurface electrical resistivity values has been presented as 2D inverse resistivity model, 3D horizontal (x-y) sections and 3D volumetric isosurfaces across the study area.

Results from both 2D (Fig.4) and 3D resistivity horizontal sections (Fig. 5) indicate resistivity variations due to the heterogeneous nature of the subsurface geology within the study area at different locations. In particular, the 2D resistivity inverse models show the subsurface geology comprising the coal seams, carbonaceous mudstone/shale and other detrital sedimentary rocks such as siltstones and sandstones. Resistivity models presented in Fig. 4 indicate that the upper coal seam generally has negligible topographic undulations on which the overlying material was deposited, and the bottom surface does not entirely conform to irregularities that would otherwise be associated with ancient channels in the area. This implies that the upper coal seam may have been deposited at a time when most of the palaeo-channels had been filled with sediments and further supports a notion that the Upper Ecca Subgroup, which hosts the upper coal seam was accumulated at a time when many of the Karoo basin's topographic irregularities had been in-filled, and when rates of differential subsidence were more uniform over a greater area (Carney et al., 1994).

Coal seams and coaly shale occur as distinct high resistivity (>517 Ωm) anomalies both at shallow and deeper zones of the subsurface (Fig. 4). The distribution of coal seams along and below the respective profiles in Fig. 4 is also apparent, but the trend and spatial distribution of the coal seams and related geologic units is not easily discernible across the 2D profiles. This shows that although 2D ERI data inversions are widely accepted in coal exploration, they are limited in resolving 3D geologic structures when resistivity images are produced. This is in part due to the assumption by the inversion algorithm that the layers observed below the 2D profiles

are infinitely continuous in the direction perpendicular to the profile. This is often not the case, although the method provides a good picture of the cross-section.

The pseudo-3D survey through a set of equally spaced 10 profiles along which electrical resistivity measurements were obtained enabled generation of 3D horizontal sections (Fig. 5). Isosurface model (Fig. 6) which shows the distribution and variation of electrical resistivity along horizontal (x and y) and vertical (z) directions was also generated. We suggest that these models deliver significantly better representation of the coal geometry and the subsurface architecture compared to 2D electrical resistivity inverse models. The results from this study indicate that the coaly material is extensive in the east-west direction but lacks lateral continuity in the north-south direction, implying that they are split and adjoined in some zones. The absence of coals or coaly shale is marked by the occurrence of either carbonaceous mudstone/shale or intercalated siltstones and sandstones displaying the same trend, and manifesting as low resistivity anomalies (A, B and C) in Figs. 5 and 6. The findings of this study agree with those of Williamson (1996), who suggests that the Middle Ecca coal seams may be interlayered with the carbonaceous mudstone, sandstone, siltstone or the mudstone sequence. Alternating elongated resistivity anomalies which characterize the underlying zones of the 3D models also allude to the subsurface resistivity variation in a similar manner to that observed in 2D resistivity inverse models. However, 3D models go beyond the 2D resistivity results by confirming the spatial variation of electrical resistivity across the three orthogonal directions.

With these presentations (Figs. 5 and 6), multi-depositional facies are postulated to be alternating well with one another. According to Smith (1984) and Williamson (1996), depositional environments involving prolonged periods of inactive sedimentation are suspected for the coal and carbonaceous mudstone members. The logical explanation to this notion is that prevalent peat swamps and low-energy, interdistributary bay or flood plain lake deposits were developed, alternating well with one another and coexisting in part with fluvial-deltaic channels

so that some degree of diachronism is inevitable (Shang et al., 2018). In terms of the general geologic units layout, our findings are also in line with those of Carney et al. (1994), that the coals in Mmamabula area were accumulated in troughs formed due to syn-depositional differential subsidence or faulting, and that most of the coaly material in the area has been fragmented, suggesting fluvial transport prior to deposition.

Williamson (1996) suggested that lithological variations in coal and carbonaceous mudstone dominated members of the central Mmamabula coalfield occur both laterally and vertically so that it is not always possible to correlate similar beds or coal seams from borehole logging information. Similarly, our study demonstrates that it is equally challenging to get intelligible relationships between individual geologic units or coal seams from one 2D ERI profile to another. The application of 2D ERI inversion in a sedimentary basin hosting linearly shaped coal seams is limited to locating coal seams and identifying other coexisting earth materials occurring at variable depths, and its contribution in characterizing coal seams in terms of spatial geometry is limited. The significance of 3D resistivity models in coal exploration, particularly in an environment characterized by fluvial/deltaic systems cannot be overemphasized. However, it is evident from our results that 3D ERI technique warrants improved insight on coal geometry and the complex nature of the subsurface geology in this kind of environment and can help to elucidate the depositional facies of the coal bearing environments. From the presented 3D ERI models, we obtained more lucid lateral correlation of the coal seams and coexisting geologic units across the studied area, emphasizing the apparent cyclic pattern exhibited by the Mmamabula coals and other sedimentary units (sandstone, siltstone, carbonaceous mudstone/shale). This observation is attributed to the possibility of both the upper and lower delta plain-dominated facies associations having alternated and engendering the apparent cyclicity of Mmamabula formations (Williamson, 1996). In such a case, the sandstones and siltstones (anomaly B and C, in Figs. 4 and 5) are likely to represent a fluvially

dominated depositional environment possibly intermediate between the transitional and upper delta plains (Collinson, 1978). On the other hand, the presence of thick coal (E), coal and coaly shale (D), and carbonaceous mudstones/shale (A) sequences argues that lacustrine-marginal swamps and shallow-lacustrine quiescent interdistributary bays developed periodically in the Middle Ecca at the expense of the fluvial channel sedimentation (Williamson, 1996).

Despite the successful application of 3D ERI in resolving most of the shallow geologic units and unraveling the complex nature of the studied area, there are prevailing limitations of the ERI method in resolving the deeper-lying geologic units. A good correlation could not be achieved between our models (>50 m depth) and the BOTC181 borehole stratigraphic log (Fig. 1b), where we expected to resolve a low resistivity thick sequence of carbonaceous mudstone, siltstone and sandstone sandwiched by two highly resistive coal seams. The lack of correlation at greater depths may be attributed to the increased heterogeneous nature of the subsurface geology observed over a wider area compared to the single point geologic log observations. Conversely, the discrepancy is likely to be artefact of limitations in electrical resistivity method to resolve the sandwiched low resistive zone between the highly resistive middle and lower coal seams (Green et al., 1988). If the latter is true, longer ERI spread lengths with the ability to image deeper sections of the subsurface should be considered for future investigations. Also, jointly deploying 3D ERI technique with a method best suited for mapping hidden layers (Multichannel analysis of surface waves) should give the best results.

6. Conclusions

We propose using 3D resistivity data inversions in order to characterize the coal seams and geological setup of environments characterized by fluvial or deltaic systems. Our results demonstrate that compared to the conventional and widely adopted 2D resistivity data inversion,

3D ERI data inversion offers improved insight on the subsurface geology complexity and significantly resolves the coal seams geometry of such environments.

2D ERI data inversion is a good tool to identify coal seams, coal seam depths and coal seam discontinuities along and below the profiles. In 2D resistivity models we observed that the shallower coal seam occurs around a consistent depth of 13.6 m whereas the second observable coal seam occurs at variable depths including 50 m depth in profile 2 (Fig. 4b) and 68 m depth in profile 10 (Fig. 4c). Also, several zones of discontinuities were identified along the 2D profiles. However, this information is insufficient to provide accurate and precise resource estimates as well as positively influence decision making regarding the future mining operations. To better understand the subsurface geology complexity and resolve the geometry of coal seams and the coaly material within the study area, we employed the 3D ERI data inversion routine.

Our results show the elongated resistivity anomalies trending east-west, which correspond to the coal seams. The 3D models reveal that the coaly materials are extensive in the east-west direction, lack lateral continuity in the north-south direction implying that they are intermittent, split and adjoined in some zones. From the same 3D models (Fig. 5 and 6), we deduce that the coal geometry resembles the geometry of braided streams/channels in a fluvial or deltaic environment. We suspect that multi-depositional facies involving quiescent sedimentation may have existed. The cyclicity pattern exhibited by coal seams and carbonaceous mudstone members alongside channel deposits such as siltstone and sandstone suggest that peat swamps and low-energy, interdistributary bay or flood plain lake deposits may have developed, alternating with one another and coexisting in part with fluvial-deltaic channels.

Based on the results of this study, the pseudo-3D ERI method and 3D data inversion approach may serve as the basis for investigations in environments with similar characteristics

to those of Mmamabula coalfield, and its widespread application as a primary coal exploration tool in such environments warrants more quantitative interpretation of the complex nature of geologic structures and that of the coal seams with higher spatial resolution than is currently practiced.

Acknowledgements

I thank Botswana International University of Science and Technology for providing funding for this research. Nolens Projects (Pty) Ltd granted us permission to work in their license area, and for that we are grateful. A special thanks to C. Chhun and J. Kaavera (Kyushu University) for giving constructive comments for this manuscript. I would like to acknowledge the Japan International Cooperation Agency (JICA) for giving me the opportunity to participate in one of their long-term training programs, the Human Resources Development in the Mining Sector (KIZUNA Program) and for their support and funding during my PhD.

Data availability

The data used to support the findings of this study are available from the corresponding author upon request.

References

Akingboye, A. S., & Ogunyele, A. C. (2019). Insight into seismic refraction and electrical resistivity tomography techniques in subsurface investigations. *Rudarsko-geološko-naftni zbornik*, **34**, 93-111.

Ayodeji, O. S., Salvadoretti, P., da Costa, J. F. C. L., Gasper, G. O., & Libardi, D. S. (2018). Comparative Analyses of Geophysical Logs of Resistivity as applied to Coal Deposits. *Revista Brasileira de Geofísica*, **36**, 19-31. http://dx.doi.org/10.22564/.v36i1.861.

Bernard, J., 2003. Short Note on the Depth of Investigation of Electrical Methods. IrisInstruments, Orleans.

BGR (Bundesanstalt für Geowissenschaften und Rohstoffe-Federal Institute for Geosciences and Natural Resources) (2009), Reserves, resources and availability of energy resources-Annual Report 2009, BGR, Hannover, Germany, www.bgr.bund.de.

Carney, J. N., Aldiss, D. T., & Lock, N. P. (1994). The geology of Botswana. Geological Survey Department, **37**, 113p.

Claerbout, J. F., & Muir, F. (1973). Robust modeling with erratic data. *Geophysics*, **38**, 826-844. https://library.seg.org/doi/pdf/10.1190/1.1440378.

Collinson, J. D. (1996). Alluvial sediments: in Reading, HG, ed., Sedimentary Environments.

deGroot-Hedlin, C., & Constable, S. (1990). Occam's inversion to generate smooth, two-dimensional models from magnetotelluric data. *Geophysics*, **55**, 1613-1624. https://doi.org/10.1190/1.1442813.

Ewing, W. M., Crary, A. P., Peoples, J. W., & Peoples, J. A. (1936). Prospecting for anthracite by the Earth-resistivity Method. American Institute of mining and metallurgical engineers, **119**, 43-483.

Farquharson, C. G., & Oldenburg, D. W. (1998). Non-linear inversion using general measures of data misfit and model structure. *Geophysical Journal International*, **134**, 213-227. https://doi.org/10.1046/j.1365-246x.1998.00555.x.

Ganse, A. A. (2008). A Geophysical Inverse Theory Primer. University of Washington: Applied Physics Laboratory and Department of Earth and Space Sciences, Princeton: Princeton University Press, 10p.

Green, D. (1961). The Mamabule coal area. Geological Survey Department, Bechuanaland Protectorate, **2**, 1-65.

Green, D. H., Fenton, M. M., Sterenberg, C., Sartorelli, T., Henderson, J., & Pesowski, M. (1988). Surface geophysical coal research project 1984 to 1986, final report, **112**, 148p.

Grynberg, R. (2012). Coal exports and the diversification of Botswana's economy. Botswana Institute for Development Policy Analysis, 46p.

Ismail A., and Anderson N. (2012). 2D and 3D Resistivity Imaging of Karst Regions in Missouri, USA. *Environmental and Engineering Geoscience*, **18**, 281-293. https://doi.org/10.2113/gseegeosci.18.3.281.

Johnson–D'Appolonia, W. J. (2003). Applications of the electrical resistivity method for detection of underground mine workings. In *Forum on Geophysical Technologies for Detection of Underground Mine Voids*, 28-30.

Kang, L. (2009). Coal Exploration and Mining. *Coal, Oil Shale, Natural Bitumen, Heavy Oil and Peat*-Volume **I**, 92-112.

Krishnamurthy, N. S., Rao, V. A., Kumar, D., Singh, K. K. K., & Ahmed, S. (2009). Electrical resistivity imaging technique to delineate coal seam barrier thickness and demarcate water filled voids. *Journal of the Geological Society of India*, **73**, 639-650. https://doi.org/10.1007/s12594-009-0049-1.

Lecocq, T., & Camelbeeck, T. (2017). Electrical resistivity tomography data across the Hockai fault zone (Ardenne, Belgium). *Data in brief*, **11,** 1-4.

Loke, M. H. (1994). The inversion of two-dimensional resistivity data. Doctoral Thesis, University of Birmingham, U.K., 122p.

Loke, M. H. (2003). Rapid 2D Resistivity & IP Inversion using the least-squares method. *Geotomo Software, Manual*, 122.

Loke, M. H. (2009). Res2Dinv and Res3dinv Software Version 3.59. *Geoelectrical Imaging 2D&3D*, Penang, Malaysia, available at: http://www.geoelectrical.com/downloads.php.

Loke, M. H. (2016). RES2DINVx64 Ver. 4.06 with Multi-Core and 64-Bit Support, Rapid 2-D Resistivity & IP Inversion Using the Least-Squares Method. GEOTOMOSOFT SOLUTIONS GEOTOMO SOFTWARE PTY LTD.

Loke, M. H. (2017). RES3DINVx64 Ver. 3.12 Basic and Professional Versions with Multicore and 64- Bit Support, Rapid 3-D Resistivity & IP Inversion Using the Least-Squares Method. GEOTOMOSOFT SOLUTIONS GEOTOMO SOFTWARE PTY LTD.

Loke, M. H., Acworth, I., & Dahlin, T. (2003). A comparison of smooth and blocky inversion methods in 2D electrical imaging surveys. *Exploration Geophysics*, **34**, 182-187. https://doi.org/10.1071/EG03182.

Loke, M. H., & Barker, R. D. (1995). Least-squares deconvolution of apparent resistivity pseudo sections. *Geophysics*, **60**, 1682-1690. https://doi.org/10.1190/1.1443900.

Loke, M. H., & Dahlin, T. (2002). A comparison of the Gauss–Newton and quasi-Newton methods in resistivity imaging inversion. *Journal of Applied Geophysics*, **49**, 149-162. https://doi.org/10.1016/S0926-9851(01)00106-9.

Mahato, P. P. (2018). Detection of cavity using electrical resistivity tomography (ERT) at Patherdih, Jharia Coal Field, Dhanbad, India. *Universal Journal of Geoscience*, **6**, 114-117. https://doi.org/10.13189/ujg.2018.060402.

McNeil, J. D. (1980). Electrical conductivity of soils and rocks. *GEONICS Limited, Ontario, Canada*, Technical Note TN-5, 22p.

Mohammed, M. A., Adewumi, T., Ahmed, A. L., & Lawal, K. M. (2016). Electrical resistivity imaging of a coal deposit at Tai area of Gombe State, North Eastern Nigeria. *Journal of Environment and Earth Science*, **6**, 55p.

PIXOTEC, LLC, Slicer Dicer. http://www.slicerdicer.com/.

Rao, C. S., Majumder, M., Roy, J., Chaudhari, M. S., & Ramteke, R. S. (2015). Delineating coal seams and establishing water tightness by electrical resistivity imaging. *Current Science*, **108**, 427-434.

Reeves, D. R. (1981). Coal Interpretation Manual. *BPB Instrument Ltd., England*.

Samanlangi, A. I. (2018). Coal Layer Identification using Electrical Resistivity Imaging Method in Sinjai Area South Sulawesi. In *Journal of Physics: Conference Series*, IOP Publishing, **979**, 012048. https://doi.org/10.1088/1742-6596/979/1/012048.

Seferou P., Soupios P., Candasayar E., Papadopoulos N., Sarris A., Aktarakçi H., (2012), Monitoring of contaminant transport by using geoelectrical resistivity tomography, In *CRETE 2012 3rd International Conference on Industrial and Hazardous Waste Management, Chania/Greece*, **2012**, 2-7.

Segwabe, T. (2008). The Geological Framework and Depositional Environments of the Coal-bearing Karoo Strata in the Central Kalahari Karoo Basin, Botswana Unpublished MSc Thesis, Rhodes University, 113p. http://eprints.ru.ac.za/1737/1/Segwabe.pdf.

Shang, X., Shao, L., Zhang, W., Lv, J., Wang, W., Li, Y., Huang, M., Lu, J., Wen, H. (2018). Sequence paleogeography and coal accumulation of the Early–Middle Jurassic in central Qilian Mountain belt (Muli Basin), Qinghai Province, northwestern China. *AAPG Bulletin*, **102**, 1739-1762. https://doi.org/10.1306/01081817063.

Shemang, E., Nthaba, B., Gareutlwane, O., & Molwalefhe, L. (2019, March). Application of Three Dimensional (3D) Electrical Resistivity (ERI) Technique in a Study Conducted on Oil Contaminated Experimental Site in Biust, Palapye, Botswana, In *SAGEEP 2019-32nd Annual Symposium on the Application of Geophysics to Engineering and Environmental Problems*.

Singh, K. K. K., Singh, K. B., Lokhande, R. D., & Prakash, A. (2004). Multielectrode resistivity imaging technique for the study of coal seam, *Journal of Scientific and Industrial Research*, **63**, 927-930.

Sjödahl, P. (2006). Resistivity investigation and monitoring for detection of internal erosion and anomalous seepage in embankment dams. Doctoral Thesis, Engineering Geology, Lund University, Sweden, 86p.

Smith, R. A. (1984). The lithostratigraphy of the Karoo Supergroup in Botswana. Geological Survey Department with the authority of Ministry of Mineral Resources and Water Affairs, Republic of Botswana, **26**, 239p.

Spalding, B. R. (1999). An assessment of reserves, production and export possibilities of coal in African countries. Unpublished MSc Thesis, University of Johannesburg, 163p.

Stummer, P., Maurer, H., & Green, A. G. (2004). Experimental design: Electrical resistivity data sets that provide optimum subsurface information. *Geophysics*, **69**, 120-139. https://doi.org/ 10.1190/1.1649381

Van Schoor, M., & Fourie, C. J. S. (2014). The application of geophysics in South African coal mining and exploration. *Journal of the Southern African Institute of Mining and Metallurgy*, **114**, 875-879.

Venable, N. B., Barnes, D. A., Westjohn, D. B., & Voice, P. J. (2013). Pennsylvanian fluvial-deltaic depositional systems in central lower Michigan: Sedimentology, stratigraphy, and hydrogeology of the Saginaw Aquifer. *Insights into the Michigan Basin: Salt Deposits, Impact Structure, Youngest Basin Bedrock, Glacial Geomorphology, Dune Complexes, and Coastal Bluff Stability*, **31**, 37-56. https://doi.org/10.1130/2013.0031(04).

Williamson, I. T. (1996). The geology of the area around Mmamabula and Dibete: including an account of the Greater Mmamabula Coalfield. Geological Survey Dept., Ministry of Natural Resources and Water Affairs, Republic of Botswana, **6**, 239p.

Wood, G. H., Kehn, T. M., Carter, M. D., & Culbertson, W. C. (1983). Coal resource classification system of the US Geological Survey. *US Geological Survey Circular*, **891,** 65p.